Theory for Quantum Dot Charge Qubits - Decoherence due to Cotunneling

von

Udo Hartmann

Diplomarbeit in Physik
angefertigt am

Lehrstuhl für Theoretische Festkörperphysik
CeNS und Sektion Physik
Ludwig-Maximilians-Universität München

vorgelegt der

Mathematisch-Naturwissenschaftlichen Fakultät
der
Rheinischen Friedrich-Wilhelms-Universität
Bonn

im September 2002

BONN-IB-2002-17

Ich versichere, daß ich diese Arbeit selbständig verfaßt und keine anderen als die angegebenen Quellen und Hilfsmittel benutzt, sowie die Zitate kenntlich gemacht habe.

Referent:	Prof. Dr. Jan von Delft
Korreferent:	Prof. Dr. Hartmut Monien

For my parents, for their love, trust and support during all these years.

-

Für meine Eltern, für ihre Liebe, ihr Vertrauen und ihre Unterstützung in den letzten Jahren.

"[...] And I'm not happy with all the analyses that go with just the classical theory, because nature isn't classical, dammit, and if you want to make a simulation of nature, you'd better it quantum mechanical, and by golly it's a wonderful problem, because it doesn't look so easy."
- R.P. Feynman, *Simulating Physics with Computers*, Int. J. Theor. Phys., **V 21**, 467 (1982).

"The principles of physics, as far as I can see, do not speak against the possibility of maneuvering things atom by atom. It is not an attempt to violate any laws; it is something, in principle, that can be done; but in practice, it has not been done because we are too big."
- R.P. Feynman, *Plenty of Room at the Bottom* (lecture), December 1959.

Contents

Contents **1**

1 Introduction **3**
1.1 Quantum computation 3
1.2 Coupled double dots as a qubit 4
1.3 Overview 5

2 Physical starting point **6**
2.1 General case 6
2.2 Atomic limit 8

3 Schrieffer-Wolff transformation **9**
3.1 General case 9
3.2 Atomic limit 11

4 Bloch-Redfield formalism **12**
4.1 Formalism 12
4.2 Renormalization 13
4.3 General case 15
4.4 Atomic limit 18

5 Calculation of the current **21**

6 Discussion of the results **25**
6.1 Relaxation times 26
6.1.1 Internal energies 26
6.1.2 Temperature 28
6.1.3 Bias voltage 29
6.2 Dephasing times 30
6.2.1 Internal energies 30
6.2.2 Temperature 32
6.2.3 Bias voltage 33
6.3 Stationary current 34
6.3.1 Internal energies 34

6.3.2 Temperature . . . 37
6.3.3 Bias voltage . . . 38
6.4 Conductance and differential conductance . . . 39
6.5 Time-dependent elements of the reduced density matrix . . . 42
6.6 Time-dependent current . . . 43
6.7 Stability in the double dot system . . . 44

7 Conclusions **47**

8 Deutsche Zusammenfassung **50**

Acknowledgements **54**

A Schrieffer-Wolff coefficients **55**

B Effect of the renormalization **59**

C Rules for the integrals **64**
C.1 Rules for $\Gamma^{(+)}$ . . . 64
C.1.1 $\omega_{nk} = 0$ . . . 64
C.1.2 $\omega_{nk} \neq 0$ . . . 64
C.2 Rules for $\Gamma^{(-)}$ . . . 65
C.2.1 $\omega_{lm} = 0$ . . . 65
C.2.2 $\omega_{lm} \neq 0$ . . . 65

D Functions for the atomic limit **67**

E Some Comments on the Implementation **69**

F Some 3D Pictures **70**
F.1 Relaxation time . . . 70
F.2 Dephasing time . . . 71
F.3 Stationary current . . . 72

Used symbols **73**

List of Figures **75**

Bibliography **77**

Chapter 1

Introduction

1.1 Quantum computation

Following first ideas of Richard Feynman [1] to simulate quantum mechanical properties in quantum mechanical systems, quantum computation started being a primary and promising field of research in the late 90s of the last century.

Following the elementary algorithm of David Deutsch [2], much of the recent attention is due to the algorithms of Shor [3] and Grover [4]. Shor's algorithm factorizes numbers quicker than every classical computer (exponential speedup), using Grover's algorithm one can search a database entry faster than on a normal computer ($\sqrt{N}$ speedup, where $N =$ number of database entries).

Since then several realizations have been proposed for quantum computation; in particular, quantum optics [5, 6, 7] and nuclear magnetic resonance (NMR) systems [8] were used to define these two-state systems, so-called quantum bits (or *qubits*), which can be brought in a superpostion of the two classical states.

Qubits based on quantum optical methods are excellent examples for tunable microscopic quantum systems, because of their stability against influences from the outside world, and have been studied very intensely [9]. Quantum cryptography [10, 11] is also based on quantum optics, first commercial systems are available now. In 2001, Shor's algorithm was implemented first [12] in an NMR setup and it was used to factorize a number. Only seven qubits have been addressed to factorize the number 15.

But back to the basic ideas, there are three main features of a quantum computer:

1. the possibility for a qubit to be in an *superposition* of two states, $|\psi\rangle = \alpha\,|0\rangle + \beta\,|1\rangle$.

2. quantum *parallelism*, i.e. calculations can have a large number of results in the same moment, of which only one is read out.

3. *entanglement*, which means an nonlocal correlation between qubits, used e.g. in Shor's algorithm and in quantum cryptography.

In order to build a large quantum computer, one has to couple many qubits to each other (e.g. in [13]). Solid state devices, where one can design the system by hand in a very flexible

way, have the advantage that they can easily be coupled by lithographic techniques. These methods are widely known for integrating devices in electrical circuits.

1.2 Coupled double dots as a qubit

Solid state devices are usually strongly limited by decoherence, so one has to choose an appropriate system for the realization of a *scalable* quantum computer [14].

Quantum dots ("artificial atoms") are prototype systems for realizing quantum bits, fully controllable two-state quantum systems, in solid state physics. There are various proposals to define qubits in quantum dots, e.g. one could use the spin degree of freedom [15] in coupled quantum dots or optically excited charge states in etched quantum dots [16].

We however consider another realization, a *charge* qubit whose basis states are defined by the position (either on the left or right dot) of an additional, spin-polarized electron in the system of two laterally coupled quantum dots (i.e. an "artificial molecule") [17]. The experiment of Waugh et al. [18] was the first, where coherent molecular states have been observed. The coupling of these two states can be controlled externally by a highly transparent quantum point contact between the two dots (red in Figure 1.1). In this Figure 1.1 the system under consideration is sketched. The system has two leads (μ_L and

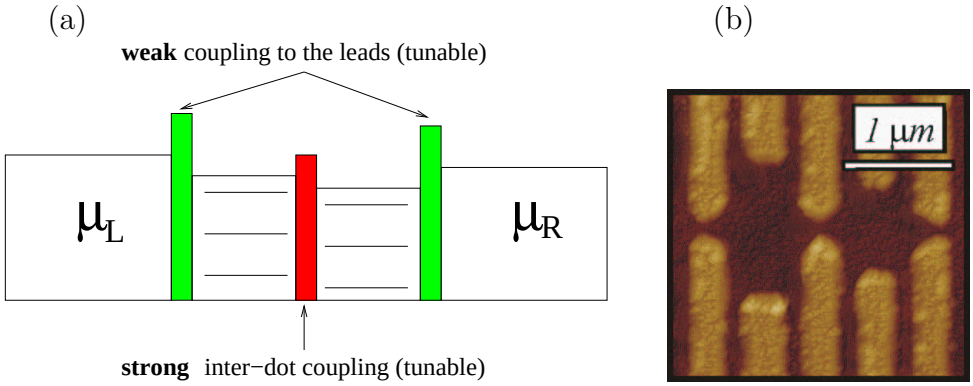

Figure 1.1: (a) Sketch of the double dot system, (b) scanning electron microscope (SEM) picture of a real double dot system

μ_R) which are attached to one dot each via a weak, tunable coupling (green), realized by a low transparent quantum point contact.

In order to minimize the inevitable decoherence through coupling to the electronic leads, this setup can be biased in the Coulomb Blockade regime where sequential tunneling [19] is supressed. This regime can be reached by adjusting the gate voltages such that the levels under consideration are far outside the transport window. The main goal of this thesis is to investigate how the cotunneling contribution [20] in this regime decoheres the system. We shall consider only spin-polarized electrons, because we want to use only the charge

degree of freedom to define the qubit. This spin-polarization can be realized by applying a magnetic field B_{P}, which should be in-plane with the lateral dots. It has been shown for the Kondo regime [21], that already if $g_{\mathrm{P}}\mu_{\mathrm{B}}B_{\mathrm{P}} > k_B T_{\mathrm{K}}$, the physics is governed by the charge degrees of freedom only. T_{K} is the Kondo temperature, which is assumed to be much smaller than the temperature throughout the present work, so that Kondo physics can be ignored. However, to achieve full spin polarization, we have to fulfil another condition for Zeeman splitting $g_{\mathrm{P}}\mu_{\mathrm{B}}B_{\mathrm{P}} > 2\delta$, where 2δ is the level splitting in our molecular system and will be defined later (see Chapter 2).

This system is treated by using the well-established Bloch-Redfield theory, which can be applied to describe the weak coupling to the environment perturbatively and to take the strong internal coupling fully into account. Originally the Bloch-Redfield method was developed to describe NMR physics [22] and it has been widely used in chemical physics. In the few last years it turned out that Bloch-Redfield theory could also be used as an alternative to path-integral methods in open quantum systems, even at *low* temperatures, as realized in solid state physics [23]. This has been done for some other models such as the Spin-Boson model (see e.g. [24]), so that some experience exists in using the Bloch-Redfield formalism for quantum control and decoherence. It could be interesting to analyze analogies between the different systems.

We use a Schrieffer-Wolff transformation to derive an effective Hamiltonian that incorporates cotunneling processes. And then we use this effective Hamiltonian as starting point for our Bloch-Redfield approach (which uses a Born approximation with the input Hamiltonian). If we take the normal Hamiltonian as input, we would get a description of sequential tunneling only. The Schrieffer-Wolff transformation gives an effective Hamiltonian with higher orders in the coupling to the leads. With this new Hamiltonian, Bloch-Redfield theory results in a Born approximation in higher orders, that means that we do describe cotunneling.

We study the general case plus a simple Gedanken experiment, where the system is initially brought into a superposition and then the inter-dot tunneling is removed nonadiabatically.

1.3 Overview

We will start the discussion of the above mentioned system by explaining the model Hamiltonian (Chapter 2). Chapter 3 covers the Schrieffer- Wolff transformation as a tool to treat cotunneling in such a system. The Bloch-Redfield formalism is considered and fully used in Chapter 4. In Chapter 5 an expression for the current through the coupled double dot system is derived. The numerical results of Chapters 4 and 5 and their interpretation can be found in Chapter 6. In Chapter 7 we draw our conclusions from this work. Chapter 8 is a summary in German language. The regular chapters are supplemented by technical appendices.

First results for the simple Gedanken experiment mentioned above have been published recently [25].

Chapter 2

Physical starting point

2.1 General case

In the Coulomb Blockade regime [26, 27], the relevant Hilbert space is spanned by four basis states, written as $|i,j\rangle$, which denotes i additional electrons on the left dot, j additional electrons on the right dot. The two states $|1,0\rangle$ and $|0,1\rangle$ define the computational basis [14], because they are energetically stable due to the charging energy. The energy levels for one electron each are very far from each other in ultra-small dots. In this regime cotunneling is the most important process of the coupling to the leads, thus we use the closest energetically forbidden states as virtual intermediate states. These are $|v_0\rangle = |0,0\rangle$ and $|v_2\rangle = |1,1\rangle$. Zero and two electron states are energetically even less favorable due to the high charging energy of the individual dots.

The Hamiltonian of this system can be written as

$$
\begin{aligned}
H &= H_0 + H_1 && (2.1)\\
H_0 &= H_{\text{sys}} + H_{\text{res}} && (2.2)\\
H_{\text{sys}} &= \epsilon_{\text{as}}(\hat{n}_l - \hat{n}_r) - \epsilon_\alpha \hat{n}_{v_0} + \epsilon_\beta \hat{n}_{v_2} + \gamma \sum_n (a_n^{L\dagger} a_n^R + a_n^{R\dagger} a_n^L) && (2.3)\\
H_{\text{res}} &= \sum_{\vec{k}} \epsilon_{\vec{k}}^L b_{\vec{k}}^{L\dagger} b_{\vec{k}}^L + \sum_{\vec{k\prime}} \epsilon_{\vec{k\prime}}^R b_{\vec{k\prime}}^{R\dagger} b_{\vec{k\prime}}^R && (2.4)\\
H_1 &= t_c \sum_{\vec{k},n} (a_n^{L\dagger} b_{\vec{k}}^L + a_n^L b_{\vec{k}}^{L\dagger}) + t_c \sum_{\vec{k\prime},m} (a_m^{R\dagger} b_{\vec{k\prime}}^R + a_m^R b_{\vec{k\prime}}^{R\dagger}) \ . && (2.5)
\end{aligned}
$$

Note, that the sum over dot states only runs over the restricted Hilbert space described above. H_0 describes the energy spectrum of the isolated double-dot (H_{sys}) and the leads (H_{res}), whereas the tunneling part H_1 describes the coupling of each dot to its lead and will be treated as a perturbation. $\hat{n}_{l/r}$ are the number operators counting additional electrons on either dot. The asymmetry energy $\epsilon_{\text{as}} = (\epsilon_l - \epsilon_r)/2$ describes the difference between the energy level for the additional electron in left dot (ϵ_l) and the corresponding energy level in the right dot (ϵ_r). It can be tuned via the gate voltages which are applied at each dot. ϵ_β and ϵ_α are the energy differences towards the higher level $|v_2\rangle$ and the lower level

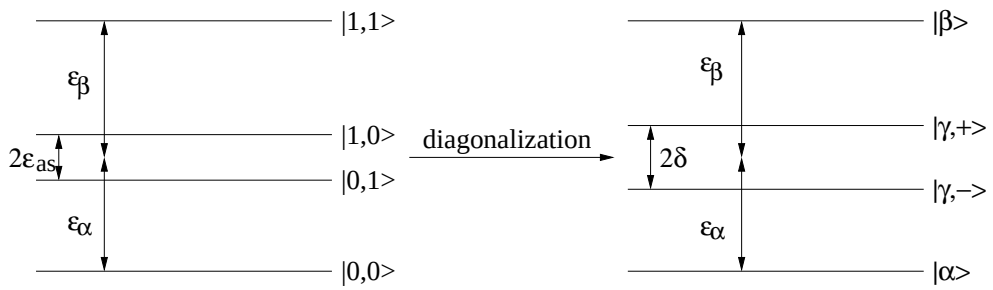

Figure 2.1: Energy spectrum of the system before and after a diagonalization; δ is defined as $\delta = \sqrt{\epsilon_{\text{as}}^2 + \gamma^2}$.

$|v_0\rangle$ respectively (see Figure 2.1). γ is the tunable inter-dot coupling. The $a^{(\dagger)}$s and $b^{(\dagger)}$s denote electron creation/annihilation operators in the dots and leads. In H_1 the symbol t_c represents the tunnel matrix element between the dots and the leads, which should be small compared to the asymmetry energy. Note, that we have chosen a slightly asymmetric notation in order to highlight the physical model: For the actual calculation, H_1 is also expressed in the localized basis of the dot. The matrix representation of H_0 is (states in decreasing order)

$$H_0 = \begin{pmatrix} \epsilon_\beta & 0 & 0 & 0 \\ 0 & \epsilon_{\text{as}} & \gamma & 0 \\ 0 & \gamma & -\epsilon_{\text{as}} & 0 \\ 0 & 0 & 0 & -\epsilon_\alpha \end{pmatrix} + \begin{pmatrix} E_0 & 0 & 0 & 0 \\ 0 & E_0 & 0 & 0 \\ 0 & 0 & E_0 & 0 \\ 0 & 0 & 0 & E_0 \end{pmatrix} , \tag{2.6}$$

where E_0 is the energy offset due to the energies of the two leads.

The eigenstates of the double-dot are

$$|\gamma, +\rangle = \frac{1}{S}\left(|1,0\rangle + \frac{\gamma}{\delta + \epsilon_{\text{as}}} |0,1\rangle \right) \tag{2.7}$$

$$|\gamma, -\rangle = \frac{1}{S}\left(-\frac{\gamma}{\delta + \epsilon_{\text{as}}} |1,0\rangle + |0,1\rangle \right) , \tag{2.8}$$

where $S = \sqrt{1 + \frac{\gamma^2}{(\delta+\epsilon_{\text{as}})^2}}$ is a normalization factor. We will call these states also "molecular states", because these states represent in case of a dominating inter-dot coupling γ the bonding and anti-bonding state in a molecule. These molecular states are exact eigenstates of H_0 and serve as a starting point for our perturbation theory (next chapter). There are no clear transition rules anymore, because in the new basis both states couple to both leads. The upper state $|v_2\rangle = |1,1\rangle = |\beta\rangle$ and the lower state $|v_0\rangle = |0,0\rangle = |\alpha\rangle$ remain unchanged. In the new basis, the diagonal matrix representation of H_0 has the following

form (again in decreasing order of energy levels)

$$H_{0,diag} = \begin{pmatrix} \epsilon_\beta + E_0 & 0 & 0 & 0 \\ 0 & \delta + E_0 & 0 & 0 \\ 0 & 0 & -\delta + E_0 & 0 \\ 0 & 0 & 0 & -\epsilon_\alpha + E_0 \end{pmatrix}, \tag{2.9}$$

here the half level splitting δ is $\delta = \sqrt{\epsilon_{\text{as}}^2 + \gamma^2}$, as in the caption of Figure 2.1.

2.2 Atomic limit

In order to treat one limit analytically by hand, we consider a Gedanken experiment, in which all terms are simplified and the number of terms is reduced.

For our Gedanken experiment, we assume that first the inter-dot coupling γ is high such that the system relaxes into the ground state, which is a molecular superposition state of the form $|g\rangle = (|0,1\rangle - |1,0\rangle)/\sqrt{2}$. Then the gate voltage that controls the inter-dot coupling is switched to high values, so that the coupling is practically zero. After this, the system dephases and relaxes into a thermal mixture of the localized eigenstates of the new system. Thus, in order to describe decoherence, we only have to consider the case $\gamma = 0$. This means, that H_0 is already diagonal, i.e. the states $|1,1\rangle$, $|1,0\rangle$, $|0,1\rangle$ and $|0,0\rangle$ are eigenstates of our system. We call this the "atomic limit", because here both dots act like uncoupled atoms.

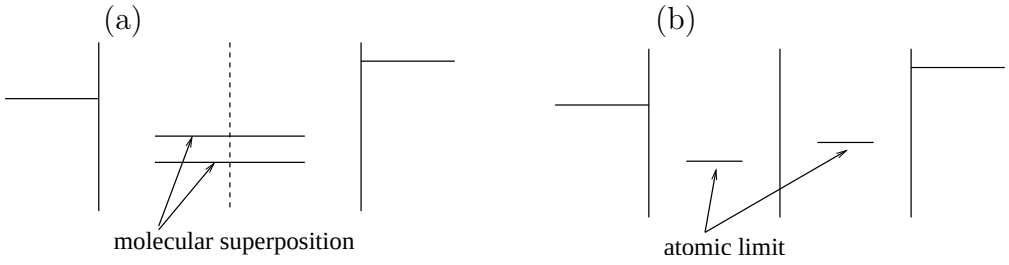

Figure 2.2: Sketch of the two phases for the Gedanken experiment: (a) superposition, (b) atomic limit

Chapter 3

Schrieffer-Wolff transformation

3.1 General case

We want to apply the well-established and controlled Bloch-Redfield theory, because it is a common and systematic tool for describing open quantum systems. It uses a Born approximation and includes the non-markovian parts up to errors beyond the Born approximation. Originally Bloch-Redfield theory uses a Liouville equation of motion for the density matrix of a given system as a starting point. Bloch-Redfield theory has been shown to be numerically equivalent [23] to path integral methods for low temperatures and it should be appropriate for such a system (strong inter-dot coupling, weak dot-lead coupling). This involves using the Born-approximation in the system bath-coupling. In the Coulomb blockade, the first order result of the time dependent perturbation theory for H_1 would vanish. In order to treat cotunneling with this formalism, we perform a generalized Schrieffer-Wolf transformation which generates transition terms in our effective Hamiltonian between the unperturbed levels which originate from indirect processes via the intermediate states.

The Schrieffer-Wolff transformation [28] has to be carried out in a way which generalizes the transformation of the standard Anderson model. This transformation is also known under different names in other fields such as atomic physics [29] or chemical physics [30].

This Schrieffer-Wolff transformation transforms indirect processes between the multiplets into direct transitions in the molecular basis (see Figure 3.1): one starts from one eigenstate ($|\gamma,+\rangle$ or $|\gamma,-\rangle$) in the two-state system, then goes via a virtual process to one of the two other levels ($|\beta\rangle$ or $|\alpha\rangle$). From there one goes back to the two-state system again using a virtual process, but not necessarily to the starting state. And all possible processes must be summed up. This is the way how the four elements of $H_{I,\text{eff}}$ are determined. The above mentioned procedure is captured in the expression

$$\begin{aligned} \langle \gamma, i | \, H_{I,\text{eff}} \, | \gamma, j \rangle &= \frac{1}{2} \sum_{\phi \neq \gamma} \langle \gamma, i | \, H_1 \, | \phi \rangle \, \langle \phi | \, H_1 \, | \gamma, j \rangle \times \\ &\quad \times \left[\frac{1}{E_{\gamma,i} - E_\phi \pm \epsilon_s^{L/R}} + \frac{1}{E_{\gamma,j} - E_\phi \mp \epsilon_s^{L/R}} \right] , \end{aligned} \tag{3.1}$$

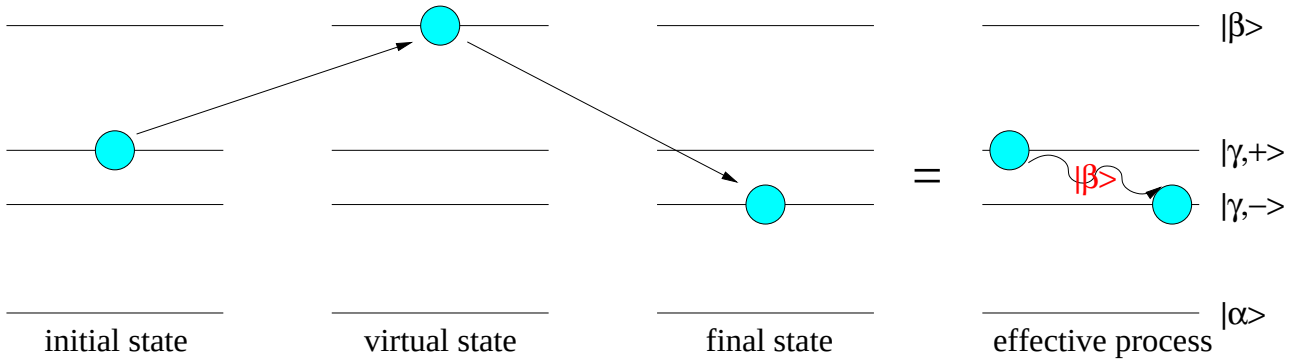

Figure 3.1: Principle of the generalized Schrieffer-Wolff transformation

where γ and ϕ are labels for different multiplets in the spectrum of the problem. γ denotes the molecular two-state system and ϕ can here be either β (i.e. the upper virtual state $|\beta\rangle$ or α (i.e. the lower virtual state $|\alpha\rangle$). i and j can be either $+$ or $-$ (for the molecular states $|\gamma,+\rangle$ and $|\gamma,-\rangle$). The Es are the eigenenergies of the corresponding states.
Equation (3.1) can be found in a similar way in [29], however, one has to realize that the leads change their energies as well, hence $\pm\epsilon_s^{L/R}$ and $\mp\epsilon_s^{L/R}$ show up. This generalizes standard second order perturbation theory, where only diagonal matrix elements are calculated.
As a final result, one gets the parts of $H_{I,\text{eff}}$ as

$$\begin{aligned}
\langle\gamma,+|\, H_{I,\text{eff}}\,|\gamma,+\rangle = H_{I,++} \;=\;& A(R\dagger,R,++)\; b_m^{R\dagger}b_n^R + A(R\dagger,L,++)\; b_m^{R\dagger}b_l^L + \\
&+A(L\dagger,R,++)\; b_k^{L\dagger}b_n^R + A(L\dagger,L,++)\; b_k^{L\dagger}b_l^L + \\
&+A(L,L\dagger,++)\; b_l^L b_k^{L\dagger} + A(L,R\dagger,++)\; b_l^L b_m^{R\dagger} + \\
&+A(R,L\dagger,++)\; b_n^R b_k^{L\dagger} + A(R,R\dagger,++)\; b_n^R b_m^{R\dagger} \qquad (3.2)\\
\langle\gamma,-|\, H_{I,\text{eff}}\,|\gamma,-\rangle = H_{I,--} \;=\;& A(R\dagger,R,--)\; b_m^{R\dagger}b_n^R + A(R\dagger,L,--)\; b_m^{R\dagger}b_l^L + \\
&+A(L\dagger,R,--)\; b_k^{L\dagger}b_n^R + A(L\dagger,L,--)\; b_k^{L\dagger}b_l^L + \\
&+A(L,L\dagger,--)\; b_l^L b_k^{L\dagger} + A(L,R\dagger,--)\; b_l^L b_m^{R\dagger} + \\
&+A(R,L\dagger,--)\; b_n^R b_k^{L\dagger} + A(R,R\dagger,--)\; b_n^R b_m^{R\dagger} \qquad (3.3)\\
\langle\gamma,+|\, H_{I,\text{eff}}\,|\gamma,-\rangle = H_{I,+-} \;=\;& A(R\dagger,R,+-)\; b_m^{R\dagger}b_n^R + A(R\dagger,L,+-)\; b_m^{R\dagger}b_l^L + \\
&+A(L\dagger,R,+-)\; b_k^{L\dagger}b_n^R + A(L\dagger,L,+-)\; b_k^{L\dagger}b_l^L + \\
&+A(L,L\dagger,+-)\; b_l^L b_k^{L\dagger} + A(L,R\dagger,+-)\; b_l^L b_m^{R\dagger} + \\
&+A(R,L\dagger,+-)\; b_n^R b_k^{L\dagger} + A(R,R\dagger,+-)\; b_n^R b_m^{R\dagger} \qquad (3.4)\\
\langle\gamma,-|\, H_{I,\text{eff}}\,|\gamma,+\rangle = H_{I,-+} \;=\;& A(R\dagger,R,-+)\; b_m^{R\dagger}b_n^R + A(R\dagger,L,-+)\; b_m^{R\dagger}b_l^L + \\
&+A(L\dagger,R,-+)\; b_k^{L\dagger}b_n^R + A(L\dagger,L,-+)\; b_k^{L\dagger}b_l^L + \\
&+A(L,L\dagger,-+)\; b_l^L b_k^{L\dagger} + A(L,R\dagger,-+)\; b_l^L b_m^{R\dagger} + \\
&+A(R,L\dagger,-+)\; b_n^R b_k^{L\dagger} + A(R,R\dagger,-+)\; b_n^R b_m^{R\dagger}\;. \qquad (3.5)
\end{aligned}$$

The As are called *Schrieffer-Wolff coefficients*, they are calculated with equation (3.1) and can be found in Appendix A. The $+$ and $-$ signs represent the molecular states $|\gamma, +\rangle$ and $|\gamma, -\rangle$.

3.2 Atomic limit

In the special case of the Gedanken experiment, one finds the following equations

$$H_{I,++} = A(R\dagger, R, ++)\; b_m^{R\dagger} b_n^R + A(L, L\dagger, ++)\; b_l^L b_k^{L\dagger} \tag{3.6}$$
$$H_{I,--} = A(L\dagger, L, --)\; b_k^{L\dagger} b_l^L + A(R, R\dagger, --)\; b_n^R b_m^{R\dagger} \tag{3.7}$$
$$H_{I,+-} = A(R\dagger, L, +-)\; b_m^{R\dagger} b_l^L + A(L, R\dagger, +-)\; b_l^L b_m^{R\dagger} \tag{3.8}$$
$$H_{I,-+} = A(L\dagger, R, -+)\; b_k^{L\dagger} b_n^R + A(R, L\dagger, -+)\; b_n^R b_k^{L\dagger}\ . \tag{3.9}$$

If one compares these four equations (3.6)-(3.9) to the general case (3.2)-(3.5), it is obvious that a lot of terms are missing in this special case. This is due to the symmetry of the considered "atomic" states.

Figure 3.2 illustrates the processes in equations (3.6)-(3.9), where the cyan (magenta) circle denotes the final (initial) position of the starting state. The green arrows represent the first processes, the red ones the second processes. The $+$ sign denotes the same sign in equations (3.6)-(3.9).

The processes acting on the left panels in Figure 3.2 are $|\beta\rangle$ mediated virtual processes (like the one in Figure 3.1), on the right panels the $|\alpha\rangle$ mediated virtual transitions are shown.

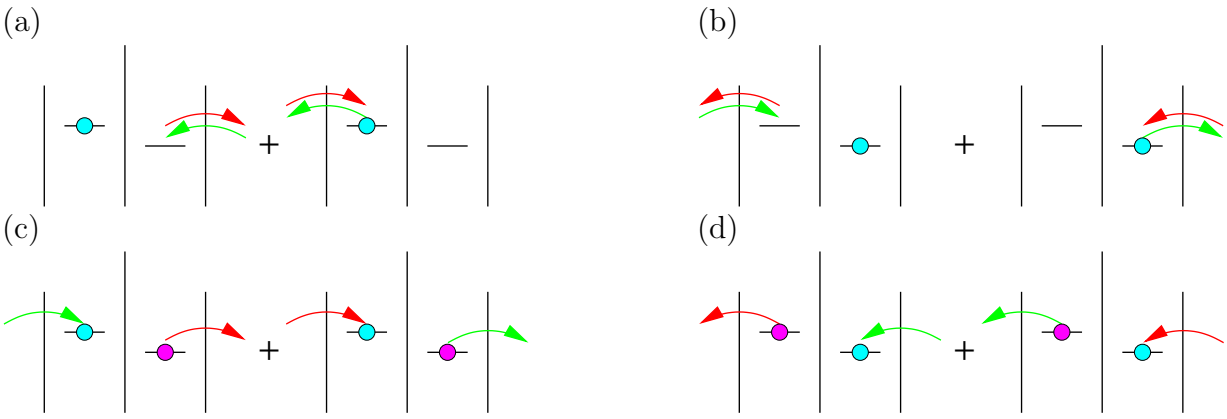

Figure 3.2: Sketch of the virtual processes involved in (a) $H_{I,++}$, (b) $H_{I,--}$, (c) $H_{I,+-}$ and (d) $H_{I,-+}$

Chapter 4

Bloch-Redfield formalism

4.1 Formalism

As a starting point for the derivation of the Bloch-Redfield equations (4.4), one usually [31] takes the Liouville equation of motion for the density matrix of the whole system $W(t)$ (describing the time evolution of the system)

$$\dot{W}(t) = -\frac{i}{\hbar}\left[H, W(t)\right] \ , \tag{4.1}$$

where

$$H = H_{\text{sys}} + H_{\text{res}} + H_I \ . \tag{4.2}$$

H_{sys} is the Hamiltonian which describes the system (in our case: the double-dot system), H_{res} stands for the reservoirs (the two leads) and H_I is the interaction Hamiltonian between system and reservoirs.
Projecting the the density matrix of the whole system $W(t)$ on the relevant part of the system (which means only our two-state system), one finally gets the reduced density matrix ρ

$$\rho(t) = PW(t) \ , \tag{4.3}$$

where P is the projector on the relevant sub-system. Putting (4.3) in equation (4.1) one gets the Nakajima-Zwanzig equation [32, 33]. If one then uses the Born approximation and back-propagation, one finally comes to the Bloch-Redfield equations for the reduced density matrix ρ in the eigenstate basis of H_{sys} [31, 34]

$$\dot{\rho}_{nm}(t) = -i\omega_{nm}\rho_{nm}(t) - \sum_{k,l} R_{nmkl}\rho_{kl}(t) \ , \tag{4.4}$$

where R_{nmkl} are the elements of the Redfield tensor and the ρ_{nm} are the elements of the reduced density matrix. These equations of motion for the reduced density matrix ρ are obtained within Born approximation in the effective system-bath coupling, so after the Schrieffer-Wolff transformation, the R_{nmkl} are of the order t_c^4. Let us remark that our perturbation theory naturally breaks down below the Kondo temperature T_{K}, which can

however be made arbitrarily small by lowering t_c through pinching off the contacts to the reservoirs.

The Bloch-Redfield equations are of Markovian form, however, by properly using the free time evolution of the system (back-propagation), they take into account all bath correlations which are relevant within the Born approximation [23]. In [23] it has also been shown that in the bosonic case the Bloch-Redfield theory is numerically equivalent to the path-integral method.

The Redfield tensor has the form

$$R_{nmkl} = \delta_{lm} \sum_r \Gamma^{(+)}_{nrrk} + \delta_{nk} \sum_r \Gamma^{(-)}_{lrrm} - \Gamma^{(+)}_{lmnk} - \Gamma^{(-)}_{lmnk}. \tag{4.5}$$

The rates entering the Redfield tensor elements are given by the following Golden-Rule expressions

$$\Gamma^{(+)}_{lmnk} = \hbar^{-2} \int_0^\infty dt\ e^{-i\omega_{nk}t} \langle \tilde{H}_{I,lm}(t) \tilde{H}_{I,nk}(0) \rangle \tag{4.6}$$

$$\Gamma^{(-)}_{lmnk} = \hbar^{-2} \int_0^\infty dt\ e^{-i\omega_{lm}t} \langle \tilde{H}_{I,lm}(0) \tilde{H}_{I,nk}(t) \rangle\ , \tag{4.7}$$

where H_I appears in the interaction representation (written as $\tilde{H}_I$). In the interaction picture one has to replace [35] all operators in second quantization by time-dependent operators, e.g. $b^{R\dagger}_m(t) = b^{R\dagger}_m(0) e^{\frac{i}{\hbar}\epsilon^R_m t}$. l, m, n and k can be either $+$ or $-$. ω_{nk} is defined as $\omega_{nk} = (E_n - E_k)/\hbar$. The possible values of ω_{nk} are $\omega_{++} = \omega_{--} = 0$, $\omega_{+-} = \frac{2\delta}{\hbar}$ and $\omega_{-+} = -\frac{2\delta}{\hbar}$.

4.2 Renormalization

In order to use the Bloch-Redfield theory, the effective interaction Hamiltonian $\tilde{H}_I$ should only produce noise, i.e. the expectation value of $\tilde{H}_I$ must vanish

$$\langle \tilde{H}_I \rangle = 0\ . \tag{4.8}$$

Considering now the Hamiltonian which we calculated in the last chapter, we observe that $\langle \tilde{H}_I \rangle \neq 0$. If we continue to work with this interaction Hamiltonian, we would get some divergences. Thus we reformulate $\tilde{H}_I$ by

$$\tilde{H}_I(t) := \tilde{H}_I(t) - \langle \tilde{H}_I(t) \rangle \tag{4.9}$$

$$\begin{aligned}
\tilde{H}_I(t) = {} & A(R\dagger, R) b^{R\dagger}_m(t) b^R_n(t) + A(R\dagger, L) b^{R\dagger}_m(t) b^L_l(t) \\
& + A(L\dagger, R) b^{L\dagger}_k(t) b^R_n(t) + A(L\dagger, L) b^{L\dagger}_k(t) b^L_l(t) \\
& + A(L, L\dagger) b^L_l(t) b^{L\dagger}_k(t) + A(L, R\dagger) b^L_l(t) b^{R\dagger}_m(t) \\
& + A(R, L\dagger) b^R_n(t) b^{L\dagger}_k(t) + A(R, R\dagger) b^R_n(t) b^{R\dagger}_m(t) \\
& - A(L\dagger, L) f_L(\epsilon^L_k) \delta_{kl} - A(R\dagger, R) f_R(\epsilon^R_m) \delta_{mn} \\
& - A(L, L\dagger)(1 - f_L(\epsilon^L_k)) \delta_{kl} - A(R, R\dagger)(1 - f_R(\epsilon^R_m)) \delta_{mn}\ .
\end{aligned} \tag{4.10}$$

Of course this must be done for all four components of $\tilde{H}_I$. In order to compensate this definition, one has to change the unperturbed Hamiltonian $H_{0,\mathrm{diag}}$ as well,

$$H_{0,\mathrm{diag}} := H_{0,\mathrm{diag}} + \langle \tilde{H}_I(t) \rangle \ . \tag{4.11}$$

This effect on $H_{0,\mathrm{diag}}$, will be considered in Appendix B and shown to be small. The correlation function in (4.6) is then

$$\begin{aligned}
&\langle \tilde{H}_I(t)\tilde{H}_I(0)\rangle = \\
&\sum_{\substack{k,k',l,l' \\ m,m',n,n'}} \langle A(R\dagger,R) b_m^{R\dagger}(t) b_n^R(t) \times \tilde{H}_I(0) + A(R\dagger,L) b_m^{R\dagger}(t) b_l^L(t) \times \tilde{H}_I(0) \\
&+A(L\dagger,R) b_k^{L\dagger}(t) b_n^R(t) \times \tilde{H}_I(0) + A(L\dagger,L) b_k^{L\dagger}(t) b_l^L(t) \times \tilde{H}_I(0) \\
&+A(L,L\dagger) b_l^L(t) b_k^{L\dagger}(t) \times \tilde{H}_I(0) + A(L,R\dagger) b_l^L(t) b_m^{R\dagger}(t) \times \tilde{H}_I(0) \\
&+A(R,L\dagger) b_n^R(t) b_k^{L\dagger}(t) \times \tilde{H}_I(0) + A(R,R\dagger) b_n^R(t) b_m^{R\dagger}(t) \times \tilde{H}_I(0) \\
&-A(R\dagger,R) f_R(\epsilon_m^R)\delta_{mn} \times \tilde{H}_I(0) - A(L\dagger,L) f_L(\epsilon_k^L)\delta_{kl} \times \tilde{H}_I(0) \\
&-A(L,L\dagger)(1-f_L(\epsilon_k^L))\delta_{kl} \times \tilde{H}_I(0) - A(R,R\dagger)(1-f_R(\epsilon_m^R))\delta_{mn} \times \tilde{H}_I(0)\rangle \ ,
\end{aligned} \tag{4.12}$$

where

$$\begin{aligned}
\tilde{H}_I(0) \ = \ & A'(R\dagger,R) b_{m'}^{R\dagger} b_{n'}^R + A'(R\dagger,L) b_{m'}^{R\dagger} b_{l'}^L + A'(L\dagger,R) b_{k'}^{L\dagger} b_{n'}^R \\
&+A'(L\dagger,L) b_{k'}^{L\dagger} b_{l'}^L + A'(L,L\dagger) b_{l'}^L b_{k'}^{L\dagger} + A'(L,R\dagger) b_{l'}^L b_{m'}^{R\dagger} \\
&+A'(R,L\dagger) b_{n'}^R b_{k'}^{L\dagger} + A'(R,R\dagger) b_{n'}^R b_{m'}^{R\dagger} \\
&-A'(R\dagger,R) f_R(\epsilon_{m'}^R)\delta_{m'n'} - A'(L\dagger,L) f_L(\epsilon_{k'}^L)\delta_{k'l'} \\
&-A'(L,L\dagger)(1-f_L(\epsilon_{k'}^L))\delta_{k'l'} - A'(R,R\dagger)(1-f_R(\epsilon_{m'}^R))\delta_{m'n'} \ ,
\end{aligned} \tag{4.13}$$

which was calculated from the original Hamiltonian through the Schrieffer-Wolff transformation. All primed coefficients and variables represent the time-independent case. From all the possible cases, only two major cases are relevant: the first is $k = l$, $k' = l'$, $m = n$ and $m' = n'$, the second is $k = l'$, $l = k'$, $m = n'$ and $n = m'$. All other possibilities are neglected, because their expectation values vanish. All terms for the first case also vanish (this is due to the reformulation of $\tilde{H}_I$) and only the second case is relevant and additionally the sum changes to an integral in the continuum limit

$$\begin{aligned}
\langle \tilde{H}_I(t)\tilde{H}_I(0)\rangle \ = \ & c_1 \int_{-\infty}^{\infty}\int_{-\infty}^{\infty} d\epsilon_k^L d\epsilon_l^L e^{\frac{i}{\hbar}(\epsilon_k^L-\epsilon_l^L)t} f_L(\epsilon_k^L)(1-f_L(\epsilon_l^L)) \times \\
&\times [A(L\dagger,L)(A'(L\dagger,L)-A'(L,L\dagger)) + A(L,L\dagger)(A'(L,L\dagger)-A'(L\dagger,L))] \\
&+c_1 \int_{-\infty}^{\infty}\int_{-\infty}^{\infty} d\epsilon_m^R d\epsilon_n^R e^{\frac{i}{\hbar}(\epsilon_m^R-\epsilon_n^R)t} f_R(\epsilon_m^R)(1-f_R(\epsilon_n^R)) \times \\
&\times [A(R\dagger,R)(A'(R\dagger,R)-A'(R,R\dagger)) + A(R,R\dagger)(A'(R,R\dagger)-A'(R\dagger,R))] \\
&+c_1 \int_{-\infty}^{\infty}\int_{-\infty}^{\infty} d\epsilon_k^L d\epsilon_n^R e^{\frac{i}{\hbar}(\epsilon_k^L-\epsilon_n^R)t} f_L(\epsilon_k^L)(1-f_R(\epsilon_n^R)) \times
\end{aligned}$$

$$
\begin{aligned}
&\times[A(L\dagger,R)(A'(R\dagger,L)-A'(L,R\dagger))+A(R,L\dagger)(A'(L,R\dagger)-A'(R\dagger,L))]\\
&+c_1\int_{-\infty}^{\infty}\int_{-\infty}^{\infty}d\epsilon_m^R d\epsilon_l^L e^{\frac{i}{\hbar}(\epsilon_m^R-\epsilon_l^L)t}f_R(\epsilon_m^R)(1-f_L(\epsilon_l^L))\times\\
&\times[A(R\dagger,L)(A'(L\dagger,R)-A'(R,L\dagger))+A(L,R\dagger)(A'(R,L\dagger)-A'(L\dagger,R))]\ ,
\end{aligned}
\tag{4.14}
$$

where c_1 is $c_1 = \frac{V_{2\mathrm{DEG}}^2 m_*^2}{(2\pi\hbar^2)^2}$ from the density of states of the lead energies. The above calculation can analogously be carried out for the correlation function in (4.7). One then finds

$$
\begin{aligned}
\langle\tilde{H}_I(0)\tilde{H}_I(t)\rangle \;=\;& c_1\int_{-\infty}^{\infty}\int_{-\infty}^{\infty}d\epsilon_k^L d\epsilon_l^L e^{\frac{i}{\hbar}(\epsilon_k^L-\epsilon_l^L)t}f_L(\epsilon_l^L)(1-f_L(\epsilon_k^L))\times\\
&\times[A'(L\dagger,L)(A(L\dagger,L)-A(L,L\dagger))+A'(L,L\dagger)(A(L,L\dagger)-A(L\dagger,L))]\\
&+c_1\int_{-\infty}^{\infty}\int_{-\infty}^{\infty}d\epsilon_m^R d\epsilon_n^R e^{\frac{i}{\hbar}(\epsilon_m^R-\epsilon_n^R)t}f_R(\epsilon_n^R)(1-f_R(\epsilon_m^R))\times\\
&\times[A'(R\dagger,R)(A(R\dagger,R)-A(R,R\dagger))+A'(R,R\dagger)(A(R,R\dagger)-A(R\dagger,R))]\\
&+c_1\int_{-\infty}^{\infty}\int_{-\infty}^{\infty}d\epsilon_k^L d\epsilon_n^R e^{\frac{i}{\hbar}(\epsilon_k^L-\epsilon_n^R)t}f_R(\epsilon_n^R)(1-f_L(\epsilon_k^L))\times\\
&\times[A'(R\dagger,L)(A(L\dagger,R)-A(R,L\dagger))+A'(L,R\dagger)(A(R,L\dagger)-A(L\dagger,R))]\\
&+c_1\int_{-\infty}^{\infty}\int_{-\infty}^{\infty}d\epsilon_m^R d\epsilon_l^L e^{\frac{i}{\hbar}(\epsilon_m^R-\epsilon_l^L)t}f_L(\epsilon_l^L)(1-f_R(\epsilon_m^R))\times\\
&\times[A'(L\dagger,R)(A(R\dagger,L)-A(L,R\dagger))+A'(R,L\dagger)(A(L,R\dagger)-A(R\dagger,L))]\ .
\end{aligned}
\tag{4.15}
$$

4.3 General case

In order to calculate the $\Gamma^{(+)}$-rates, we have to plug equation (4.14) in (4.6), multiply everything out and evaluate all integrals. These integrals are all of the same form

$$
c_1\int_0^{\infty}dt\int_{-\infty}^{\infty}d\epsilon_1\int_{-\infty}^{\infty}d\epsilon_2 e^{\frac{i}{\hbar}(\epsilon_1-\epsilon_2\pm 2\delta)t}\frac{1}{\epsilon_1-\epsilon_a}\frac{1}{\epsilon_2-\epsilon_b}f_1(\epsilon_1)(1-f_2(\epsilon_2))\ , \tag{4.16}
$$

where the exponent of the exponential function will be called iat with $a=\frac{1}{\hbar}(\epsilon_1-\epsilon_2\pm 2\delta)$. The $\pm 2\delta$ originates in the ω_{nk} and this term could also vanish in the case where $n=k$. The $+/-$ signs in $\pm 2\delta$ denote ω_{-+} resp. ω_{+-}. Additionally there can of course be other constant prefactors stemming from the Schrieffer-Wolff coefficients. For starters, we carry

out the time integration which uses only the exponential function

$$\begin{aligned}\int_0^\infty dt e^{iat} &= \lim_{\theta\to 0}\int_0^\infty dt e^{iat-\theta t} \\ &= \lim_{\theta\to 0}\left[\frac{e^{iat-\theta t}}{ia-\theta}\right]_{0^+}^\infty \\ &= \lim_{\theta\to 0^+}\frac{1}{-ia+\theta} = \lim_{\theta\to 0^+}\frac{i}{a+i\theta} = \pi\delta(a)\ , \end{aligned} \tag{4.17}$$

where we used the residue theorem in the shorthand notation for poles on the real axis (see e.g. in [35]) in the last step

$$\lim_{\theta\to 0^+}\frac{1}{x+i\theta} = \mathcal{P}\left(\frac{1}{x}\right) - i\pi\delta(x)\ . \tag{4.18}$$

$\mathcal{P}$ denotes the principle value of $\frac{1}{x}$ which is neglected here due to energy conservation [29]. That means that the energies are changed only very slowly due to the Born approximation. The principle value would play a role, if we want to renormalize the frequencies ω_{nk}, which is normally done in the case of bosonic baths. This is not necessary, because our reformulation of $\tilde{H}_I$ is already of second order in the coupling to the leads t_c, whereas in the bosonic case the renormalization of the ω_{nk}s is only of first order in the strength of the dissipative coupling. Consequently we find for the rest of our integral

$$\begin{aligned} &c_1\frac{\pi}{\hbar}\int_{-\infty}^{\infty} d\epsilon_1 \int_{-\infty}^{\infty} d\epsilon_2 \frac{1}{\epsilon_1-\epsilon_a}\frac{1}{\epsilon_2-\epsilon_b}\delta(\epsilon_1-\epsilon_2\pm 2\delta) f_1(\epsilon_1)(1-f_2(\epsilon_2)) = \\ &c_1\frac{\pi}{\hbar}\int_{\infty}^{\infty} d\epsilon_2 \frac{1}{\epsilon_2\mp 2\delta-\epsilon_a}\frac{1}{\epsilon_2-\epsilon_b} f_1(\epsilon_2\mp 2\delta)(1-f_2(\epsilon_2))\ . \end{aligned} \tag{4.19}$$

The $\hbar^{-2}$ from equation (4.6) has also been taken into account here. The application of the residue theorem (again along the lines of [36]) then gives

$$\begin{aligned} &c_1\frac{\pi}{\hbar}\int_{-\infty}^{\infty} d\epsilon_2 \frac{1}{\epsilon_2\mp 2\delta-\epsilon_a}\frac{1}{\epsilon_2-\epsilon_b} f_1(\epsilon_2\mp 2\delta)(1-f_2(\epsilon_2)) = \\ &c_1\frac{\pi}{\hbar}\Bigg\{\frac{\pi i}{\epsilon_b-\epsilon_a\mp 2\delta}\left[f_1(\epsilon_b\mp 2\delta)(1-f_2(\epsilon_b)) - f_1(\epsilon_a)(1-f_2(\epsilon_a\pm 2\delta))\right] \\ &\quad -\frac{2\pi i}{\beta}\sum_{j=0}^{\infty}\frac{1}{\mu_1-\epsilon_a+\frac{\pi i}{\beta}(2j+1)}\frac{1}{\mu_1-\epsilon_b\pm 2\delta+\frac{\pi i}{\beta}(2j+1)}\times \\ &\qquad\times(1-f_2(\mu_1\pm 2\delta+\frac{\pi i}{\beta}(2j+1))) \\ &\quad +\frac{2\pi i}{\beta}\sum_{j=0}^{\infty}\frac{1}{\mu_2\mp 2\delta-\epsilon_a+\frac{\pi i}{\beta}(2j+1)}\frac{1}{\mu_2-\epsilon_b+\frac{\pi i}{\beta}(2j+1)}\times \end{aligned}$$

$$\times f_1(\mu_2 \mp 2\delta + \frac{\pi i}{\beta}(2j+1))\Bigg\} . \tag{4.20}$$

Carrying out the resummation of the Matsubara series [using (B.10) and [37]], which means summing over the poles of the Fermi functions $f(\epsilon)$, we get finally the generic form of *one* single integral in equation (4.6) by

$$\begin{aligned}\Gamma^{(+)} &= c\Bigg\{\frac{i\pi}{\epsilon_b-\epsilon_a\mp 2\delta}[f_1(\epsilon_b\mp 2\delta)(1-f_2(\epsilon_b))-f_1(\epsilon_a)(1-f_2(\epsilon_a\pm 2\delta))] \\ &\quad + \frac{-n_1(\mu_2\mp 2\delta)}{\epsilon_b-\epsilon_a\mp 2\delta}\Bigg[\psi\Bigg(\frac{1}{2}+\frac{i\beta}{2\pi}\Bigg(\epsilon_b\mp 2\delta-\mu_1\Bigg)\Bigg)-\psi\Bigg(\frac{1}{2}+\frac{i\beta}{2\pi}\Bigg(\epsilon_a-\mu_1\Bigg)\Bigg) \\ &\quad -\psi\Bigg(\frac{1}{2}+\frac{i\beta}{2\pi}\Bigg(\epsilon_b-\mu_2\Bigg)\Bigg)+\psi\Bigg(\frac{1}{2}+\frac{i\beta}{2\pi}\Bigg(\epsilon_a\pm 2\delta-\mu_2\Bigg)\Bigg)\Bigg]\Bigg\} ,\end{aligned} \tag{4.21}$$

where $c = c_1\frac{\pi}{\hbar}\frac{t_c^4}{4} = \frac{t_c^4\pi V_{2\mathrm{DEG}}^2 m_*^2}{4\hbar(2\pi\hbar^2)^2}$. The factor $\frac{t_c^4}{4}$ is common in all products of Schrieffer-Wolff coefficients and very important for the order of magnitude. One can express the coupling to the leads t_c by $t_c = \sqrt{\frac{g}{8\pi^2}}\cdot\frac{E_F}{n}$, where g is a conductance in terms of the quantum conductance, E_F is the Fermi energy of the leads and n is the number of electrons in the leads. Consequently, c is then changed to $c = \frac{t_c^2 g}{32\pi\hbar}$. The energy changes ϵ_a and ϵ_b contain varying combinations of ϵ_β, ϵ_α and ϵ_{as}. Due to the multitude of possibilities for virtual transitions, each element of the Redfield tensor contains a number of terms of this generic structure. In the above equations, the terms containing the Fermi function $f(\epsilon)$ only play a role close to resonance and can be neglected inside the Coulomb Blockade [38]. The energies in these Fermi functions are dominated by ϵ_α and ϵ_β, that means that one is far away from our transport window between $-\delta$ and δ. The $n_{L/R}$s represent Bose functions for the electron-hole pairs (excitons) that are generated by the cotunneling processes. The ψs denote Digamma functions and hence diverge logarithmically at low temperatures. So, the final, generic result for *one* integral of (4.6) is

$$\Gamma^{(+)} = c\,\frac{-n_1(\mu_2\mp 2\delta)}{\epsilon_b-\epsilon_a\mp 2\delta}\left[\ln\left(\frac{\epsilon_b-\mu_1\mp 2\delta}{\epsilon_a-\mu_1}\right)+\ln\left(\frac{\epsilon_a-\mu_2\pm 2\delta}{\epsilon_b-\mu_2}\right)\right] . \tag{4.22}$$

If one does the completely analogous calculation for $\Gamma^{(-)}$, one yields the form of *one* integral in equation (4.7) by

$$\Gamma^{(-)} = c\,\frac{-n_2(\mu_1\pm 2\delta)}{\epsilon_b-\epsilon_a\mp 2\delta}\left[\ln\left(\frac{\epsilon_a-\mu_1}{\epsilon_b-\mu_1\mp 2\delta}\right)+\ln\left(\frac{\epsilon_b-\mu_2}{\epsilon_a-\mu_2\pm 2\delta}\right)\right] . \tag{4.23}$$

In both cases ($\Gamma^{(+)}$ and $\Gamma^{(-)}$) one normally has to sum up 64 terms to get one $\Gamma^{(\pm)}_{lmnk}$. This is too tedious for a complete manual treatment, so these sums have been implemented in Maple V (Release 7). All other used special rules for these integrals can be found in Appendix C. With the implementation, it was also possible to analyze the behaviour of the Redfield tensor elements and therefore of the relaxation and dephasing rates. By solving

equation (4.4), one finds that the off-diagonal elements of the reduced density matrix decay towards zero on a time scale τ_ϕ (dephasing time) whereas the diagonal elements of the reduced density matrix equilibrate on a time scale τ_r (relaxation time).

In general, one has to find the eigenvalues of R [see below in (4.24)] to get the relaxation and dephasing rates. This becomes clear, if we write equation (4.4) in another way

$$\frac{d}{dt}\vec{\rho}(t) = -R\vec{\rho}(t), \tag{4.24}$$

where the reduced density matrix $\rho(t) = \begin{pmatrix} \rho_{++}(t) & \rho_{+-}(t) \\ \rho_{-+}(t) & \rho_{--}(t) \end{pmatrix}$ is written as $\vec{\rho}(t) = \begin{pmatrix} \rho_{++}(t) \\ \rho_{--}(t) \\ \rho_{+-}(t) \\ \rho_{-+}(t) \end{pmatrix}$.

(4.24) can be reformulated as

$$\frac{d}{dt}\vec{\rho}(t) = -BCB^{-1}\vec{\rho}(t), \tag{4.25}$$

where C is a diagonal matrix, or since B and B^{-1} are time-independent

$$\frac{d}{dt}B^{-1}\vec{\rho}(t) = -CB^{-1}\vec{\rho}(t). \tag{4.26}$$

This differential equation for $B^{-1}\vec{\rho}$ can be solved via a usual exponential Ansatz and we find

$$\vec{\rho}(t) = Be^{-Ct}B^{-1}\vec{\rho}(0). \tag{4.27}$$

We can now analyze the components of $\vec{\rho}$. The time evolution of the diagonal elements of the reduced density matrix (i.e. the relaxation rates) are given by the first two diagonal entries of C. The last two diagonal entries then describe the time evolution of the off-diagonal elements of the reduced density matrix (i.e. the dephasing rates). The plots in Chapter 6 have been made by only considering the leading order in the coupling t_c to the leads in the relaxation or dephasing rates.

4.4 Atomic limit

In order to find the relaxation and dephasing rates in the case of our Gedanken experiment, we first calculate all nonvanishing elements of the Redfield tensor R_{nmkl}

$$\begin{aligned}
R_{++++} &= \Gamma^{(+)}_{+--+} + \Gamma^{(-)}_{+--+} && (4.28)\\
R_{----} &= \Gamma^{(+)}_{-++-} + \Gamma^{(-)}_{-++-} && (4.29)\\
R_{++--} &= -\Gamma^{(+)}_{-++-} - \Gamma^{(-)}_{-++-} && (4.30)\\
R_{--++} &= -\Gamma^{(+)}_{+--+} - \Gamma^{(-)}_{+--+} && (4.31)\\
R_{+-+-} &= \Gamma^{(+)}_{+--+} + \Gamma^{(-)}_{-++-} + \Gamma^{(+)}_{++++} + \Gamma^{(-)}_{----} - \Gamma^{(+)}_{--++} - \Gamma^{(-)}_{--++} && (4.32)\\
R_{-+-+} &= \Gamma^{(+)}_{-++-} + \Gamma^{(-)}_{+--+} + \Gamma^{(+)}_{----} + \Gamma^{(-)}_{++++} - \Gamma^{(+)}_{++--} - \Gamma^{(-)}_{++--}\ , && (4.33)
\end{aligned}$$

where $\Gamma^{(+)}_{lmnk} = \Gamma^{(-)}_{lmnk}$ and $\Gamma^{(+)}_{++--} = \Gamma^{(+)}_{--++}$.
If we now only consider the diagonal elements of the reduced density matrix (to get the relaxation rate), we find from equation (4.4)

$$\frac{d}{dt}\begin{pmatrix} \rho_{++}(t) \\ \rho_{--}(t) \end{pmatrix} = -\begin{pmatrix} R_{++++} & R_{++--} \\ R_{--++} & R_{----} \end{pmatrix}\begin{pmatrix} \rho_{++}(t) \\ \rho_{--}(t) \end{pmatrix} . \tag{4.34}$$

Diagonalizing the matrix in equation (4.34), we find two relaxation rates: $\Gamma_r = 0$ and $\Gamma_r = R_{++++} + R_{----}$. $\Gamma_r = 0$ means that there is a stationary state and the only nontrivial relaxation channel is described by the other, finite Γ_r.

Analyzing the off-diagonal elements of the reduced density matrix in equation (4.4) leads to the two equations

$$\dot{\rho}_{+-}(t) = -i(\omega_{+-} - iR_{+-+-})\rho_{+-}(t) \tag{4.35}$$
$$\dot{\rho}_{-+}(t) = -i(\omega_{-+} - iR_{-+-+})\rho_{-+}(t) . \tag{4.36}$$

Here, we can directly identify the two dephasing rates by the Rs, but in this specific case $R_{+-+-} = R_{-+-+}$. This means that there is only one dephasing rate $\Gamma_\phi = R_{+-+-}$.

Summarizing our previous results, we found

$$\Gamma_r = 2\,(\Gamma^{(+)}_{+--+} + \Gamma^{(+)}_{-++-}) \tag{4.37}$$
$$\Gamma_\phi = \frac{\Gamma_r}{2} + (\Gamma^{(+)}_{++++} + \Gamma^{(+)}_{----} - 2\Gamma^{(+)}_{++--}) \tag{4.38}$$

where

$$\Gamma^{(+)}_{+--+} = \Gamma^{(-)}_{+--+} = c\,(-n_R(\mu_L + 2\epsilon_{\text{as}}))Z \tag{4.39}$$
$$\Gamma^{(+)}_{-++-} = \Gamma^{(-)}_{-++-} = c\,(n_L(\mu_R - 2\epsilon_{\text{as}}))Z \tag{4.40}$$
$$\Gamma^{(+)}_{++++} = \Gamma^{(-)}_{++++} = c\,k_{\text{B}}T\,Y_1 \tag{4.41}$$
$$\Gamma^{(+)}_{----} = \Gamma^{(-)}_{----} = c\,k_{\text{B}}T\,Y_{-1} \tag{4.42}$$
$$\Gamma^{(+)}_{++--} = \Gamma^{(-)}_{++--} = c\,k_{\text{B}}T\,Y_{1,-1}. \tag{4.43}$$

Z is a function containing several ψ-functions (or logarithms). Y_1, Y_{-1} and $Y_{1,-1}$ are different functions of several ψ'-(Trigamma-) functions (or reciprocals), however, these functions have no temperature dependence. The functions can be found in Appendix D. The most important part of the temperature dependence comes in through the proportionality to T and through the Bose functions $n_{L/R}$. One can generally say, that in the relaxation rate (4.37) are only terms with an energy exchange with the two leads. This can be seen in the function $n_{L/R}$. In the dephasing rate (4.38) are also terms without an energy exchange with the environment.

We will now compare these results to the relaxation and dephasing rates in the Spin-Boson case [39, 40]

$$\Gamma_r = \sin^2\theta\; J(\delta)\coth\left(\frac{2\delta}{2k_{\text{B}}T}\right) \tag{4.44}$$
$$\Gamma_\phi = \frac{\Gamma_r}{2} + 2\pi\alpha\frac{k_{\text{B}}T}{\hbar}\;\cos^2\theta\;, \tag{4.45}$$

where 2δ is again the level splitting. J is the spectral density of a bosonic bath; this function measures the phase space and depends logarithmically from the energies of the intermediate states. θ is the angle between the z-axis and an effective magnetic field $\vec{B}_{\text{eff}}$. This magnetic field is responsible for the bias in an NMR system [41]. The α is the dimensionless strength of the interaction of the two-state system with the environment. The α dependent term occurs only if the bath is composed of ohmic oscillators for low frequencies. This term also describes dephasing processes without spin flip.

We can observe similar structures in the relaxation rates (4.37) and (4.44), if we write the relaxation rate like this

$$\Gamma_r = \sigma \ \kappa \ \coth\left(\frac{2\delta}{2k_{\text{B}}T}\right) \ . \tag{4.46}$$

Here we identified a cross section σ with Z or $\cos^2\theta$. κ is a spectral density, which means that it denotes c or J. The coth function can be identified in (4.37), if one writes the sum of the Bose functions $n_{L/R}$ in another way.

The comparison of the dephasing rates is even shorter, because the structure looks immediately similar in both cases. The first term is the same and in the second term is a linear temperature dependence combined with again something that looks like a cross section [Ys in (4.38)].

We observe universal features in the relaxation and dephasing rates of our model compared to the Spin-Boson model, but we considered two distinct fermionic baths. In general these two baths also have different chemical potentials and therefore we usually are in a non-equilibrium situation. Our Gedanken experiment would correspond to pure dephasing in the Spin-Boson model, but we observe relaxation, which is due to the *two* baths and a voltage source.

Chapter 5

Calculation of the current

In this chapter, we will derive an expression for the cotunneling current through our double-dot system, because we would like to describe an easy accessible, natural observable which is potentially useful for an easy probing of timescales. Transport spectroscopy is one of the most important and powerful techniques to characterize such mesoscopic systems.

Following the fundamental relation from [42]

$$I(t) = -e\,\frac{i}{\hbar}\int\limits_{-\infty}^{t} dt'\,\langle\left[\dot{N}_L(t),\tilde{H}_I(t')\right]\rangle\ , \tag{5.1}$$

one can deduce a relation for the time-dependent current through the coupled double-dot system. $\dot{N}_L$ is the time derivative of the particle counting operator N_L on the left dot in the interaction picture (5.2). In order to determine an expression for the current through the whole system, both dots are equivalent.

We start with the calculation of $\dot{N}_L$, where we have to consider the commutator between N_L and $\tilde{H}_I(t)$

$$\begin{aligned}
\dot{N}_L(t) &= \frac{i}{\hbar}\left[\tilde{H}_I(t),N_L\right] \\
&= \frac{i}{\hbar}\begin{pmatrix}1&0\\0&0\end{pmatrix}\left[\tilde{H}_{I,++}(t),N_L\right]+\frac{i}{\hbar}\begin{pmatrix}0&0\\0&1\end{pmatrix}\left[\tilde{H}_{I,--}(t),N_L\right] \\
&+ \frac{i}{\hbar}\begin{pmatrix}0&1\\0&0\end{pmatrix}\left[\tilde{H}_{I,+-}(t),N_L\right]+\frac{i}{\hbar}\begin{pmatrix}0&0\\1&0\end{pmatrix}\left[\tilde{H}_{I,-+}(t),N_L\right]\ ,
\end{aligned} \tag{5.2}$$

where

$$\begin{aligned}
\tilde{H}_{I,cd}(t) &= e^{\frac{i}{\hbar}\omega_{cd}t}\Big\{e^{\frac{i}{\hbar}(\epsilon_m^R-\epsilon_n^R)t}\left[A(R\dagger,R,cd)b_m^{R\dagger}b_n^R+A(R,R\dagger,cd)b_n^Rb_m^{R\dagger}\right] \\
&+ e^{\frac{i}{\hbar}(\epsilon_k^L-\epsilon_l^L)t}\left[A(L\dagger,L,cd)b_k^{L\dagger}b_l^L+A(L,L\dagger,cd)b_l^Lb_k^{L\dagger}\right] \\
&+ e^{\frac{i}{\hbar}(\epsilon_m^R-\epsilon_l^L)t}\left[A(R\dagger,L,cd)b_m^{R\dagger}b_l^L+A(L,R\dagger,cd)b_l^Lb_m^{R\dagger}\right] \\
&+ e^{\frac{i}{\hbar}(\epsilon_k^L-\epsilon_n^R)t}\left[A(L\dagger,R,cd)b_k^{L\dagger}b_n^R+A(R,L\dagger,cd)b_n^Rb_k^{L\dagger}\right]\Big\}\ .
\end{aligned} \tag{5.3}$$

Evaluating all important commutators we finally yield for $\dot{N}_L$

$$\begin{aligned}
\dot{N}_L(t) &= \frac{i}{\hbar}\Bigg\{\begin{pmatrix} 1 & 0 \\ 0 & 0 \end{pmatrix}\Bigg(e^{\frac{i}{\hbar}(\epsilon_m^R-\epsilon_l^L)t} b_m^{R\dagger} b_l^L \left[A(R\dagger, L, ++) - A(L, R\dagger, ++)\right] \\
&\quad + e^{\frac{i}{\hbar}(\epsilon_k^L-\epsilon_n^R)t} b_k^{L\dagger} b_n^R \left[A(R, L\dagger, ++) - A(L\dagger, R, ++)\right]\Bigg) \\
&\quad + \begin{pmatrix} 0 & 0 \\ 0 & 1 \end{pmatrix}\Bigg(e^{\frac{i}{\hbar}(\epsilon_m^R-\epsilon_l^L)t} b_m^{R\dagger} b_l^L \left[A(R\dagger, L, --) - A(L, R\dagger, --)\right] \\
&\quad + e^{\frac{i}{\hbar}(\epsilon_k^L-\epsilon_n^R)t} b_k^{L\dagger} b_n^R \left[A(R, L\dagger, --) - A(L\dagger, R, --)\right]\Bigg) \\
&\quad + e^{\frac{i}{\hbar}2\delta t}\begin{pmatrix} 0 & 1 \\ 0 & 0 \end{pmatrix}\Bigg(e^{\frac{i}{\hbar}(\epsilon_m^R-\epsilon_l^L)t} b_m^{R\dagger} b_l^L \left[A(R\dagger, L, +-) - A(L, R\dagger, +-)\right] \\
&\quad + e^{\frac{i}{\hbar}(\epsilon_k^L-\epsilon_n^R)t} b_k^{L\dagger} b_n^R \left[A(R, L\dagger, +-) - A(L\dagger, R, +-)\right]\Bigg) \\
&\quad + e^{-\frac{i}{\hbar}2\delta t}\begin{pmatrix} 0 & 0 \\ 1 & 0 \end{pmatrix}\Bigg(e^{\frac{i}{\hbar}(\epsilon_m^R-\epsilon_l^L)t} b_m^{R\dagger} b_l^L \left[A(R\dagger, L, -+) - A(L, R\dagger, -+)\right] \\
&\quad + e^{\frac{i}{\hbar}(\epsilon_k^L-\epsilon_n^R)t} b_k^{L\dagger} b_n^R \left[A(R, L\dagger, -+) - A(L\dagger, R, -+)\right]\Bigg)\Bigg\}\,, \qquad (5.4)
\end{aligned}$$

where only processes play a role that act on *both* leads. Carrying out some straightforward manipulations, we finally get the following expression for the commutator between $\dot{N}_L(t)$ and $\tilde{H}_I(t')$

$$\begin{aligned}
\left[\dot{N}_L(t), \tilde{H}_I(t')\right] &= \begin{pmatrix} 1 & 0 \\ 0 & 0 \end{pmatrix}\left(\left[\dot{N}_{L,++}(t), \tilde{H}_{I,++}(t')\right]\right. \\
&\quad \left. + \dot{N}_{L,+-}(t)\tilde{H}_{I,-+}(t') - \tilde{H}_{I,+-}(t')\dot{N}_{L,-+}(t)\right) \\
&\quad + \begin{pmatrix} 0 & 0 \\ 0 & 1 \end{pmatrix}\left(\left[\dot{N}_{L,--}(t), \tilde{H}_{I,--}(t')\right]\right. \\
&\quad \left. + \dot{N}_{L,-+}(t)\tilde{H}_{I,+-}(t') - \tilde{H}_{I,-+}(t')\dot{N}_{L,+-}(t)\right) \\
&\quad + \begin{pmatrix} 0 & 1 \\ 0 & 0 \end{pmatrix}\left(\dot{N}_{L,++}(t)\tilde{H}_{I,+-}(t') - \tilde{H}_{I,++}(t')\dot{N}_{L,+-}(t)\right. \\
&\quad \left. + \dot{N}_{L,+-}(t)\tilde{H}_{I,--}(t') - \tilde{H}_{I,+-}(t')\dot{N}_{L,--}(t)\right) \\
&\quad + \begin{pmatrix} 0 & 0 \\ 1 & 0 \end{pmatrix}\left(\dot{N}_{L,--}(t)\tilde{H}_{I,-+}(t') - \tilde{H}_{I,--}(t')\dot{N}_{L,-+}(t)\right. \\
&\quad \left. + \dot{N}_{L,-+}(t)\tilde{H}_{I,++}(t') - \tilde{H}_{I,-+}(t')\dot{N}_{L,++}(t)\right)\,. \qquad (5.5)
\end{aligned}$$

This means that we again have to sum up a lot of terms. If we continue to calculate equation (5.1) by carrying out the time integration [using again (4.18)] and rotating back

to the Schrödinger picture, we yield for the summands in general

$$\int_{-\infty}^{0} dt \int_{-\infty}^{\infty} d\epsilon_1 \int_{-\infty}^{\infty} d\epsilon_2 \dot{N}_{L,ab} \tilde{H}_{I,cd} =$$

$$i\pi c_1 \Bigg\{ \int_{-\infty}^{\infty} d\epsilon_l^L f_R(\epsilon_l^L \mp 2\delta)(1 - f_L(\epsilon_l^L)) \left[A(R\dagger, L, ab) - A(L, R\dagger, ab)\right] \times$$

$$\times \left[A(L\dagger, R, cd) - A(R, L\dagger, cd)\right]$$

$$- \int_{-\infty}^{\infty} d\epsilon_{m'}^R f_L(\epsilon_{m'}^R \mp 2\delta)(1 - f_R(\epsilon_{m'}^R)) \left[A(R\dagger, L, cd) - A(L, R\dagger, cd)\right] \times$$

$$\times \left[A(L\dagger, R, ab) - A(R, L\dagger, ab)\right] \Bigg\} \tag{5.6}$$

$$\int_{-\infty}^{0} dt \int_{-\infty}^{\infty} d\epsilon_1 \int_{-\infty}^{\infty} d\epsilon_2 \tilde{H}_{I,cd} \dot{N}_{L,ab} =$$

$$i\pi c_1 \Bigg\{ - \int_{-\infty}^{\infty} d\epsilon_m^R f_R(\epsilon_m^R)(1 - f_L(\epsilon_m^R \mp 2\delta)) \left[A(R\dagger, L, cd) - A(L, R\dagger, cd)\right] \times$$

$$\times \left[A(L\dagger, R, ab) - A(R, L\dagger, ab)\right]$$

$$+ \int_{-\infty}^{\infty} d\epsilon_{l'}^L f_L(\epsilon_{l'}^L)(1 - f_R(\epsilon_{l'}^L \mp 2\delta)) \left[A(R\dagger, L, ab) - A(L, R\dagger, ab)\right] \times$$

$$\times \left[A(L\dagger, R, cd) - A(R, L\dagger, cd)\right] \Bigg\} , \tag{5.7}$$

where $\mp 2\delta$ comes from ω_{-+} resp. ω_{+-}. These terms have the same structure as the $\Gamma^{(+)}$ and $\Gamma^{(-)}$ rates and can be treated like them using the Maple V implementation. Even most constants are the same if one takes the constants in equation (5.1) into account, there is only one additional e for the electron charge, which makes sense to get a current (charge/time).

If one considers a total expression for $I(t)$, one has to look at equation (5.5) and calculate all terms along the lines of (5.6) and (5.7). Then one finally gets the four matrix elements of $I(t)$. Only terms containing processes that act on *both* leads appear in the matrix elements of $I(t)$. This current expression itself can of course not be observed in an experiment. For this purpose we calculate the expectation value of $I(t)$ by

$$\langle I(t) \rangle = tr[\rho(t) I(t)] \tag{5.8}$$

$$= tr\left[\begin{pmatrix} \rho_{++}(t) & \rho_{+-}(t) \\ \rho_{-+}(t) & \rho_{--}(t) \end{pmatrix} \begin{pmatrix} I_{++}(t) & I_{+-}(t) \\ I_{-+}(t) & I_{--}(t) \end{pmatrix} \right] \tag{5.9}$$

$$= \rho_{++}(t) I_{++}(t) + \rho_{+-}(t) I_{-+}(t) + \rho_{-+}(t) I_{+-}(t) + \rho_{--}(t) I_{--}(t) \; . \tag{5.10}$$

In this expression, relaxation and dephasing rates cannot be found explicitly, but implicitly (via the time-dependent elements of ρ) they provide the adjustment of a dynamical equilibrium.

In the case of a stationary current (usually considered in literature), we have to consider

$$I_{\rm st} := \langle I(t) \rangle = \rho_{++,{\rm st}} I_{++}(t) + \rho_{--,{\rm st}} I_{--}(t) \ , \tag{5.11}$$

where

$$\rho_{++,{\rm st}} = \frac{R_{++--}}{R_{++--} - R_{++++}} \tag{5.12}$$

$$\rho_{--,{\rm st}} = \frac{R_{--++}}{R_{--++} - R_{----}} \tag{5.13}$$

are the stationary occupation probabilities for the ground state $|\gamma, -\rangle$ and the excited state $|\gamma, +\rangle$. They are determined by equation (4.4), where the off-diagonal elements of the density matrix ρ vanish.

Using the nonstationary Bloch-Redfield equations (4.4), we can also study the nonstationary current [see equations (5.8)-(5.10)].

Chapter 6

Discussion of the results

After the evaluation of the Redfield tensor elements and the current calculation, we analyze the physical properties of the system.

The aim is to get as much information as possible out of these results and to understand the fundamental processes, which control the system behaviour.

For having definite numbers, we have to make some realistic assumptions based on the experiments [43, 44, 45] concerning the size of energies, which are used as parameters in this theory.

First of all, one could choose the 2D volume V_{2DEG} of the two leads as 10^{-12} m^2. This seems reasonable, if one contemplates SEM pictures of lateral double dot systems. Another assumption concerns the Fermi energy E_F of the leads, which we take as 5 meV. The number of electrons per volume in the leads is $n/V_{\mathrm{2DEG}} = 1.7 \cdot 10^{15}$ m^{-2}. Together with $g = 0.1$ in terms of the quantum conductance, one finally yields $t_c = 1.21$ mK for the coupling of the dots to the leads (the formula for t_c can be found in Chapter 4.3). The distances to the nearest other states apart from the two-state system are $\epsilon_\beta = 11$ K and $\epsilon_\alpha = 9$ K, describing the charging energies which are needed to put another electron into the system or to get one electron out of the system. The intrinsic energies are taken to be in the ranges $\epsilon_{\mathrm{as}} = -0.5..0.5$ K and $\gamma = -0.5..0.5$ K. Furthermore, the average chemical potential is mostly given by $\mu_{\mathrm{av}} = 0.88$ K and the temperature is normally set to $T = 0.14$ K.
All energies are given in the unit Kelvin K (1 K $=$ 86.17 μeV/k$_{\mathrm{B}}$).
In the following sections, the relaxation time, the dephasing time and the stationary current are presented depending on the different parameters: internal energies ϵ_{as} and γ, temperature T and bias voltage $V = \mu_R - \mu_L$. The section concerning conductance treats only the bias voltage dependence of the (differential) conductance.

6.1 Relaxation times

6.1.1 Internal energies

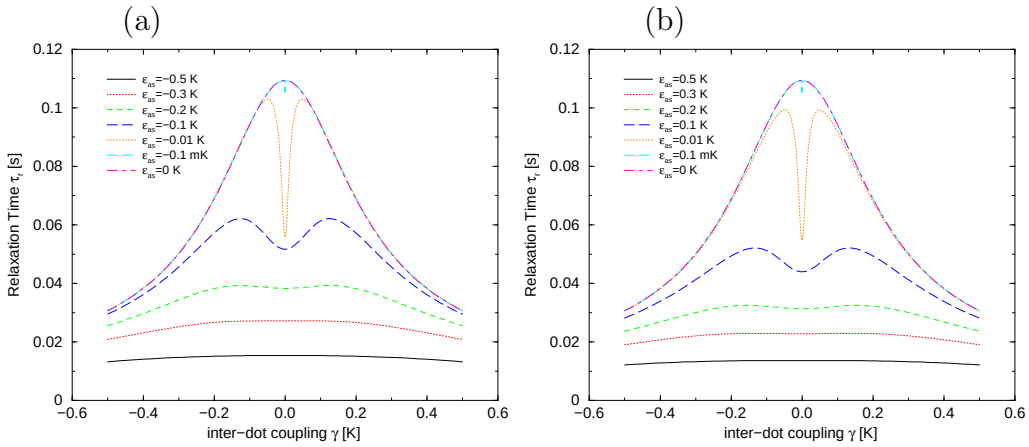

Figure 6.1: Relaxation times τ_r for different values of ϵ_{as} when the coupling strength γ is varied (with $T = 0.14$ K, $V = 0.06$ K and $\mu_{\text{av}} = 0.88$ K)

As one can see in Figure 6.1, the relaxation time τ_r is in the order of ms. This means that an incoherent mixture in the relevant two-state system decays very slowly due to cotunneling. Processes involving phonons are probably orders of magnitudes faster.

The curves are axially symmetric to the y-axis at $\gamma = 0$. If the absolute value of the asymmetry energy ϵ_{as} is equal, the curves for $\epsilon_{\text{as}} > 0$ and for $\epsilon_{\text{as}} < 0$ are also very similar to each other, but not equal. This is due to the positive bias voltage ($V = \mu_R - \mu_L$), which is applied here. That means that the energy levels with positive ϵ_{as} in the double-dot are closer to the Fermi energies of the leads, and hence they can decay easier.

The relaxation time rises as the absolute value of ϵ_{as} drops down. By approaching the $\epsilon_{\text{as}} = 0$ line, one adds another symmetry to the system. Because of this symmetry the states are more stable and the relaxation time reaches its maximum value.
Another characteristic part of the diagrams is the low-γ-minimum in the curve for $|\epsilon_{\text{as}}| = 0.1$ K. This minimum is probably due to the changing from the "atomic" to the "molecular" basis, which is done by varying the inter-dot coupling strength. The height of this dip is also connected to the absolute value of ϵ_{as}, for smaller ϵ_{as} the dip is huger and sharper. For $\epsilon_{\text{as}} = 0$, no dip can be resolved. But this also makes sense, because only the inter-dot coupling contributes to the changing to the molecular basis. By varying γ, transport channels can be controlled, this will be discussed near Figure 6.9, because the relaxation processes contribute to the electron transport.

After a specific point in γ, the relaxation times goes down with bigger absolute values of γ. This can be understood by again looking at the Spin-Boson case. One would expect such a decrease for higher values of the tunnel coupling $\cos^2\theta$ [see equation (4.44)].

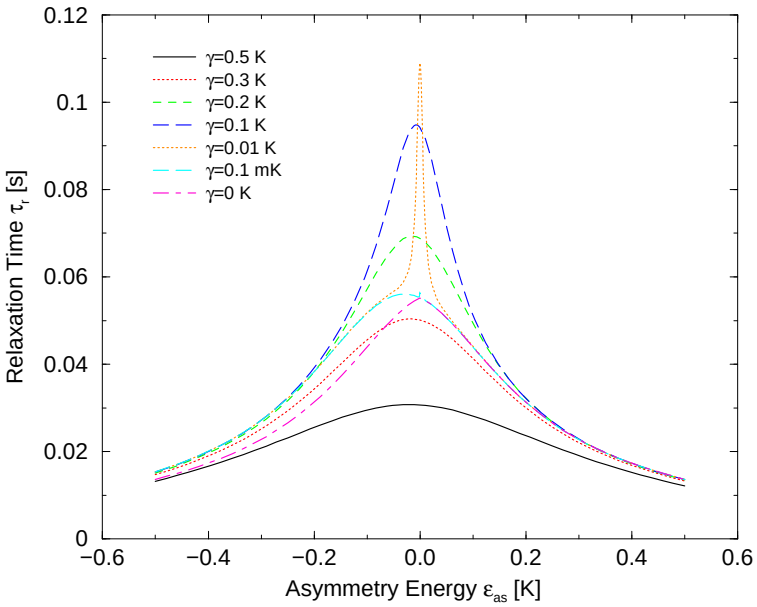

Figure 6.2: Relaxation times τ_r for different values of γ when the asymmetry energy ϵ_{as} is varied (with $T = 0.14$ K, $V = 0.06$ K and $\mu_{\text{av}} = 0.88$ K)

Figure 6.2 shows the relaxation time τ_r as a function of the asymmetry energy ϵ_{as}. One observes a small asymmetry at $\epsilon_{\text{as}} = 0$, which is due to the applied small bias voltage. For small negative ϵ_{as}, the relaxation times are higher, a possible explanation for this is given in Section 6.7.

This figure is fully consistent with Figure 6.1, because for large absolute values of ϵ_{as} the relaxation time goes down. A maximum in the relaxation time arises for small absolute values of ϵ_{as}, because the system is very stable there.

The behaviour, which is described in Figures 6.1 and 6.2, could be understood as a cross-over between a symmetric regime ($\epsilon_{\text{as}} < \gamma$) and an asymmetric regime ($\epsilon_{\text{as}} \geq \gamma$).

6.1.2 Temperature

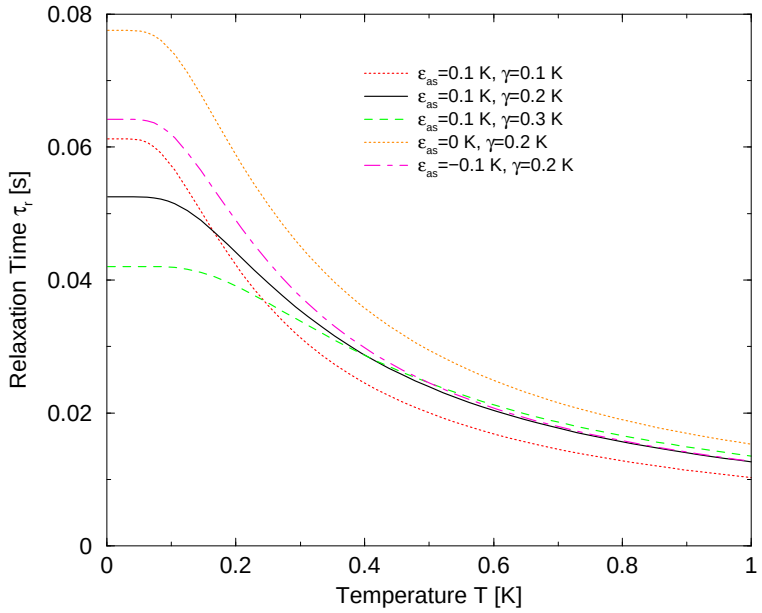

Figure 6.3: Relaxation times τ_r for different values of ϵ_{as} and γ when the temperature T is varied (with $V = 0.06$ K and $\mu_{\text{av}} = 0.88$ K)

In Figure 6.3, the temperature dependence of τ_r is shown. One can observe the following properties. Firstly one denotes that the relaxation time τ_r decreases for higher temperatures. This was of course to be expected, because the Pauli blocking is smaller at higher temperatures and more energy levels are available for relaxation processes. This temperature dependence is similar to the Spin-Boson case, but there bunching effects are the reason for the temperature dependence.
We plotted only positive γs, because τ_r does not depend on the sign of γ.

And one expects from Figure 6.1, that for $\epsilon_{\text{as}} < 0$ the relaxation time should be greater than for $\epsilon_{\text{as}} > 0$. This can be confirmed in Figure 6.3, if one compares the curves with $|\epsilon_{\text{as}}| = 0.1$ K and $\gamma = 0.2$ K. At higher temperatures these both curves approach each other. This can of course be explained by the contributing energy scales, because the voltage was only $V = 0.06$ K compared to a rising temperature. Consequently if T is much bigger than V, the temperature is dominating.

One also observes that the graph for $\gamma = 0.1$ K starts at a higher τ_r and drops down with rising temperature very rapidly, crossing some other lines during this process. On the other hand, the curve for $\gamma = 0.3$ K starts at the lowest τ_r and crosses some other lines. With an analogy to the Spin-Boson case (see Chapter 4), this can be understood. The $\coth\left(\frac{2\delta}{2T}\right)$ grows stronger, if δ is small. This means that the exciton states are occupied faster than for big δ. The curve for $\epsilon_{\text{as}} = 0$ is again the highest. This is consistent with our observation for Figure 6.1 that the symmetry makes the system more stable against relaxation.

6.1.3 Bias voltage

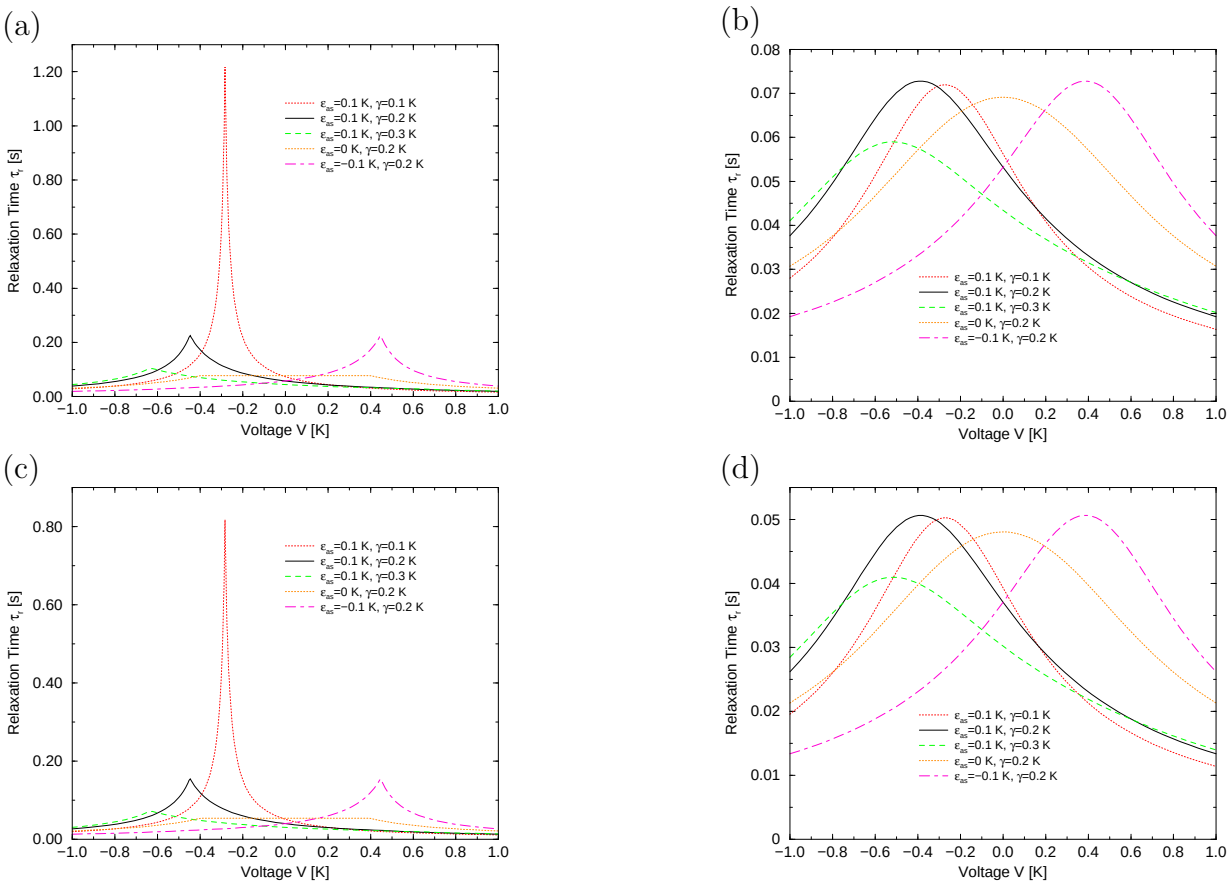

Figure 6.4: Relaxation times τ_r for different values of ϵ_{as} and γ when the bias voltage V is varied: (a) at $T = 0.1$ mK, $\mu_{\text{av}} = 0.88$ K, (b) at $T = 0.14$ K, $\mu_{\text{av}} = 0.88$ K, (c) at $T = 0.1$ mK, $\mu_{\text{av}} = 4$ K and (d) at $T = 0.14$ K, $\mu_{\text{av}} = 4$ K

In Figure 6.4, one can observe that the plots at the same temperature remain qualitatively equal, only the absolute value of τ_r changes for a different μ_{av}. This is due to the fact, that the bandwidth enters the evaluation logarithmically (similar to the Kondo effect). The peak positions for different temperatures are also the same, but for the higher temperature ($T = 0.14$ K) the peaks are smeared out. And there is also an axial symmetry in ϵ_{as} which is also evident in the curve for $\epsilon_{\text{as}} = 0$ itself, because this the only curve which is symmetric to $V = 0$. The appearance of the peaks could be explained by the naive picture, that there is one configuration, which is the most stable for some given parameters (see Section 6.7). For positive ϵ_{as} the maximum must be in the negative voltage range. The peak position depends on the value of δ. At $\pm 2\delta$ the peak maximum can be found, this is consistent with all other voltage dependencies that follow (Figures 6.8, 6.13, 6.14 and 6.15).

6.2 Dephasing times

6.2.1 Internal energies

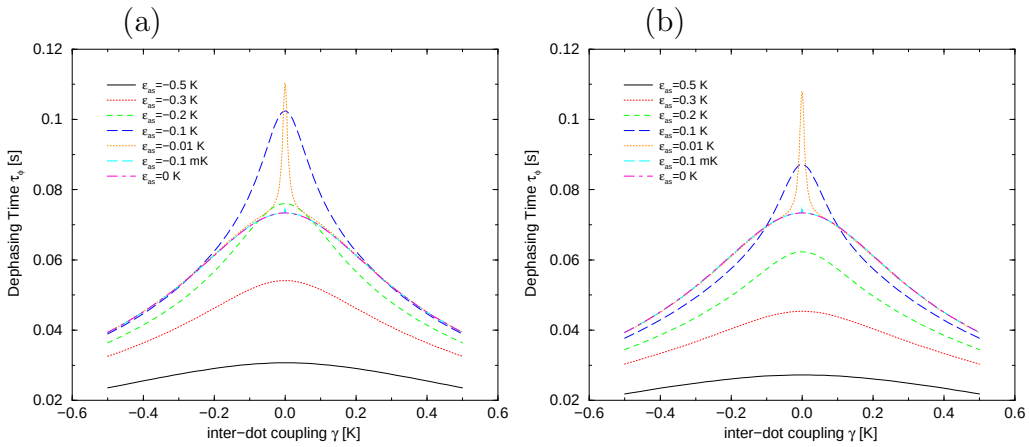

Figure 6.5: Dephasing times τ_ϕ for different values of $\epsilon_{\rm as}$ when the coupling strength γ is varied (with $T = 0.14$ K, $V = 0.06$ K and $\mu_{\rm av} = 0.88$ K)

In Figure 6.5, there is a very obvious asymmetry of the dephasing time τ_ϕ depending on the coupling strength γ, if one compares both pictures. This is again due to the asymmetry energy $\epsilon_{\rm as}$ and the voltage V. The dephasing times are higher for negative $\epsilon_{\rm as}$, because there is a small, positive voltage. For smaller absolute values of $\epsilon_{\rm as}$ ($|\epsilon_{\rm as}| = 0.01$ K or $|\epsilon_{\rm as}| = 0.1$ mK) the curves in (a) and (b) look more and more identical.

The appearance of only one peak (compared to Figure 6.1) could be explained by an analogy with the Spin-Boson model, if we take "flipless" processes into account. These processes, that are linear in the temperature T, occur only in the dephasing [compare e.g. to (4.38)] and have no energy transfer to the leads. The appearance of these terms has also been checked in the Maple V implementation. The curve for $\epsilon_{\rm as} = 0$ is the highest one, but this cannot be resolved in these pictures. In general are more symmetric configurations more stable concerning "flipless" processes. This can also be understood, if one analyzes the formulae for Y_1, Y_{-1} and $Y_{1,-1}$ (representing the "flipless" processes) in Appendix D. The fact that the maxima can be found at $\gamma = 0$ is probably due to the small number of processes remaining for these localized "atomic states".

The whole figure is a combination of the relaxation time features (see Figure 6.1; minimum at $\gamma = 0$) and the "flipless" features (maximum at $\gamma = 0$).

Since the figures for the γ dependence (Figures 6.1, 6.5 and 6.9) are symmetric to $\gamma = 0$, we used only positive γs for the other figures.

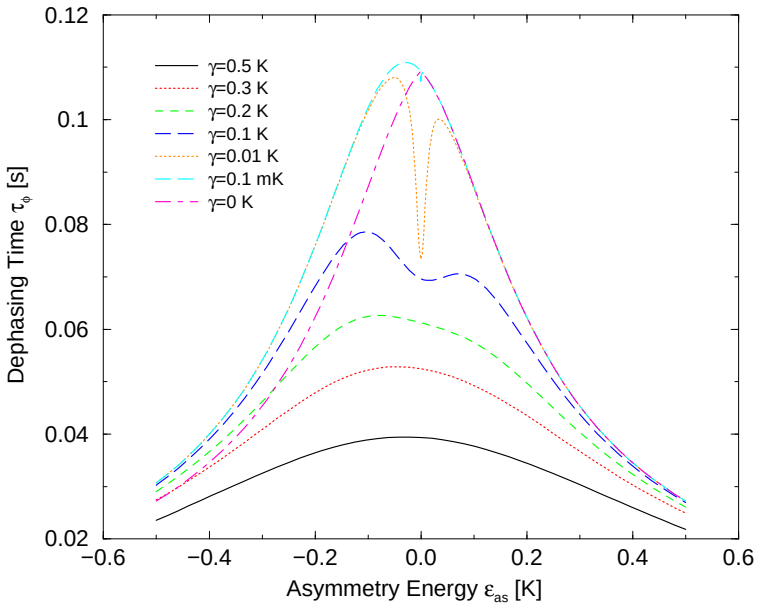

Figure 6.6: Dephasing times τ_ϕ for different values of γ when the asymmetry energy ϵ_{as} is varied (with $T = 0.14$ K, $V = 0.06$ K and $\mu_{\text{av}} = 0.88$ K)

Figure 6.6 shows the dependence of the dephasing time τ_ϕ on the other internal energy, the asymmetry energy ϵ_{as}. Like in Figure 6.2, one observes an asymmetry at $\epsilon_{\text{as}} = 0$, which is again due to the small bias voltage (see Section 6.7 for an explanation).

The other features, which we can find here, have been seen in Figure 6.2. For example, Figures 6.5 and 6.6 are consistent with each other, and we can again see the already mentioned cross-over between a symmetric regime ($\epsilon_{\text{as}} < \gamma$) and an asymmetric regime ($\epsilon_{\text{as}} \geq \gamma$).

6.2.2 Temperature

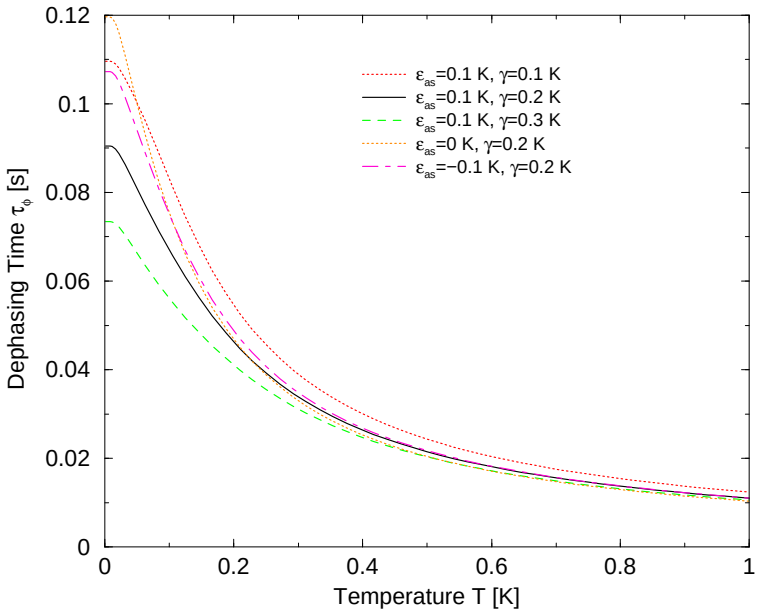

Figure 6.7: Dephasing times τ_ϕ for different values of ϵ_{as} and γ when the temperature T is varied (with $V = 0.06$ K and $\mu_{\text{av}} = 0.88$ K)

The temperature dependence of the dephasing time is plotted in Figure 6.7. And here one observes a similar behaviour like in the Spin-Boson case. This is due to the fact that in the analytical expressions for the dephasing rate are some terms that are linear in T, which cannot be seen for the relaxation rate. This again the same argument, which we used to explain Figure 6.5. "Flipless" processes occur for the dephasing.

Additionally, the already mentioned asymmetry for equal values of the absolute values of ϵ_{as} is again visible (due to the interaction of ϵ_{as} and V).

6.2.3 Bias voltage

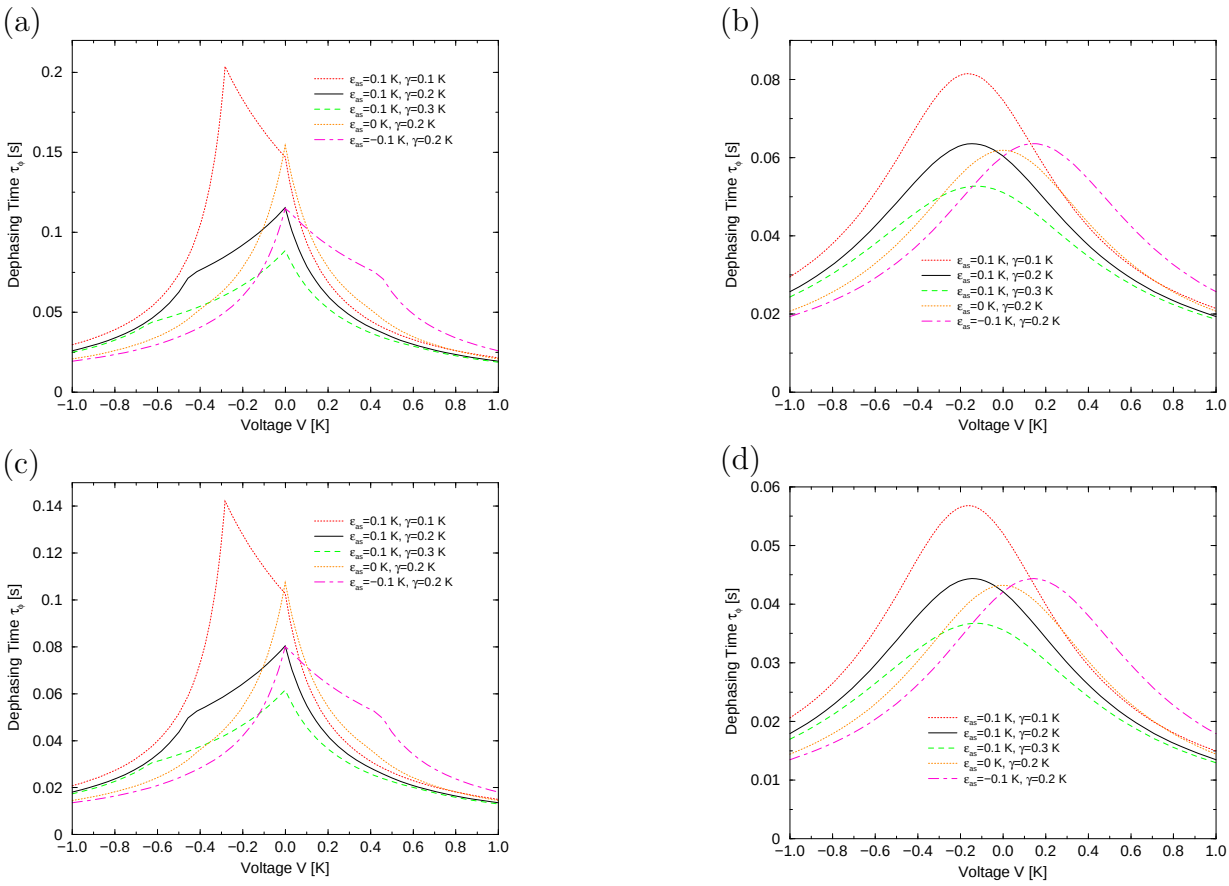

Figure 6.8: Dephasing times τ_ϕ for different values of ϵ_{as} and γ when the bias voltage V is varied: (a) at $T = 0.1$ mK, $\mu_{\text{av}} = 0.88$ K, (b) at $T = 0.14$ K, $\mu_{\text{av}} = 0.88$ K, (c) at $T = 0.1$ mK, $\mu_{\text{av}} = 4$ K and (d) at $T = 0.14$ K, $\mu_{\text{av}} = 4$ K

There is again a symmetry for the different absolute values of ϵ_{as}, while the peaks for themselves are not symmetric at all. For the low temperature the peaks have two important points, one at $V = 0$ and one depending on ϵ_{as} and γ (at $\pm 2\delta$). The peak at $V = 0$ is probably again due to "flipless" processes, because such a structure does not show up in the relaxation time. An explanation could be that these non-diagonal dephasing processes are driven by a finite voltage. So for $V = 0$, these processes are suppressed and the only phase space, where "flipless" processes could survive, stems from the thermal smearing out of the Fermi edge. But this phase space is very small. The peak at $\pm 2\delta$ has its origin in the relaxation processes which have been discussed earlier (see Figure 6.4).

As already seen in Figure 6.4, the curves for the voltage dependence in Figure 6.8 are smeared out for the higher temperature (in (b) and (d)), so that the characteristics of the two peaks were lost.

6.3 Stationary current

6.3.1 Internal energies

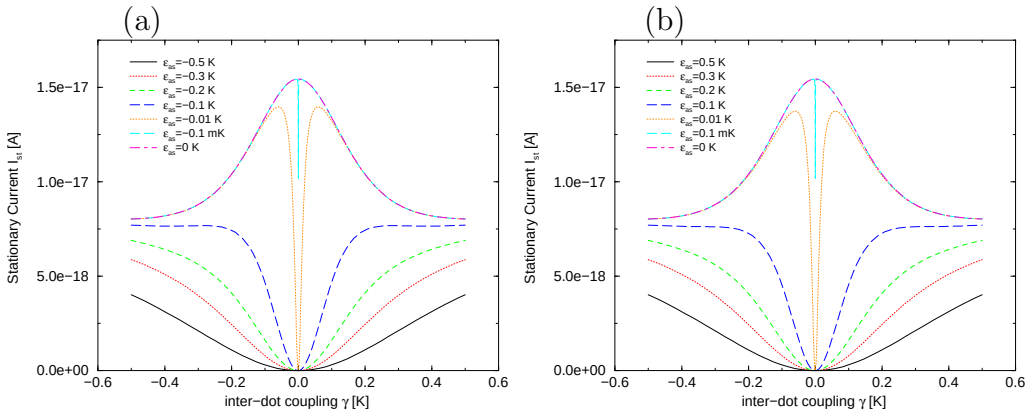

Figure 6.9: Stationary current I_{st} for different values of ϵ_{as} when the coupling strength γ is varied (with $T = 0.14$ K, $V = 0.06$ K and $\mu_{\mathrm{av}} = 0.88$ K)

In Figure 6.9, there is a symmetry for the same absolute values of ϵ_{as}. This can be explained by the fact that the current expression [see equation (5.11)] is a sum of products of two quantities with an odd symmetry (current rates and stationary occupation probability). One would furthermore expect that at $\gamma = 0$ there is no stationary current at all, but for $\epsilon_{\mathrm{as}} = 0$ there seems to be a current maximum. This is not the full truth, because the dip downwards for $\epsilon_{\mathrm{as}} = 0$ cannot be resolved in these pictures. If one looks very closely at this curve, one finds a very narrow dip that reaches $I_{\mathrm{st}} = 0$ at $\gamma = 0$. The stationary current for $\gamma = 0$ at a finite voltage must be 0, because there is no connection between the two dots then. That means that there is no way for an electron to go through the double-dot structure.

Another feature is that a saturation value for the stationary current in dependence of the coupling strength seems to exist (at about $I_{0,\mathrm{st}} = 7.5 \cdot 10^{-18}$ A). This is probably due to the regime $\gamma \gg V$ where the curves show the saturation. For $\gamma \gg V$ only one of the two states is in the "transport window" (can be used for electron transport). We can also see a current of $2I_{0,\mathrm{st}}$ in the curve for $\epsilon_{\mathrm{as}} = 0$. That means we can distinguish between three transport regimes: the first for $\gamma < \frac{t_c^2}{2\delta}$ where there is no current $I = 0$, a second regime $\frac{t_c^2}{2\delta} < \gamma < \sqrt{\frac{V^2}{4} - \epsilon_{\mathrm{as}}^2}$ where there is $I = 2I_{0,\mathrm{st}}$ and the third for $\gamma > \sqrt{\frac{V^2}{4} - \epsilon_{\mathrm{as}}^2}$ where there is a current of $I_{\mathrm{st}} = I_{0,\mathrm{st}}$. In the first regime, no molecular state can be used for electron transport. Both molecular states are used in the second case, whereas in the third case there is only one molecular state available for charge transport. The reason, why we talk about transport channels or states like in the Landauer-Büttiker formalism, is that we look at coherent transport through the whole double-dot due to cotunneling, where there is no dephasing during the transport through the structure.

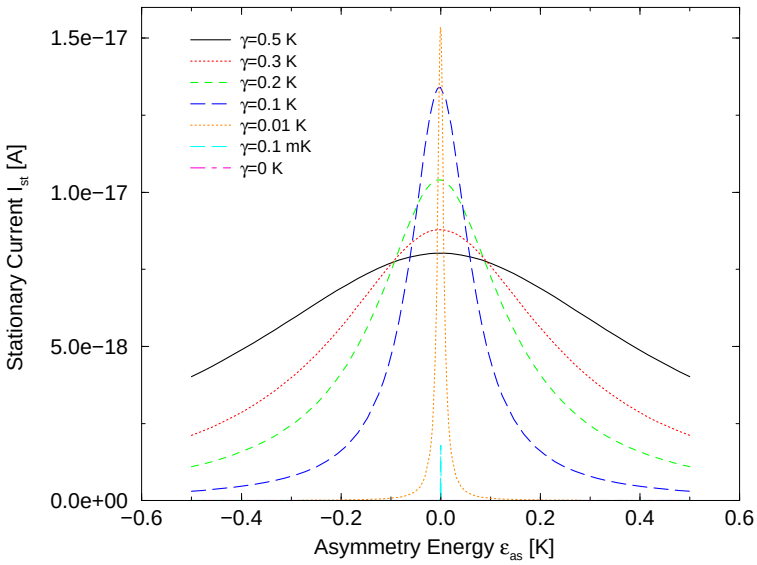

Figure 6.10: Stationary current I_{st} for different values of γ when the asymmetry energy ϵ_{as} is varied (with $T = 0.14$ K, $V = 0.06$ K and $\mu_{\mathrm{av}} = 0.88$ K)

Figure 6.10 shows the dependence of the stationary current from ϵ_{as} as the second internal energy. This figure is a full confirmation of the interpretation of Figure 6.9. First of all, the plot is symmetric to $\epsilon_{\mathrm{as}} = 0$, which was also the case before due to the fact that the stationary current is the sum of products of quantities with odd symmetry (see discussion of Figure 6.9).

The appearance of a single peak at $\epsilon_{\mathrm{as}} = 0$ makes sense, because the condition for charge transport is ideal there (only *one* effective level due to the symmetry between the two dots), there is no further blocking in the double-dot system.

We recognize again the three transport regimes, but they are not so clear now, because there are some "intermediate" values of γ, therefore we see all possibilities. If we start the discussion for the $\gamma = 0$ curve, we see that the stattionary current is exactly $I_{\mathrm{st}} = 0$, as we would expect. For growing, but small values of γ, the maximum at $\epsilon_{\mathrm{as}} = 0$ reaches the highest value $I_{\mathrm{st}} = 2I_{0,\mathrm{st}}$ at about $1.5 \cdot 10^{-17}$ A (like in Figure 6.9). If we increase γ further, the height of the peak goes down again and saturates at $I_{\mathrm{st}} = I_{0,\mathrm{st}} \approx 7.5 \cdot 10^{-18}$ A.

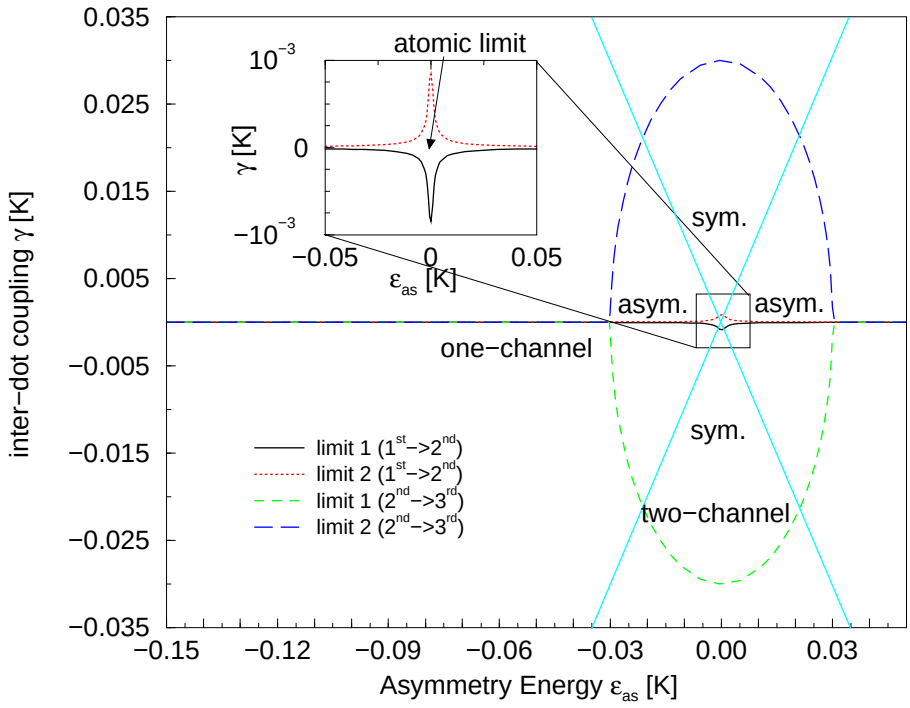

Figure 6.11: Limits for the three transport regimes with the parameters $V = 0.06$ K and $t_c = 1.21$ mK

Figure 6.11 shows the limits for the three transport regimes, which we identified in Figures 6.9 and 6.10 with the same parameters. The three regimes are

- atomic limit $\gamma < \frac{t_c^2}{2\delta}$;
- two-channel $\frac{t_c^2}{2\delta} < \gamma < \sqrt{\frac{V^2}{4} - \epsilon_{\text{as}}^2}$;
- one-channel $\gamma > \sqrt{\frac{V^2}{4} - \epsilon_{\text{as}}^2}$.

Thus we get the following, possible criteria for the limits

- between the 1^{st} and the 2^{nd} regime
  - limit 1: $\gamma = -\sqrt{-\frac{\epsilon_{\text{as}}^2}{2} + \frac{1}{2}\sqrt{\epsilon_{\text{as}}^4 + t_c^4}}$;
  - limit 2: $\gamma = \sqrt{-\frac{\epsilon_{\text{as}}^2}{2} + \frac{1}{2}\sqrt{\epsilon_{\text{as}}^4 + t_c^4}}$;
- between the 2^{nd} and the 3^{rd} regime
  - limit 1: $\gamma = -\sqrt{\frac{V^2}{4} - \epsilon_{\text{as}}^2}$;
  - limit 2: $\gamma = \sqrt{\frac{V^2}{4} - \epsilon_{\text{as}}^2}$.

6.3.2 Temperature

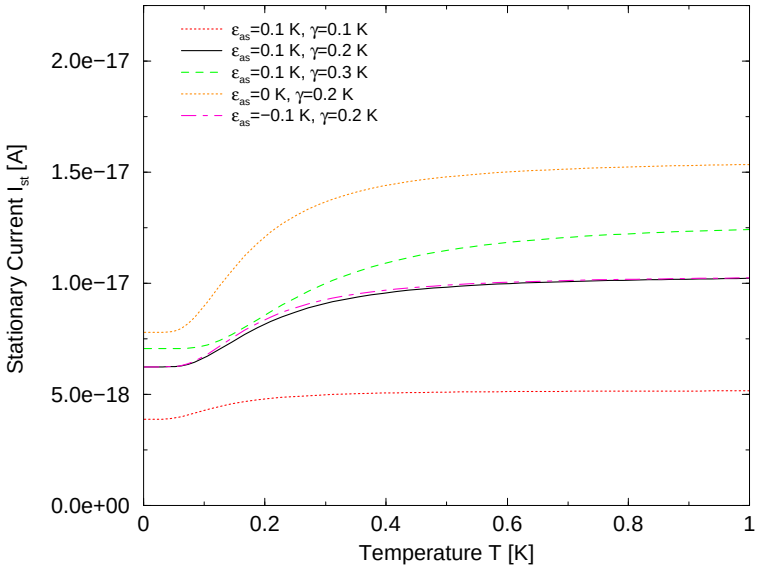

Figure 6.12: Stationary current I_{st} for different values of ϵ_{as} and γ when the temperature T is varied (with $V = 0.06$ K and $\mu_{\mathrm{av}} = 0.88$ K)

At a specific value of the temperature, the curves for the stationary current begin to rise very fast in Figure 6.12, whereas they were nearly constant for low Ts. Even the sometimes very different behaviour for the possibilities of the absolute values of ϵ_{as} does not occur. This can be unterstood from Figure 6.13, where both are nearly equal for a sufficient small voltage.

The values for the stationary current seem to saturate for each configuration of the ϵ_{as} and the γ seperately. This saturation can be understood, if we look again at the regime, which we use. Here we rise the temperature more and more, that means that both molecular states can be used for electron transport. This results in a higher current. Using this argument, we also explain, why the curves saturate seperately: the molecular states (i.e. the level spacing 2δ) are different for each configuration (only for $|\epsilon_{\mathrm{as}}| = 0.1$ K and $\gamma = 0.2$ K the curves are identical).

6.3.3 Bias voltage

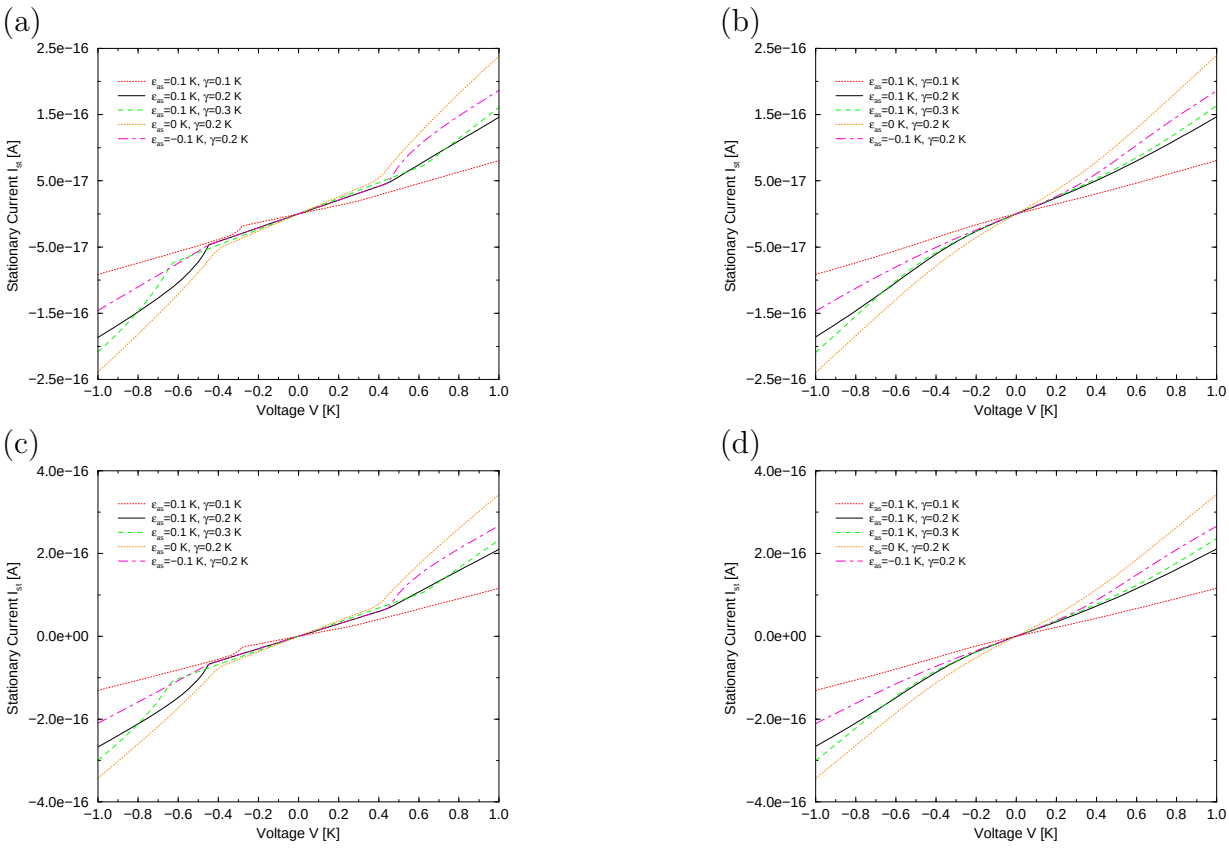

Figure 6.13: Stationary I_{st}-V characteristics for different values of ϵ_{as} and γ: (a) at $T = 0.1$ mK, $\mu_{\mathrm{av}} = 0.88$ K, (b) at $T = 0.14$ K, $\mu_{\mathrm{av}} = 0.88$ K, (c) at $T = 0.1$ mK, $\mu_{\mathrm{av}} = 4$ K and (d) at $T = 0.14$ K, $\mu_{\mathrm{av}} = 4$ K

As already observed, also in Figure 6.13 the curves are smeared out for the high temperature and for $\epsilon_{\mathrm{as}} = \gamma = 0.1$ K, the current-voltage dependence really looks like a linear resistor. In (b) and (d) it is hard to recognize the edges that are there. In the other two pictures ((a) and (c)), there is again the asymmetry for negative and positive voltages and again the curves for the same absolute value of ϵ_{as} and γ are somehow symmetric with respect to $V = 0$.

The position of these edges is again determined by $\pm 2\delta$. This has already been observed in the voltage dependence of the relaxation (Figure 6.4) and the dephasing time (Figure 6.8). The edges seem to stem from the relaxation processes, because they can be observed whenever relaxation plays a role. At these edges, an additional transport channel disappears (at -2δ) or reappears (at $+2\delta$). Between -2δ and $+2\delta$, only one molecular state is available for electron transport through the double-dot structure.

6.4 Conductance and differential conductance

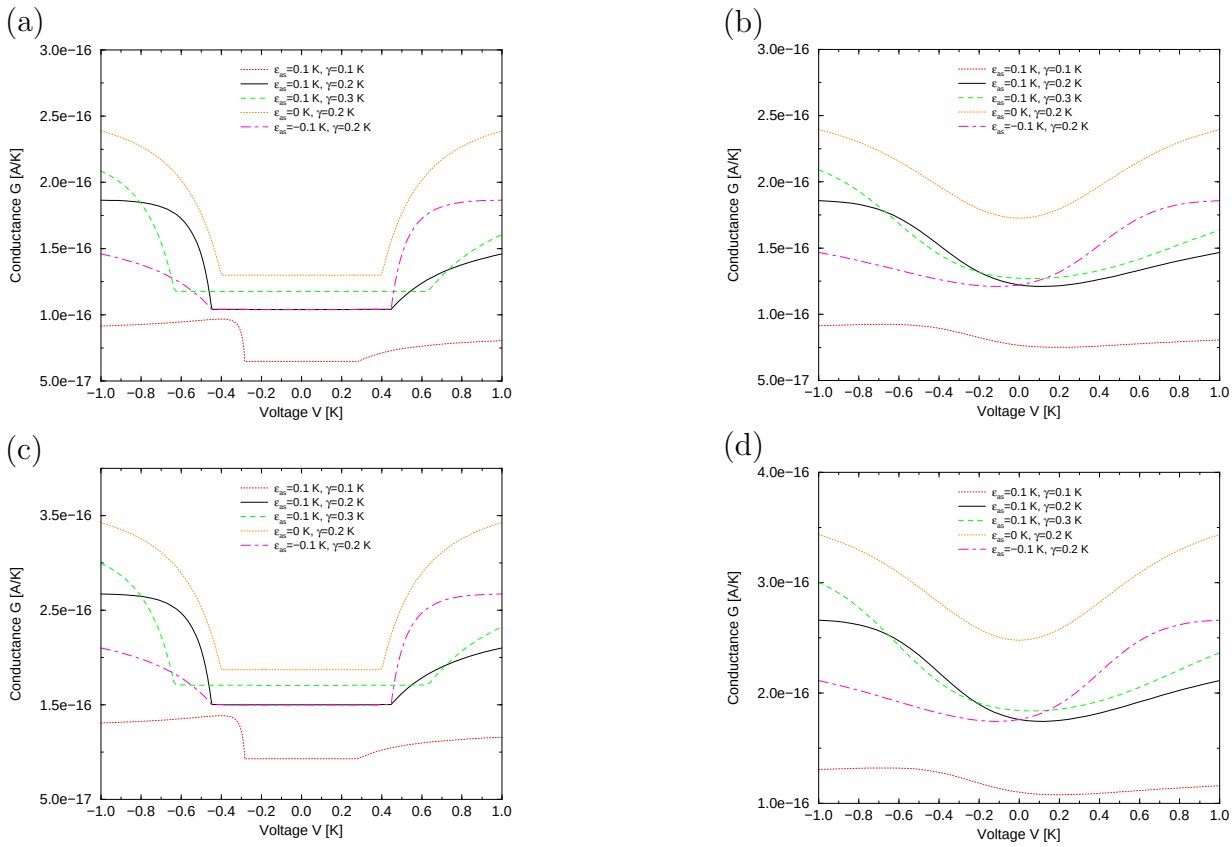

Figure 6.14: Conductance G for different values of ϵ_{as} and γ when the bias voltage V is varied: (a) at $T = 0.1$ mK, $\mu_{\text{av}} = 0.88$ K, (b) at $T = 0.14$ K, $\mu_{\text{av}} = 0.88$ K, (c) at $T = 0.1$ mK, $\mu_{\text{av}} = 4$ K and (d) at $T = 0.14$ K, $\mu_{\text{av}} = 4$ K

In Figure 6.14, one sees again a very obvious asymmetry with respect to $V = 0$. Again this effect is smeared out for the high temperature. For the low temperature, one observes a minimal level with two flanks each that behave very differently. The width of this minimal level is given by 4δ, which is consistent with the other pictures of voltage dependencies.

Especially in (a) and (c), it becomes obvious that the asymmetry energy is responsible for the characteristics of the curves, because only the symmetric curve ($\epsilon_{\text{as}} = 0$) is fully symmetric to $V = 0$. These pictures highlight the behaviour that was observed in Figure 6.13. A later interpretation of Figure 6.16 will probably explain this feature.

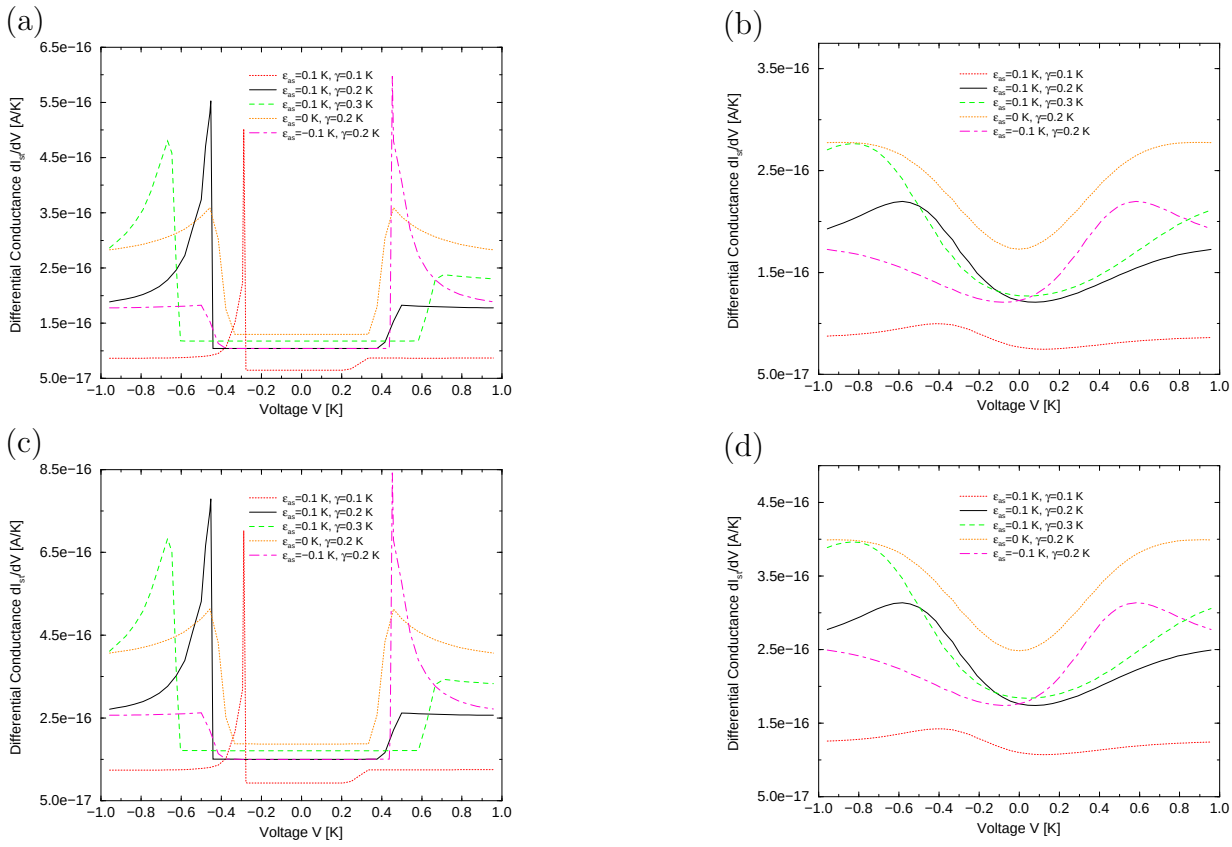

Figure 6.15: Differential conductance dI_{st}/dV for different values of ϵ_{as} and γ when the bias voltage V is varied: (a) at $T = 0.1$ mK, $\mu_{\mathrm{av}} = 0.88$ K, (b) at $T = 0.14$ K, $\mu_{\mathrm{av}} = 0.88$ K, (c) at $T = 0.1$ mK, $\mu_{\mathrm{av}} = 4$ K and (d) at $T = 0.14$ K, $\mu_{\mathrm{av}} = 4$ K

The differential conductance as a function of the voltage (Figure 6.15) shows mainly the same characteristics as already presented in Figure 6.14. All features are even clearer: the asymmetry in the voltage, the symmetry for special values (same absolute value) and the smearing out due to a higher temperature.

The asymmetries can only be observed, if $\epsilon_{\mathrm{as}} \neq 0$. And the positions of the peaks are again determined by the values of δ, they can be found at $\pm 2\delta$.

These features seem to be very general, because they appear in all "voltage plots". The asymmetries can maybe be explained by looking at the difference of the stationary occupation probability $\rho_{++,\mathrm{st}} - \rho_{--,\mathrm{st}}$ (Figure 6.16). Further plausible explanations for these effects are stability arguments in the double-dot systems (see Section 6.7).

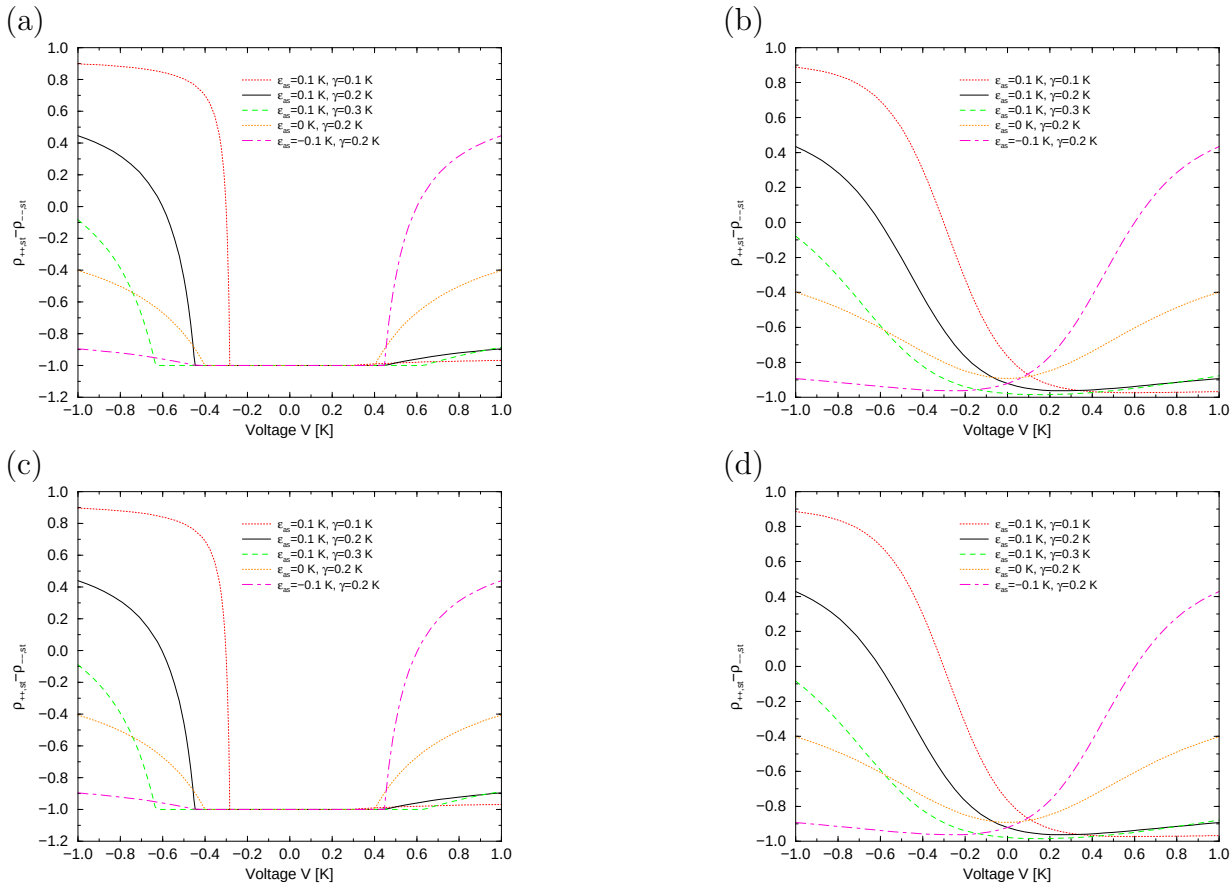

Figure 6.16: Difference of the stationary occupation probabilities $\rho_{++,\mathrm{st}} - \rho_{--,\mathrm{st}}$ for different values of ϵ_{as} and γ when the bias voltage V is varied: (a) at $T = 0.1$ mK, $\mu_{\mathrm{av}} = 0.88$ K, (b) at $T = 0.14$ K, $\mu_{\mathrm{av}} = 0.88$ K, (c) at $T = 0.1$ mK, $\mu_{\mathrm{av}} = 4$ K and (d) at $T = 0.14$ K, $\mu_{\mathrm{av}} = 4$ K

In Figure 6.16, the difference in the stationary occupation probabilities is shown. And all features which were not clear in Figures 6.14 and 6.15 seem to make sense now, because all of the already mentioned characteristics do also appear in this figure. In Chapter 5, where one can find a part of the analytical expression for the current, there is a trace over a product of a current matrix and the (stationary) reduced density matrix [equation (5.11)]. That means that this behaviour is due to the behaviour of the occupation probabilities which are given by Bloch-Redfield theory. A further discussion can be found in Section 6.7. The time evolution, that leads to the here observed behaviour of the difference of two stationary elements of the reduced density matrix, can be found in Figure 6.17 for some given parameters.

6.5 Time-dependent elements of the reduced density matrix

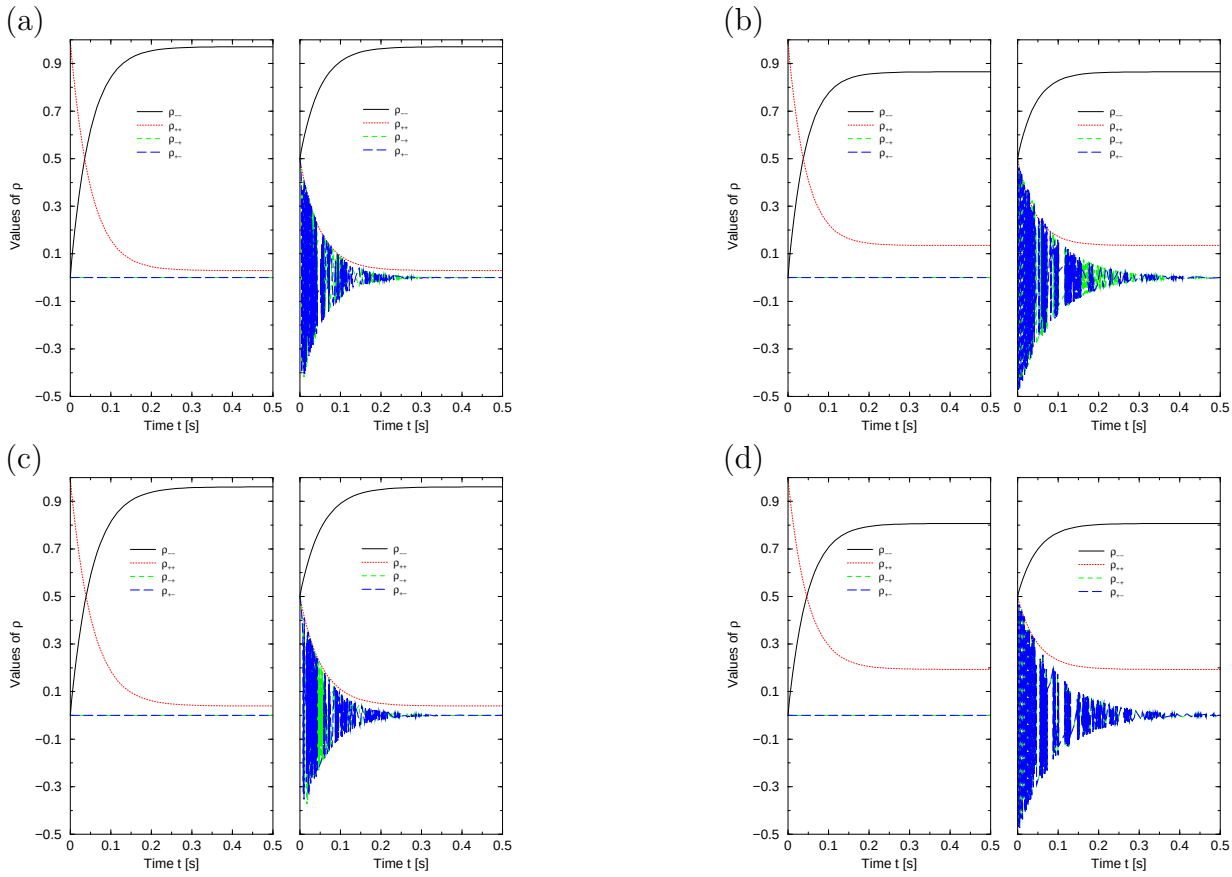

Figure 6.17: Time-dependent reduced density matrix elements with the following parameters: $T = 0.14$ K, $\mu_{\text{av}} = 0.88$ K and $\epsilon_{\text{as}} = 0.1$ K; additionally (a) $V = 0.06$ K, $\gamma = 0.2$ K, (b) $V = 0.06$ K, $\gamma = 0$ K, (c) $V = 0$ K, $\gamma = 0.2$ K and (d) $V = 0$ K, $\gamma = 0$ K

In Figure 6.17, the behaviour of the time-dependent elements of the reduced density matrix is shown. The left part of the pictures is the case of a pure state (the execited state ρ_{++}) as a starting value ρ_0 for the reduced density matrix. The right part shows the behaviour, if we start in a superpostion of states ($\rho_{++} = \rho_{--} = \rho_{+-} = \rho_{-+} = 0.5$). For long times, the left and the right part of each picture must coincide. This happens to be the case for all pictures.

The common behaviour for all pictures is that after a while the ground state (ρ_{--}) is mainly occupied, the occupation probability for the excited state is small, whereas the off-diagonal density matrix elements ρ_{+-} and ρ_{-+} remain to be 0 or dephase with coherent oscillations to 0 (depending on the starting value ρ_0). Although the oscillations seem to be frequency modulated, a closer look reveals clear oscillations with an angular frequency

of about $\frac{2\delta}{\hbar}$.
The occupation probability for the ground state never reaches 1 fully, this can explained by the temperature of $T = 0.14$ K. That means that there is always a small thermal excitation.

There are also some differences between the pictures, which are due to the different voltages and the different γs. If we compare (a) and (b), we observe that the occupation probability for the ground state is significantly smaller in (b), where there is no inter-dot coupling γ. This probably due to the fact that it is harder to relax to the ground state, if the dots are not coupled. Another difference is that the dephasing processes in (a) are faster than in (b), this can be explained with the same argument. A comparison between (c) and (d) gives the same observations. The difference between (a) and (c) and between (b) and (d) is that the occupation probability for the ground state is even smaller in (c) and (d) than in (a) and (b). The only reason can be the finite voltage $V = 0.06$ K that makes it easier to relax to the ground state in (a) and (b).
The stationary values for the elements of the reduced density matrix, which can be observed here, can also be found in Figure 6.16(b), if one subtracts $\rho_{--,\mathrm{st}}$ from $\rho_{++,\mathrm{st}}$.

6.6 Time-dependent current

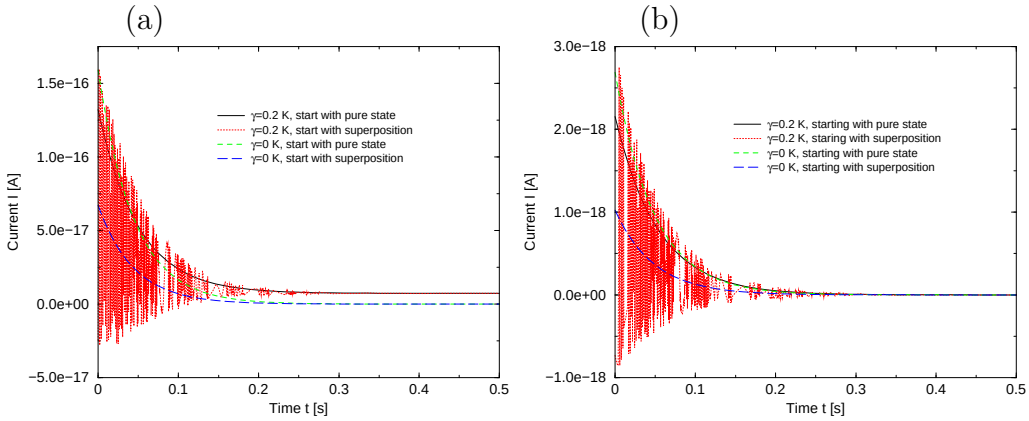

Figure 6.18: Time-dependent cotunneling current through the double dot system with the parameters: $T = 0.14$ K, $\mu_{\mathrm{av}} = 0.88$ K and $\epsilon_{\mathrm{as}} = 0.1$ K; additionally (a) $V = 0.06$ K and (b) $V = 0$ K

Figure 6.18 shows the time-evolution of the current through the double-dot system. The results are consistent with Figure 6.17.

(a) and (b) look very similar with one major difference: for $\gamma = 0.2$ K there remains a finite current in (a), but this is clear, because there is also a finite voltage $V = 0.06$ K and a finite temperature $T = 0.14$ K as well.

The common results in (a) and (b) are that there are only oscillations (not frequency modulated) in the current for $\gamma = 0.2$ K and if one starts in a superposition. All other

curves approximate their saturation value directly. Mostly this saturation value is 0, because there should not be a stationary current, if $\gamma = 0$ or $V = 0$. This has also been discussed before. Note that we only discuss the expectation value of the current. In order to observe this current, one first has to study the shot-noise associated with it, which is potentially very high.

6.7 Stability in the double dot system

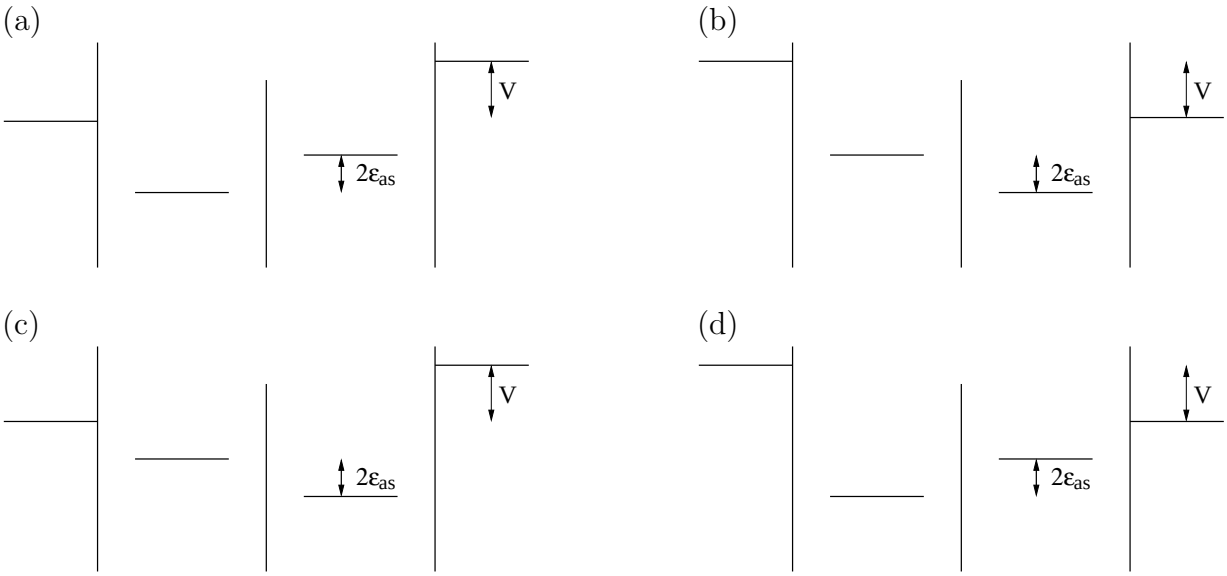

Figure 6.19: Sketches for some "stable" [(a) and (b)] and "unstable" [(c) and (d)] configurations in the asymmetry energy ϵ_{as} and the voltage V

Figure 6.19 shows some possible configurations for the asymmetry energy ϵ_{as} and the voltage V.

In pictures (a) and (b), ϵ_{as} and V have opposite signs, whereas in (c) and (d) they have the same sign. In (a) and (b) one directly observes that the distances to the Fermi energies of the leads are huge, because the levels are aligned in the same way. Thus these configurations are somehow stable. For the other two pictures (c) and (d), the opposite argument holds. The levels of the dots and of the leads are not aligned in the same way, that means that there is one very small distance to the Fermi energy of one lead. Therefore the configurations in (c) and (d) are unstable.

On the other hand, if the voltage is increased immensely, then the above mentioned alignment makes charge transport easier, because the levels in the dots do not block each other, which would be true for (c) and (d). This can be observed in Figures 6.13, 6.14 and 6.15.

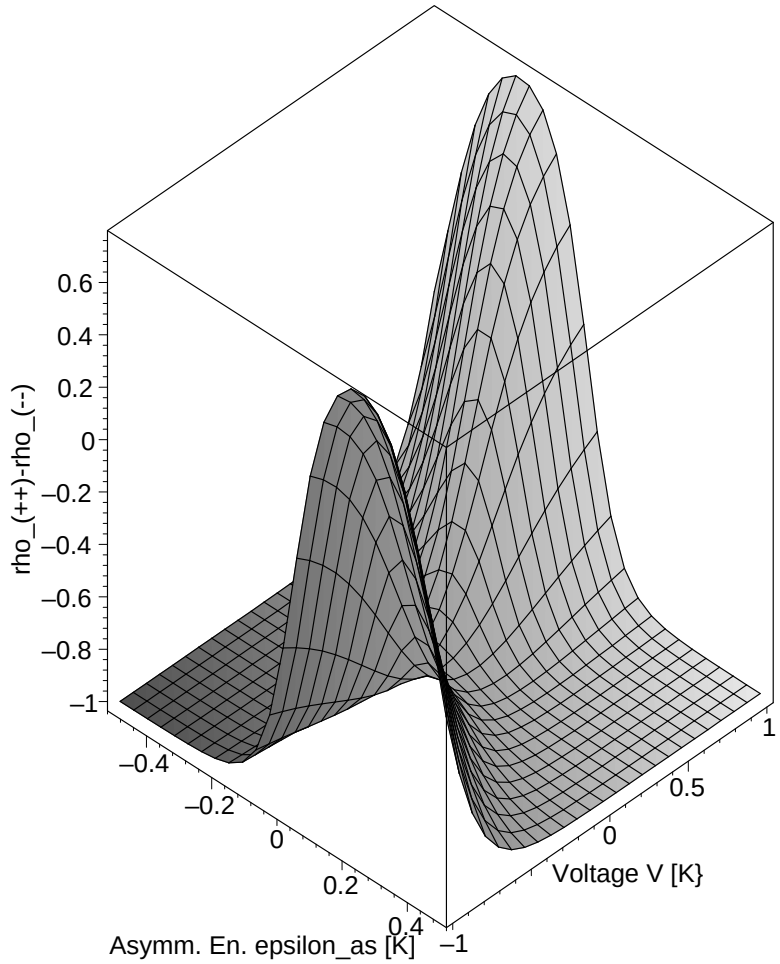

Figure 6.20: Difference of the stationary occupation probabilities $\rho_{++,\mathrm{st}} - \rho_{--,\mathrm{st}}$ for varying ϵ_{as} and V with $\gamma = 0.2$ K, $\epsilon_\beta = 11$ K, $\epsilon_\alpha = 9$ K, $T = 0.14$ K and $\mu_{\mathrm{av}} = 0.88$ K

In Figure 6.20, we can make the observation, which we expected due to the stability arguments that have been mentioned on the last page. For different signs in the asymmetry energy ϵ_{as} and the voltage V, one gets a more stable excited state $|\gamma, +\rangle$. If the signs are the same, the ground state $|\gamma, -\rangle$ is nearly fully occupied in the stationary case.

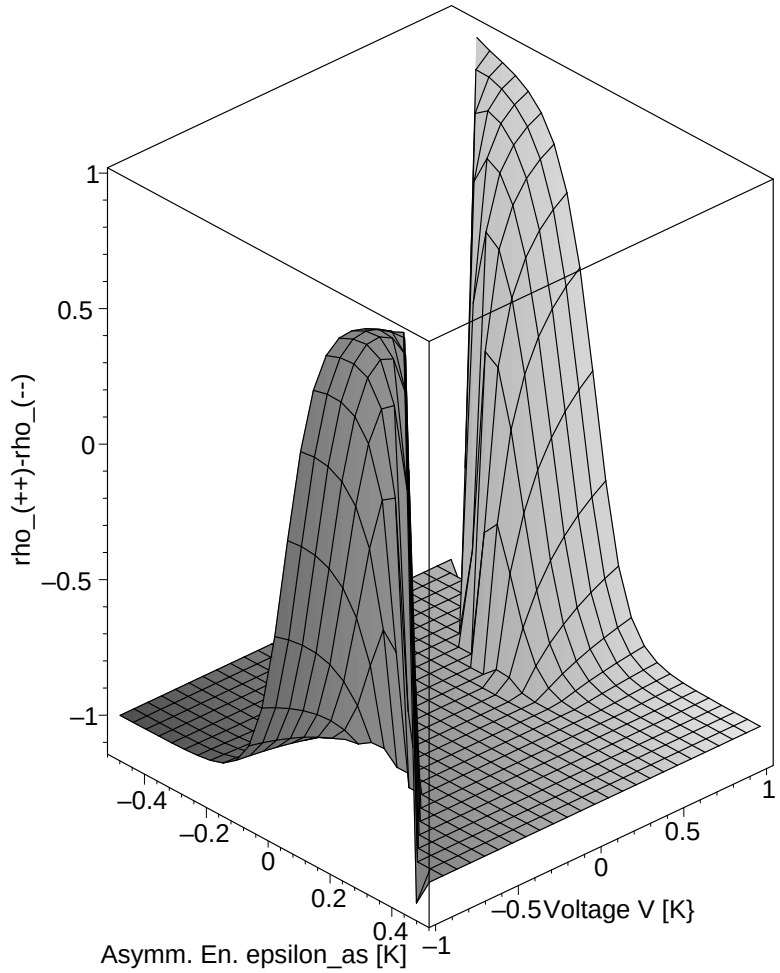

Figure 6.21: Difference of the stationary occupation probabilities $\rho_{++,\mathrm{st}} - \rho_{--,\mathrm{st}}$ for varying ϵ_{as} and V with $\gamma = 0.2$ K, $\epsilon_\beta = 11$ K, $\epsilon_\alpha = 9$ K, $T = 0.1$ mK and $\mu_{\mathrm{av}} = 0.88$ K

Figure 6.21 shows in addition to Figure 6.20 that a "transition" regime between the stable configurations does not exist for low temperatures. This explains the sharp contures in the voltage dependence plots in Chapter 6 (Figures 6.4, 6.8, 6.13, 6.14, 6.15 and 6.16). The pictures in Figure 6.16 contain cuts through the Figures 6.20 and 6.21 for the configuration $\epsilon_{\mathrm{as}} = 0.1$ K and $\gamma = 0.2$ K.

The dominating relaxation channel would give a current in the opposite direction of the bias voltage V, hence it is suppressed.

Chapter 7

Conclusions

We analyzed decoherence and transport properties of spin-polarized electrons due to cotunneling processes in a lateral double quantum dot structure. We showed how one can control decoherence using a non-equilibrium between two baths and we discussed non-linear cotunneling through an artificial molecule.

As a starting point, we used in Chapter 3 a generalized Schrieffer-Wolff transformation [28] to treat the cotunneling processes in order to get an effective description of the interaction between the dots and the leads in the two-state system. This is important, because a standard treatment would only describe sequential tunneling, which is suppressed in the Coulomb Blockade regime and therefore not the dominating transport mechanism.

The resulting Hamiltonian is of typical system and bath form. In Chapter 4 we hence can apply the Bloch-Redfield formalism [22, 31, 34], which treats the system part exactly and performs perturbation theory in the coupling to the bath, which was assumed to be small. As a result one obtains expressions for the time-dependent reduced density matrix ρ and also for the relaxation (τ_r) and dephasing (τ_ϕ) times. Relaxation describes the transition from a starting state to the stationary state, in which mainly the ground state is occupied (see Figure 6.17). Dephasing is the loss of phase information of the off-diagonal elements of the reduced density matrix with growing time. The off-diagonal elements of the reduced density matrix become zeroes in the stationary state. These expressions have been implemented with Maple V (Release 7) for an arbitrary inter-dot coupling γ. The case $\gamma = 0$ has been treated by hand as a Gedanken experiment.

In Chapter 5, an expression for the cotunneling current through this double dot system has been derived and also implemented using Maple V.

The results of this theory are shown and discussed in Chapter 6. The behaviour of the different analyzed quantities can mostly be understood by stability arguments of states due to the internal energy asymmetry and the bias voltage (see Section 6.7). For different signs of the bias voltage $V = \mu_R - \mu_L$ and the asymmetry energy $\epsilon_{\text{as}} = (\epsilon_l - \epsilon_r)/2$, a particular state is in principle more stable than others, whereas there is a maximum for this stability. This can e.g. be observed in the figures concerning the relaxation time.

The dependencies of the relaxation time τ_r on the inter-dot coupling γ, the asymmetry energy ϵ_{as}, the temperature T and the bias voltage V that has been applied between

the leads, are illustrated in several examples in Section 6.1. The transition from the "atomic" to the "molecular" basis, together with asymmetry arguments, dominates the dependence of τ_r on γ (Figure 6.1) in this temperature regime. If one also takes Figure 6.2 into account, one can understand the behaviour as a cross-over between a symmetric and an asymmetric regime. The temperature dependence (Figure 6.3) can be understood by looking at asymmetries and in analogy to the Spin-Boson case [39, 40]. To explain the bias voltage dependence of relaxation time (Figure 6.4), one should again take the asymmetry energy ϵ_{as} and the inter-dot coupling γ into account. Some characteristic points ($\pm 2\delta$) can also be found in figures for the bias voltage dependence of other quantities.
In Section 6.2, we analyzed the dephasing time τ_ϕ. Some properties, that also occurred for relaxation time, can be found here, too. The important difference is the appearance of "flipless" processes, during which there is no energy exchange with the leads. These processes can be suppressed, if one tunes the charging energies ϵ_β and ϵ_α (i.e. the charging energies required for transitions between the two-state system and a higher or lower level) to be equal. If $\epsilon_\beta = \epsilon_\alpha$, then dephasing processes can only take place using relaxation processes. However, we used $\epsilon_\beta \neq \epsilon_\alpha$, because, the charging energies for different levels in a double-dot structure are not equal in general. The "flipless" processes affect the behaviour of the dephasing times in comparison to the relaxation times immensely. One can still observe a decrease of the dephasing time for huge absolute values of γ in Figure 6.5, but an additional stability due to the transition of the basis states cannot be observed. Together with Figure 6.6, again a cross-over can be observed as mentioned above. The temperature dependence of the dephasing time (Figure 6.7) is also very strongly affected by the "flipless" processes, because these are linear in T in the dephasing rate Γ_ϕ [see equation (4.38)]. The dependence of τ_ϕ on the bias voltages V (Figure 6.8) is similar to the behaviour of τ_r, but there is one additional peak at $V = 0$. This is also due to the "flipless" processes.

In the last paragraphs, we described the control of decoherence due to cotunneling processes by applying a voltage (and thus creating a non-equilibrium situation) between the two fermionic baths (leads). There seem to be two different operating points for a quantum calculation and quantum measurement. A long dephasing time τ_ϕ would be good for calculations, that means e.g. $V = 0$ is an appropriate voltage. On the other hand, it would be favourable for a measurement to have a long relaxation time τ_r, which would be realized at $V = \pm 2\delta$ (depending on the sign of the asymmetry energy).

In Section 6.3, we next analyzed the stationary current I_{st}. In the plot for the γ dependence (Figure 6.9) one observes that all stationary currents vanish for $\gamma = 0$. Unfortunately, this could not be resolved for all curves. Another feature was a non-monotonic behaviour of the stationary current with rising inter-dot coupling γ. This has been explained by analyzing the role of different transport channels. An analysis of the ϵ_{as} dependence (Figure 6.10) gives the same result. This is summarized in Figure 6.11, where the borders of the transport regimes are illustrated. Contemplating the temperature dependence of I_{st} (Figure 6.12), one observes two saturation effects: one for small temperatures (see above) and one for higher temperatures. With the thermal excitation, the second molecular state can be addressed for charge transport here. We can also find asymmetries in the bias voltage behaviour of the stationary current (at the same points $\pm 2\delta$ as before) in Figure 6.13.

This could be explained via the same arguments that hold for the relaxation time.

As a next step, we considered in Section 6.4 the bias voltage dependence of quantities that are related to the stationary current and of the difference of the stationary occupation probabilities of ground and excited state ($\rho_{--,\mathrm{st}}$ and $\rho_{++,\mathrm{st}}$ resp.). In these three Figures 6.14, 6.15 and 6.16, one also observes peaks or characteristic points at the same places that have been mentioned above. The reason for this behaviour can again be found in stability arguments due to the interplay of the dot asymmetry energy ϵ_{as} and the bias voltage V (see Section 6.7).

A visualization of the time-dependent elements of the reduced density matrix followed (Figure 6.17) in Section 6.5. One could again see the interplay of ϵ_{as} and V. And additionally the inter-dot coupling γ and the temperature T play an important role to describe the occupation of the state during the flow of time. If one starts in a superposition of states, one observes the dephasing processes via coherent oscillations.

Section 6.6 treated the time-dependent current I (Figure 6.18), which is flowing through the double-dot system due to cotunneling processes. If one starts in a pure state, the current approaches its stationary value I_{st} continuously. In the case of a superposition as a starting state, one can see oscillations again. For $\gamma = 0$ there is also a continuous progression of the current. This makes sense, because charge transport without an inter-dot coupling is only possible via the leads.

Finally, some stability arguments were discussed in the last section (Section 6.7).

To summarize this thesis, we described the control of dephasing (for quantum operations) and relaxation (for detection) of a coupled double-dot system due to cotunneling processes to leads. This control is possible by adjusting various parameters, in particular also the transport voltage.

We interpret our results for the charge transport $I_{\mathrm{st}}(\gamma)$ (with a rich, non-monotonic structure) in terms of coherent channels. This can be called "molecular cotunneling spectroscopy".

The relaxation rate Γ_r and the current I depend on each other, which we explained via stability arguments (see Section 6.7).

The experimentally measured decoherence times are, however, in the order of μs [27], whereas our observations can only explain relaxation and dephasing times in the range of $10 - 1000$ ms. Consequently, we did not focus on the dominating decoherence process in this thesis. We have to permit other effects like phonon and/or photon assisted processes [46, 47, 43, 27] in order to do this. If it is possible to suppress the decoherence due to phonons using phonon cavities [47], then cotunneling could again be the dominating decoherence mechanism. An analysis of the used electrical circuit could maybe also be useful in order to reduce further, unwanted sources of decoherence.

The application of a similar theory to explain recent experimental results [44] would be another prospective field of work.

Chapter 8

Deutsche Zusammenfassung

In den vorausgegangenen Kapiteln haben wir Dekohärenz- und Transporteigenschaften von spin-polarisierten Elektronen in einer lateralen Doppelquantenpunktstruktur im Kotunnelregime analysiert. Wir haben gezeigt, wie man Dekohärenz mithilfe eines Nichtgleichgewichts zwischen den beiden Bädern kontrollieren kann. Und wir haben nichtlineares Kotunneln durch ein künstliches Molekül diskutiert.

Zunächst verwenden wir in Kapitel 3 zur Behandlung der Kotunnelprozesse eine verallgemeinerte Schrieffer-Wolff-Transformation [28], um eine effektive Beschreibung der Wechselwirkung zwischen Quantenpunkten und Kontakten in Form eines Hamiltonianoperators zu erhalten. Das ist sehr wichtig, denn eine Standardbehandlung würde nur sequentielles Tunneln, das im Coulomb-Blockade-Regime unterdrückt und deswegen nicht der dominierende Dekohärenzmechanismus ist, beschreiben.

In Kapitel 4 sind wir in der Lage den Bloch-Redfield-Formalismus [22, 31, 34], der interne Kopplungen voll und Kopplungen an äußere Bäder perturbativ berücksichtigt, anzuwenden. Als Ergebnis erhält man Ausdrücke für die zeitabhängige reduzierte Dichtematrix ρ und auch für die Relaxationszeit τ_r und die Dephasierungszeit τ_ϕ. Relaxation beschreibt den Übergang eines Anfangszustandes in den stationären Zustand, wobei man nachher hauptsächlich den Grundzustand besetzt sieht (siehe Abbildung 6.17). Dephasierung ist der Verlust der Phaseninformationen der nicht-diagonalen reduzierten Dichtematrixelemente mit fortschreitender Zeit. Im stationären Zustand werden die nicht-diagonalen reduzierten Dichtematrixelemente zu Nullen. Für beliebige Kopplung γ zwischen den beiden Quantenpunkten sind diese Ausdrücke in Maple V (Release 7) implementiert worden und den Fall $\gamma = 0$ haben wir als Gedankenexperiment von Hand berechnet.

Im anschließenden Kapitel 5 wird ein Ausdruck für den Kotunnel-Strom durch dieses Doppelquantenpunktsystem hergeleitet und darauffolgend ebenfalls in Maple V implementiert.

Eine Sammlung von graphischen Ergebnissen und physikalischen Erklärungen folgt (Kapitel 6). Die meisten Verhaltensweisen der verschiedenen analysierten Größen lassen sich durch Überlegungen zur Stabilität von Zuständen aufgrund von Symmetrieargumenten und Spannungseinstellungen erklären (siehe auch Abschnitt 6.7). Bei verschiedenen Vorzeichen von Spannung $V = \mu_R - \mu_L$ und Asymmetrieenergie $\epsilon_{\text{as}} = (\epsilon_l - \epsilon_r)/2$ ist der

Zustand prinzipiell stabiler, wobei es auch ein Maximum der Stabilität gibt. Dies kann man insbesondere in den Abbildungen zur Relaxationszeit beobachten.

Die Abhängigkeit der Relaxationszeit τ_r von der Kopplungsstärke γ zwischen den Quantenpunkten, von der Asymmetrieenergie ϵ_{as}, von der Temperatur T und der an die Kontakte angelegten Spannung V wird anhand von Beispielen in Abschnitt 6.1 gezeigt. Der Basiswechsel vom "atomaren" zum "molekularen" Zweizustandssystem dominiert in diesem Temperaturbereich zusammen mit Asymmetrieüberlegungen das Verhalten von τ_r bei Variation von γ (Abbildung 6.1). Wenn man zusätzlich noch Abbildung 6.2 betrachtet, dann kann man das Verhalten als "cross-over" zwischen einem symmetrischen und einem asymmetrischen Regime verstehen. Die Temperaturabhängigkeit (Abbildung 6.3) kann aufgrund von Asymmetrien und der Analogie zum Spin-Boson Fall [39, 40] verstanden werden. Für eine Erklärung der Spannungsabhängigkeit (Abbildung 6.4) kann man wieder die Asymmetrieenergie ϵ_{as} und die Kopplungsstärke γ heranziehen. Bestimmte charakteristische Punkte ($\pm 2\delta$) findet man auch in den Abbildungen der Spannungsabhängigkeiten der anderen Größen.

In Abschnitt 6.2 wird die Dephasierungszeit τ_ϕ betrachtet. Hier lassen sich einige Eigenschaften, die auch bei der Relaxationszeit auftraten, wiederfinden. Der wesentliche Unterschied ist das Auftreten von "fliplosen" Prozessen, bei denen kein Energieaustausch mit den Kontakten erfolgt. Diese Prozesse lassen sich auch ausschließen, wenn man die Ladungsenergien ϵ_β und ϵ_α, die zu Übergängen zum nächsthöheren bzw. -niedrigen Energieniveau der Quantenpunkte außerhalb des Zweizustandssystems benötigt werden, gleichsetzt. Dann findet Dephasierung nur noch über Relaxationsprozesse statt. Wir behalten diese Asymmtrie in den Ladungsenergien allerdings in allen Abbildungen in Kapitel 6 bei, um keine charakteristischen Eigenschaften unseres Systems zu verpassen. Abgesehen davon sind die Ladungsenergien im allgemeinen nicht gleich. Die "fliplosen" Prozesse verändern die Eigenschaften der Dephasingzeit im Vergleich zur Relaxationszeit ganz erheblich. Zwar beobachtet man immer noch ein Abfallen der Dephasingzeit für große Kopplungsstärken γ (Abbildung 6.5), allerdings scheint das Vorhandensein der molekularen Basis bei endlichen γ's keine anfängliche, zusätzliche Stabilität geben. Zusammen mit Abbildung 6.6 kann man wieder ein "cross-over" beobachten (s.o.). Die Temperaturabhängigheit der Dephasierungszeit (Abbildung 6.7) ist ebenfalls durch die "fliplosen" Prozesse stark beeinflußt, denn diese sind linear in der Temperatur in der Dephasingrate Γ_ϕ [siehe auch (4.38)]. Die Abhängigkeit von der angelegten Spannung (Abbildung 6.8) ist ähnlich wie die der Relaxationszeit, jedoch gibt es noch einen Peak bei $V = 0$, der durch die "fliplosen" Prozesse entstanden ist.

In den letzten Absätzen haben wir die Kontrolle der Dekohärenz aufgrund von Kotunnel-Prozessen durch Anlegen einer Spannung (und damit der Erzeugung eines Nichtgleichgewichts) zwischen den beiden fermionischen Bädern (Kontakten) beschrieben. Es scheint zwei verschiedene Arbeitspunkte für das Rechnen mit den Doppelquantenpunkten und deren Auslesen zu geben. Eine lange Dephasierungszeit τ_ϕ ist gut für Rechnungen, d.h. $V = 0$ ist eine angemessene Spannung. Andererseits ist es für eine Messung der Quantenzustände nützlich, eine lange Relaxationszeit τ_r zu haben, was bei $V = \pm 2\delta$ (abhängig vom Vorzeichen der Asymmetrieenergie) realisiert ist.

In Abschnitt 6.3 wird der stationäre Strom I_{st} analysiert. In der γ-Abhängigkeit (Abbildung 6.9) erkennt man, daß für $\gamma = 0$ alle stationären Ströme verschwinden, auch wenn das nicht für alle Parameter in den entsprechenden Abbildungen aufgelöst werden kann. Ansonsten bemerkt man ein nicht-monotones Verhalten des stationären Stroms mit steigender Kopplung γ zwischen den Quantenpunkten. Dies erklärt man durch verschiedene Transportregime. Eine Analyse der ϵ_{as}-Abhängigkeit (Abbildung 6.10) ergibt das gleiche Ergebnis, welches dann noch einmal in Form der Abbildung 6.11 mit den Grenzen der Transportregime illustriert wird. In der Temperaturabhängigkeit (Abbildung 6.12) von I_{st} findet man zwei Sättigungseffekte: einen für kleine Temperaturen (vorher beobachtet) und einen für höhere Temperaturen. Hier wird durch thermische Anregung der zweite molekulare Zustand für den Transport zugänglich gemacht. Und wieder kann man Asymmetrien in der Spannungsabhängigkeit (Abbildung 6.13) ausmachen (an den gleichen Stellen $\pm 2\delta$ wie vorher). Dies wird erklärbar über ähnliche Argumente wie bei der Relaxationszeit.

Als nächster Schritt (Abschnitt 6.4) wird die Spannungsabhängigkeit der Größen untersucht, die aus dem stationären Strom gewonnen wurden, sowie die Differenz der stationären Besetzungszahlen von anregtem und Grundzustand ($\rho_{++,\mathrm{st}}$ und $\rho_{--,\mathrm{st}}$) als Funktion der Spannung V. In diesen drei Abbildungen (6.14, 6.15 und 6.16) ergeben sich ebenfalls Sprünge oder vielmehr charakteristische Punkte an den gleichen Stellen, wie bereits zuvor notiert. Die Begründung ist wiederum in Stabilitätsargumenten aufgrund der Wechselwirkung zwischen Asymmetrieenergie ϵ_{as} und der angelegten Spannung V zu finden (siehe Abschnitt 6.7).

Darauf folgt eine Visualierung des Zeitverhaltens der reduzierten Dichtematrixelemente (Abbildung 6.17) in Abschnitt 6.5. Auch hier kann man wieder das Wechselspiel zwischen ϵ_{as} und V feststellen, außerdem spielen die Kopplung γ zwischen den Quantenpunkten und die Temperatur eine entscheidende Rolle, wie die Zustände im Laufe der Zeit besetzt werden. Für den Fall, daß man in einer Überlagerung von Zuständen startet, kann man die Dephasierung in der Form von kohärenten Oszillationen beobachten.

Abschnitt 6.6 behandelt den zeitabhängigen Strom I, der durch das Doppelquantenpunktsystem aufgrund von Kotunnel-Prozessen fließt (Abbildung 6.18). Wenn man in einem reinem Zustand startet, dann läuft der Strom kontinuierlich auf seinen stationären Wert I_{st} zu. Falls man in einem Überlagerungszustand und $\gamma \neq 0$ beginnt, so kann man wiederum Oszillationen beobachten; für $\gamma = 0$ ist auch ein kontinuierlicher Verlauf zu beobachten. Was auch Sinn macht, denn ohne eine Kopplung zwischen den Dots ist ein Elektronen-Transport nur über die Kontakte möglich.

Im oft zitierten, letzten Abschnitt 6.7 werden einige Stabilitätsargumente im lateralen Doppelquantenpunktsystem diskutiert.

Mit dieser Arbeit sind wir in der Lage, die Kontrolle von Dephasierung (wichtig für die Quantenoperationen) und Relaxation (wichtig für die Messung) in einem gekoppelten Doppelquantenpunktsystem aufgrund der Ankopplung an zwei Kontakte zu beschreiben. Diese Kontrolle kann durch verschiedene Parameter (insbesondere durch das Anlegen einer geeigneten Spannung) ausgeübt werden.

Wir interpretieren unsere Ergebnisse für den Ladungstransport $I_{\mathrm{st}}(\gamma)$ (mit einer vielfältigen, nicht-monotonen Struktur) als kohärente Transportkanäle. Man kann dies auch als

"Molekulare Kotunnelspektroskopie" bezeichnen.

Die Relaxationsrate Γ_r und der Strom I sind abhängig voneinander, was in Abschnitt 6.7 erklärt wird.

Diese Ergebnisse erklären jedoch nicht die wesentlichen Dekohärenzeigenschaften, die man experimentell beobachtet [27], denn hier liegen die gemessenen Relaxations- und Dephasierungszeiten in der Größenordnung von μs. Unsere Beobachtungen können jedoch nur 10-1000 ms erklären. In einem nächsten Schritt liegt es nahe, zusätzlich zum Kotunneln noch andere Effekte zuzulassen und deren Auswirkung zu prüfen. In Frage kämen dafür Phononen und/oder Photonen [46, 47, 43, 27]. Falls es möglich sein sollte, die durch Phononen erzeugte Dekohärenz mithilfe von Phononen-Kavitäten [47] zu unterdrücken, dann könnte der hier betrachtete Kotunnel-Mechanismus wieder der dominierende Dekohärenzkanal sein. Eine Analyse des Einflusses des Stromkreises könnte möglicherweise auch nützlich sein, um andere, ungewollten Dekohärenzquellen zu reduzieren.

Ein anderes, künftiges Arbeitsgebiet könnte die Anwendung einer ähnlichen Theorie sein, um neue experimentelle Ergebnisse [44] zu erklären.

Acknowledgements

At the end of the diploma thesis, I would like to thank a lot of people for making all this possible:

- Prof. Dr. Jan von Delft for giving me the opportunity to join his team in Munich and for interesting discussions;
- Dr. Frank K. Wilhelm for his advice and his support in the last year, it was a great pleasure to work for/with you;
- Prof. Dr. Peter Herzog and Prof. Dr. Hartmut Monien from the University of Bonn for their official support;
- the others at the Chair for Theoretical Condensed Matter Physics (at LMU in Munich): Rong, László, Silvia, Dominique, Corinna, Henryk, Michael, Markus and Stéphane; especially the discussions with László, Michael and Markus have been very helpful for me;
- the group of Dr. Robert H. Blick at the chair of Prof. Dr. Jörg Kotthaus at LMU in Munich (experimental semiconductor physics): Dr. Alexander W. Holleitner, Eva M. Höhberger and Andreas K. Hüttel for their experimental view of the work;
- Dr. Jürgen König, Dr. Ulrich Zülicke, Dr. Achim Rosch (all TU Karlsruhe) and Dr. Igor Goychuk (University of Augsburg) for fruitful and helpful discussions;
- my family: my parents Beate and Johannes Hartmann, and my sister Regina for their support during the last years;
- Markus Storcz for his endless patience with me (sharing office *and* home is not always so easy);
- my friends Teresa and Chrissie, Gregor, Ralf, Florian (Uni Bonn), Markus, Martin, Friedhelm and all the others for not forgetting me in Bavaria;
- the Center for NanoScience (CeNS) for the organizational help and the posters;
- the Army Research Office (ARO) for financial support (Contract-Nr. P-43385-PH-QC: *Realistic theory of solid-state qubits*).

Appendix A

Schrieffer-Wolff coefficients

By applying equation (3.1), one can find all Schrieffer-Wolff coefficients, which are used in (3.2)-(3.5).

The Schrieffer-Wolff coefficients for $H_{I,++}$ are

$$A(R\dagger,R,++) = \frac{t_c^2}{2S^2}\left[\frac{1}{\epsilon_m^R-(-\delta+\epsilon_\beta)}+\frac{-1}{\epsilon_n^R-(\delta-\epsilon_\beta)}\right] \tag{A.1}$$

$$A(R\dagger,L,++) = \frac{t_c^2}{2S^2}\left[\frac{1}{\epsilon_m^R-(-\delta+\epsilon_\beta)}+\frac{-1}{\epsilon_l^L-(\delta-\epsilon_\beta)}\right]\frac{\gamma}{\delta+\epsilon_{\rm as}} \tag{A.2}$$

$$A(L\dagger,R,++) = \frac{t_c^2}{2S^2}\left[\frac{1}{\epsilon_k^L-(-\delta+\epsilon_\beta)}+\frac{-1}{\epsilon_n^R-(\delta-\epsilon_\beta)}\right]\frac{\gamma}{\delta+\epsilon_{\rm as}} \tag{A.3}$$

$$A(L\dagger,L,++) = \frac{t_c^2}{2S^2}\left[\frac{1}{\epsilon_k^L-(-\delta+\epsilon_\beta)}+\frac{-1}{\epsilon_l^L-(\delta-\epsilon_\beta)}\right]\times \times\frac{\gamma^2}{(\delta+\epsilon_{\rm as})^2} \tag{A.4}$$

$$A(L,L\dagger,++) = \frac{t_c^2}{2S^2}\left[\frac{-1}{\epsilon_l^L-(\delta+\epsilon_\alpha)}+\frac{1}{\epsilon_k^L-(-\delta-\epsilon_\alpha)}\right] \tag{A.5}$$

$$A(L,R\dagger,++) = \frac{t_c^2}{2S^2}\left[\frac{-1}{\epsilon_l^L-(\delta+\epsilon_\alpha)}+\frac{1}{\epsilon_m^R-(-\delta-\epsilon_\alpha)}\right]\frac{\gamma}{\delta+\epsilon_{\rm as}} \tag{A.6}$$

$$A(R,L\dagger,++) = \frac{t_c^2}{2S^2}\left[\frac{-1}{\epsilon_n^R-(\delta+\epsilon_\alpha)}+\frac{1}{\epsilon_k^L-(-\delta-\epsilon_\alpha)}\right]\frac{\gamma}{\delta+\epsilon_{\rm as}} \tag{A.7}$$

$$A(R,R\dagger,++) = \frac{t_c^2}{2S^2}\left[\frac{-1}{\epsilon_n^R-(\delta+\epsilon_\alpha)}+\frac{1}{\epsilon_m^R-(-\delta-\epsilon_\alpha)}\right]\times \times\frac{\gamma^2}{(\delta+\epsilon_{\rm as})^2}\ . \tag{A.8}$$

The Schrieffer-Wolff coefficients for $H_{I,--}$ are

$$A(R\dagger,R,--) = \frac{t_c^2}{2S^2}\left[\frac{1}{\epsilon_m^R-(\delta+\epsilon_\beta)}+\frac{-1}{\epsilon_n^R-(-\delta-\epsilon_\beta)}\right]\times \times\frac{\gamma^2}{(\delta+\epsilon_{\rm as})^2} \tag{A.9}$$

$$A(R\dagger,L,--) = \frac{t_c^2}{2S^2}\left[\frac{1}{\epsilon_m^R-(\delta+\epsilon_\beta)}+\frac{-1}{\epsilon_l^L-(-\delta-\epsilon_\beta)}\right]\times \times\frac{-\gamma}{\delta+\epsilon_{\rm as}} \tag{A.10}$$

$$A(L\dagger,R,--) = \frac{t_c^2}{2S^2}\left[\frac{1}{\epsilon_k^L-(\delta+\epsilon_\beta)}+\frac{-1}{\epsilon_n^R-(-\delta-\epsilon_\beta)}\right]\times \times\frac{-\gamma}{\delta+\epsilon_{\rm as}} \tag{A.11}$$

$$A(L\dagger,L,--) = \frac{t_c^2}{2S^2}\left[\frac{1}{\epsilon_k^L-(\delta+\epsilon_\beta)}+\frac{-1}{\epsilon_l^L-(-\delta-\epsilon_\beta)}\right] \tag{A.12}$$

$$A(L,L\dagger,--) = \frac{t_c^2}{2S^2}\left[\frac{-1}{\epsilon_l^L-(-\delta+\epsilon_\alpha)}+\frac{1}{\epsilon_k^L-(\delta-\epsilon_\alpha)}\right]\times \times\frac{\gamma^2}{(\delta+\epsilon_{\rm as})^2} \tag{A.13}$$

$$A(L,R\dagger,--) = \frac{t_c^2}{2S^2}\left[\frac{-1}{\epsilon_l^L-(-\delta+\epsilon_\alpha)}+\frac{1}{\epsilon_m^R-(\delta-\epsilon_\alpha)}\right]\times \times\frac{-\gamma}{\delta+\epsilon_{\rm as}} \tag{A.14}$$

$$A(R,L\dagger,--) = \frac{t_c^2}{2S^2}\left[\frac{-1}{\epsilon_n^R-(-\delta+\epsilon_\alpha)}+\frac{1}{\epsilon_k^L-(\delta-\epsilon_\alpha)}\right]\times \times\frac{-\gamma}{\delta+\epsilon_{\rm as}} \tag{A.15}$$

$$A(R,R\dagger,--) = \frac{t_c^2}{2S^2}\left[\frac{-1}{\epsilon_n^R-(-\delta+\epsilon_\alpha)}+\frac{1}{\epsilon_m^R-(\delta-\epsilon_\alpha)}\right]. \tag{A.16}$$

The Schrieffer-Wolff coefficients for $H_{I,+-}$ are

$$A(R\dagger,R,+-) = \frac{t_c^2}{2S^2}\left[\frac{1}{\epsilon_m^R-(-\delta+\epsilon_\beta)}+\frac{-1}{\epsilon_n^R-(-\delta-\epsilon_\beta)}\right]\times \times\frac{-\gamma}{\delta+\epsilon_{\rm as}} \tag{A.17}$$

$$A(R\dagger,L,+-) = \frac{t_c^2}{2S^2}\left[\frac{1}{\epsilon_m^R-(-\delta+\epsilon_\beta)}+\frac{-1}{\epsilon_l^L-(-\delta-\epsilon_\beta)}\right] \tag{A.18}$$

$$A(L\dagger,R,+-) = \frac{t_c^2}{2S^2}\left[\frac{1}{\epsilon_k^L-(-\delta+\epsilon_\beta)}+\frac{-1}{\epsilon_n^R-(-\delta-\epsilon_\beta)}\right]\times \times\frac{-\gamma^2}{(\delta+\epsilon_{\rm as})^2} \tag{A.19}$$

$$A(L\dagger,L,+-) = \frac{t_c^2}{2S^2}\left[\frac{1}{\epsilon_k^L-(-\delta+\epsilon_\beta)}+\frac{-1}{\epsilon_l^L-(-\delta-\epsilon_\beta)}\right]\times \times\frac{\gamma}{\delta+\epsilon_{\rm as}} \tag{A.20}$$

$$A(L,L\dagger,+-) = \frac{t_c^2}{2S^2}\left[\frac{-1}{\epsilon_l^L-(\delta+\epsilon_\alpha)}+\frac{1}{\epsilon_k^L-(\delta-\epsilon_\alpha)}\right]\times \times\frac{-\gamma}{\delta+\epsilon_{\rm as}} \tag{A.21}$$

$$A(L,R\dagger,+-) = \frac{t_c^2}{2S^2}\left[\frac{-1}{\epsilon_l^L-(\delta+\epsilon_\alpha)}+\frac{1}{\epsilon_m^R-(\delta-\epsilon_\alpha)}\right] \tag{A.22}$$

$$A(R,L\dagger,+-) = \frac{t_c^2}{2S^2}\left[\frac{-1}{\epsilon_n^R-(\delta+\epsilon_\alpha)}+\frac{1}{\epsilon_k^L-(\delta-\epsilon_\alpha)}\right]\times \times\frac{-\gamma^2}{(\delta+\epsilon_{\rm as})^2} \tag{A.23}$$

$$A(R,R\dagger,+-) = \frac{t_c^2}{2S^2}\left[\frac{-1}{\epsilon_n^R-(\delta+\epsilon_\alpha)}+\frac{1}{\epsilon_m^R-(\delta-\epsilon_\alpha)}\right]\times \times\frac{\gamma}{\delta+\epsilon_{\rm as}}\ . \tag{A.24}$$

The Schrieffer-Wolff coefficients for $H_{I,-+}$ are

$$A(R\dagger,R,-+) = \frac{t_c^2}{2S^2}\left[\frac{1}{\epsilon_m^R-(\delta+\epsilon_\beta)}+\frac{-1}{\epsilon_n^R-(\delta-\epsilon_\beta)}\right]\times \times\frac{-\gamma}{\delta+\epsilon_{\rm as}} \tag{A.25}$$

$$A(R\dagger,L,-+) = \frac{t_c^2}{2S^2}\left[\frac{1}{\epsilon_m^R-(\delta+\epsilon_\beta)}+\frac{-1}{\epsilon_l^L-(\delta-\epsilon_\beta)}\right]\times \times\frac{-\gamma^2}{(\delta+\epsilon_{\rm as})^2} \tag{A.26}$$

$$A(L\dagger,R,-+) = \frac{t_c^2}{2S^2}\left[\frac{1}{\epsilon_k^L-(\delta+\epsilon_\beta)}+\frac{-1}{\epsilon_n^R-(\delta-\epsilon_\beta)}\right] \tag{A.27}$$

$$A(L\dagger,L,-+) = \frac{t_c^2}{2S^2}\left[\frac{1}{\epsilon_k^L-(\delta+\epsilon_\beta)}+\frac{-1}{\epsilon_l^L-(\delta-\epsilon_\beta)}\right]\times \times\frac{\gamma}{\delta+\epsilon_{\rm as}} \tag{A.28}$$

$$A(L,L\dagger,-+) = \frac{t_c^2}{2S^2}\left[\frac{-1}{\epsilon_l^L-(-\delta+\epsilon_\alpha)}+\frac{1}{\epsilon_k^L-(-\delta-\epsilon_\alpha)}\right]\times \times\frac{-\gamma}{\delta+\epsilon_{\rm as}} \tag{A.29}$$

$$A(L,R\dagger,-+) = \frac{t_c^2}{2S^2}\left[\frac{-1}{\epsilon_l^L-(-\delta+\epsilon_\alpha)}+\frac{1}{\epsilon_m^R-(-\delta-\epsilon_\alpha)}\right]\times \times\frac{-\gamma^2}{(\delta+\epsilon_{\rm as})^2} \tag{A.30}$$

$$A(R,L\dagger,-+) = \frac{t_c^2}{2S^2}\left[\frac{-1}{\epsilon_n^R-(-\delta+\epsilon_\alpha)}+\frac{1}{\epsilon_k^L-(-\delta-\epsilon_\alpha)}\right] \tag{A.31}$$

$$A(R,R\dagger,-+) = \frac{t_c^2}{2S^2}\left[\frac{-1}{\epsilon_n^R-(-\delta+\epsilon_\alpha)}+\frac{1}{\epsilon_m^R-(-\delta-\epsilon_\alpha)}\right]\times \times\frac{\gamma}{\delta+\epsilon_{\rm as}}\ . \tag{A.32}$$

Appendix B

Effect of the renormalization

Our renormalization has been formulated by

$$\tilde{H}_I(t) := \tilde{H}_I(t) - \langle \tilde{H}_I(t) \rangle \ . \tag{B.1}$$

Let us now consider the effect of this renormalization on $H_{0,\mathrm{diag}}$. As already seen in equation (4.10), we defined $\langle \tilde{H}_I \rangle$ in each component as

$$\begin{aligned} \langle \tilde{H}_I \rangle &= A(R\dagger, R) f_R(\epsilon_m^R)\delta_{mn} + A(L\dagger, L) f_L(\epsilon_k^L)\delta_{kl} \\ &\quad + A(L, L\dagger)(1 - f_L(\epsilon_k^L))\delta_{kl} \\ &\quad + A(R, R\dagger)(1 - f_R(\epsilon_m^R))\delta_{mn} \ . \end{aligned} \tag{B.2}$$

Going to the continuum limit, one finds

$$\begin{aligned} \langle \tilde{H}_I \rangle &= c_2 \int_{-\infty}^{\infty} d\epsilon_m^R A(R\dagger, R) f_R(\epsilon_m^R) + c_2 \int_{-\infty}^{\infty} d\epsilon_k^L A(L\dagger, L) f_L(\epsilon_k^L) \\ &\quad + c_2 \int_{-\infty}^{\infty} d\epsilon_k^L A(L, L\dagger)(1 - f_L(\epsilon_k^L)) \\ &\quad + c_2 \int_{-\infty}^{\infty} d\epsilon_m^R A(R, R\dagger)(1 - f_R(\epsilon_m^R)) \ , \end{aligned} \tag{B.3}$$

with c_2 again being a factor which comes out of the density of states in the leads, $c_2 = \frac{V_{\mathrm{2DEG}} m_*}{2\pi\hbar^2}$. The first two integrals have both the form

$$c_3 \int_{-\infty}^{\infty} d\epsilon \frac{1}{\epsilon - \zeta} \frac{1}{e^{\beta(\epsilon-\mu)} + 1} \ , \tag{B.4}$$

and the other two integrals in (B.3) have the generic structure

$$c_3 \int_{-\infty}^{\infty} d\epsilon \frac{1}{\epsilon - \zeta} \frac{1}{e^{-\beta(\epsilon-\mu)} + 1} \ , \tag{B.5}$$

where c_3 is a product of c_2 with the constants from the Schrieffer-Wolff coefficients. The integrals (B.4) and (B.5) can be calculated using the residue theorem along the lines of [36]. The application of the residue theorem gives then

$$\begin{aligned}\int_{-\infty}^{\infty} d\epsilon \frac{1}{\epsilon-\zeta}\frac{1}{e^{\beta(\epsilon-\mu)}+1} &= \pi i f(\zeta) \\ &\quad -\frac{2\pi i}{\beta}\sum_{j=0}^{\infty}\frac{1}{\mu-\zeta+\frac{\pi i}{\beta}(2j+1)} \qquad \text{(B.6)}\\ \int_{-\infty}^{\infty} d\epsilon \frac{1}{\epsilon-\zeta}\frac{1}{e^{-\beta(\epsilon-\mu)}+1} &= \pi i(1-f(\zeta)) \\ &\quad +\frac{2\pi i}{\beta}\sum_{j=0}^{\infty}\frac{1}{\mu-\zeta+\frac{\pi i}{\beta}(2j+1)}\ . \qquad \text{(B.7)}\end{aligned}$$

This is the way how all these integrals can be evaluated. The final results for this procedure are given below. To get a feeling for the influence of the renormalization, we consider only the order of magnitude, which is given by c_3. We take c_3 now as

$$c_3 = \frac{t_c^2}{2S^2}\frac{V_{\text{2DEG}} m_*}{2\pi\hbar^2}\ , \qquad \text{(B.8)}$$

whereas other occuring factors will not change the order of magnitude.

We take the following values for the parameters: $\hbar = 7.605 \cdot 10^{-12}$ Ks, $m_* = m_e = 9.109 \cdot 10^{-31}$ kg, $V_{\text{2DEG}} = 10^{-12}$ m^2, $t_c = 1.21$ mK and $S = 1$.
Whereas the numerical values for t_c and S are realistic estimates, the choice of t_c is discussed in Chapter 6 and S only consists of factors that will not change the order of magnitude as we stated before. The final result for the order of magnitude of c_3 is then

$$c_3 = 1.3277 \cdot 10^{-4}\text{K}\ . \qquad \text{(B.9)}$$

This a 1000 times smaller than typical values of the asymmetry energy ϵ_{as} or the inter-dot coupling γ. Thus we normally neglect the effect of the renormalization.

One needs the follwing rule (similar to [37]) to get Digamma or ψ functions in equations (B.6) and (B.7)

$$\begin{aligned}\psi(x+iy)-\psi(x+iz) &= \sum_{j=0}^{\infty}\left(\frac{1}{x+iz+j}-\frac{1}{x+iy+j}\right) \\ &= \sum_{j=0}^{\infty}\frac{i(y-z)}{(x+iz+j)(x+iy+j)}\ . \qquad \text{(B.10)}\end{aligned}$$

Then one yields the effect of the renormalization as

$$
\begin{aligned}
\langle \tilde{H}_I \rangle_{++} &= c_3 \Bigg\{ \pi i [f_R(-\delta+\epsilon_\beta) - f_R(\delta-\epsilon_\beta)] \\
&\quad -\psi\left(\frac{1}{2}+\frac{i\beta}{2\pi}(\delta-\epsilon_\beta-\mu_R)\right)+\psi\left(\frac{1}{2}+\frac{i\beta}{2\pi}(-\delta+\epsilon_\beta-\mu_R)\right) \\
&\quad +\frac{\gamma^2}{(\delta+\epsilon_{\rm as})^2}\Bigg[\pi i[f_l(-\delta+\epsilon_\beta)-f_L(\delta-\epsilon_\beta)] \\
&\quad -\psi\left(\frac{1}{2}+\frac{i\beta}{2\pi}(\delta-\epsilon_\beta-\mu_L)\right)+\psi\left(\frac{1}{2}+\frac{i\beta}{2\pi}(-\delta+\epsilon_\beta-\mu_L)\right)\Bigg] \\
&\quad +\pi i[(1-f_L(-\delta-\epsilon_\alpha))-(1-f_L(\delta+\epsilon_\alpha))] \\
&\quad +\psi\left(\frac{1}{2}+\frac{i\beta}{2\pi}(\delta+\epsilon_\alpha-\mu_L)\right)-\psi\left(\frac{1}{2}+\frac{i\beta}{2\pi}(-\delta-\epsilon_\alpha-\mu_L)\right) \\
&\quad +\frac{\gamma^2}{(\delta+\epsilon_{\rm as})^2}\Bigg[\pi i[(1-f_R(-\delta-\epsilon_\alpha))-(1-f_R(\delta+\epsilon_\alpha))] \\
&\quad +\psi\left(\frac{1}{2}+\frac{i\beta}{2\pi}(\delta+\epsilon_\alpha-\mu_R)\right)-\psi\left(\frac{1}{2}+\frac{i\beta}{2\pi}(-\delta-\epsilon_\alpha-\mu_R)\right)\Bigg]\Bigg\} \quad \text{(B.11)}
\end{aligned}
$$

$$
\begin{aligned}
\langle \tilde{H}_I \rangle_{--} &= c_3 \Bigg\{ \frac{\gamma^2}{(\delta+\epsilon_{\rm as})^2}\Bigg[\pi i[f_R(\delta+\epsilon_\beta)-f_R(-\delta-\epsilon_\beta)] \\
&\quad -\psi\left(\frac{1}{2}+\frac{i\beta}{2\pi}(-\delta-\epsilon_\beta-\mu_R)\right)+\psi\left(\frac{1}{2}+\frac{i\beta}{2\pi}(\delta+\epsilon_\beta-\mu_R)\right)\Bigg] \\
&\quad +\pi i[f_l(\delta+\epsilon_\beta)-f_L(-\delta-\epsilon_\beta)] \\
&\quad -\psi\left(\frac{1}{2}+\frac{i\beta}{2\pi}(-\delta-\epsilon_\beta-\mu_L)\right)+\psi\left(\frac{1}{2}+\frac{i\beta}{2\pi}(\delta+\epsilon_\beta-\mu_L)\right) \\
&\quad +\frac{\gamma^2}{(\delta+\epsilon_{\rm as})^2}\Bigg[\pi i[(1-f_L(\delta-\epsilon_\alpha))-(1-f_L(-\delta+\epsilon_\alpha))] \\
&\quad +\psi\left(\frac{1}{2}+\frac{i\beta}{2\pi}(-\delta+\epsilon_\alpha-\mu_L)\right)-\psi\left(\frac{1}{2}+\frac{i\beta}{2\pi}(\delta-\epsilon_\alpha-\mu_L)\right)\Bigg] \\
&\quad +\pi i[(1-f_R(\delta-\epsilon_\alpha))-(1-f_R(-\delta+\epsilon_\alpha))] \\
&\quad +\psi\left(\frac{1}{2}+\frac{i\beta}{2\pi}(-\delta+\epsilon_\alpha-\mu_R)\right)-\psi\left(\frac{1}{2}+\frac{i\beta}{2\pi}(\delta-\epsilon_\alpha-\mu_R)\right)\Bigg\} \quad \text{(B.12)}
\end{aligned}
$$

$$
\begin{aligned}
\langle \tilde{H}_I \rangle_{+-} &= c_3 \Bigg\{ \frac{-\gamma}{\delta + \epsilon_{\rm as}} \Bigg[\pi i [f_R(-\delta + \epsilon_\beta) - f_R(-\delta - \epsilon_\beta)] \\
&\quad - \psi \left(\frac{1}{2} + \frac{i\beta}{2\pi} (-\delta - \epsilon_\beta - \mu_R) \right) + \psi \left(\frac{1}{2} + \frac{i\beta}{2\pi} (-\delta + \epsilon_\beta - \mu_R) \right) \Bigg] \\
&\quad + \frac{\gamma}{\delta + \epsilon_{\rm as}} \Bigg[\pi i [f_l(-\delta + \epsilon_\beta) - f_L(-\delta - \epsilon_\beta)] \\
&\quad - \psi \left(\frac{1}{2} + \frac{i\beta}{2\pi} (-\delta - \epsilon_\beta - \mu_L) \right) + \psi \left(\frac{1}{2} + \frac{i\beta}{2\pi} (-\delta + \epsilon_\beta - \mu_L) \right) \Bigg] \\
&\quad + \frac{-\gamma}{\delta + \epsilon_{\rm as}} \Bigg[\pi i [(1 - f_L(\delta - \epsilon_\alpha)) - (1 - f_L(\delta + \epsilon_\alpha))] \\
&\quad + \psi \left(\frac{1}{2} + \frac{i\beta}{2\pi} (\delta + \epsilon_\alpha - \mu_L) \right) - \psi \left(\frac{1}{2} + \frac{i\beta}{2\pi} (\delta - \epsilon_\alpha - \mu_L) \right) \Bigg] \\
&\quad + \frac{\gamma}{\delta + \epsilon_{\rm as}} \Bigg[\pi i [(1 - f_R(\delta - \epsilon_\alpha)) - (1 - f_R(\delta + \epsilon_\alpha))] \\
&\quad + \psi \left(\frac{1}{2} + \frac{i\beta}{2\pi} (\delta + \epsilon_\alpha - \mu_R) \right) - \psi \left(\frac{1}{2} + \frac{i\beta}{2\pi} (\delta - \epsilon_\alpha - \mu_R) \right) \Bigg] \Bigg\} \qquad \text{(B.13)}
\end{aligned}
$$

$$
\begin{aligned}
\langle \tilde{H}_I \rangle_{-+} &= c_3 \Bigg\{ \frac{-\gamma}{\delta + \epsilon_{\rm as}} \Bigg[\pi i [f_R(\delta + \epsilon_\beta) - f_R(\delta - \epsilon_\beta)] \\
&\quad - \psi \left(\frac{1}{2} + \frac{i\beta}{2\pi} (\delta - \epsilon_\beta - \mu_R) \right) + \psi \left(\frac{1}{2} + \frac{i\beta}{2\pi} (\delta + \epsilon_\beta - \mu_R) \right) \Bigg] \\
&\quad + \frac{\gamma}{\delta + \epsilon_{\rm as}} \Bigg[\pi i [f_l(\delta + \epsilon_\beta) - f_L(\delta - \epsilon_\beta)] \\
&\quad - \psi \left(\frac{1}{2} + \frac{i\beta}{2\pi} (\delta - \epsilon_\beta - \mu_L) \right) + \psi \left(\frac{1}{2} + \frac{i\beta}{2\pi} (\delta + \epsilon_\beta - \mu_L) \right) \Bigg] \\
&\quad + \frac{-\gamma}{\delta + \epsilon_{\rm as}} \Bigg[\pi i [(1 - f_L(-\delta - \epsilon_\alpha)) - (1 - f_L(-\delta + \epsilon_\alpha))] \\
&\quad + \psi \left(\frac{1}{2} + \frac{i\beta}{2\pi} (-\delta + \epsilon_\alpha - \mu_L) \right) - \psi \left(\frac{1}{2} + \frac{i\beta}{2\pi} (-\delta - \epsilon_\alpha - \mu_L) \right) \Bigg] \\
&\quad + \frac{\gamma}{\delta + \epsilon_{\rm as}} \Bigg[\pi i [(1 - f_R(-\delta - \epsilon_\alpha)) - (1 - f_R(-\delta + \epsilon_\alpha))] \\
&\quad + \psi \left(\frac{1}{2} + \frac{i\beta}{2\pi} (-\delta + \epsilon_\alpha - \mu_R) \right) - \psi \left(\frac{1}{2} + \frac{i\beta}{2\pi} (-\delta - \epsilon_\alpha - \mu_R) \right) \Bigg] \Bigg\} \qquad \text{(B.14)}
\end{aligned}
$$

If one carries out the usual approximations ($\psi(x) \to \ln(x)$ and $\psi'(x) \to \frac{1}{x}$), one finds

$$\begin{aligned}
\langle \tilde{H}_I \rangle_{++} &= c_3 \Bigg\{ \ln\left(\frac{-\delta+\epsilon_\beta-\mu_R}{\delta-\epsilon_\beta-\mu_R}\right) + \frac{\gamma^2}{(\delta+\epsilon_{\rm as})^2} \ln\left(\frac{-\delta+\epsilon_\beta-\mu_L}{\delta-\epsilon_\beta-\mu_L}\right) \\
&\quad + \ln\left(\frac{\delta+\epsilon_\alpha-\mu_L}{-\delta-\epsilon_\alpha-\mu_L}\right) + \frac{\gamma^2}{(\delta+\epsilon_{\rm as})^2} \ln\left(\frac{\delta+\epsilon_\alpha-\mu_R}{-\delta-\epsilon_\alpha-\mu_R}\right) \Bigg\} \qquad \text{(B.15)} \\
\langle \tilde{H}_I \rangle_{--} &= c_3 \Bigg\{ \frac{\gamma^2}{(\delta+\epsilon_{\rm as})^2} \ln\left(\frac{\delta+\epsilon_\beta-\mu_R}{-\delta-\epsilon_\beta-\mu_R}\right) + \ln\left(\frac{\delta+\epsilon_\beta-\mu_L}{-\delta-\epsilon_\beta-\mu_L}\right) \\
&\quad + \frac{\gamma^2}{(\delta+\epsilon_{\rm as})^2} \ln\left(\frac{-\delta+\epsilon_\alpha-\mu_L}{\delta-\epsilon_\alpha-\mu_L}\right) + \ln\left(\frac{-\delta+\epsilon_\alpha-\mu_R}{\delta-\epsilon_\alpha-\mu_R}\right) \Bigg\} \qquad \text{(B.16)} \\
\langle \tilde{H}_I \rangle_{+-} &= c_3 \frac{\gamma}{\delta+\epsilon_{\rm as}} \Bigg\{ - \ln\left(\frac{-\delta+\epsilon_\beta-\mu_R}{-\delta-\epsilon_\beta-\mu_R}\right) + \ln\left(\frac{-\delta+\epsilon_\beta-\mu_L}{-\delta-\epsilon_\beta-\mu_L}\right) \\
&\quad - \ln\left(\frac{\delta+\epsilon_\alpha-\mu_L}{\delta-\epsilon_\alpha-\mu_L}\right) + \ln\left(\frac{\delta+\epsilon_\alpha-\mu_R}{\delta-\epsilon_\alpha-\mu_R}\right) \Bigg\} \qquad \text{(B.17)} \\
\langle \tilde{H}_I \rangle_{-+} &= c_3 \frac{\gamma}{\delta+\epsilon_{\rm as}} \Bigg\{ - \ln\left(\frac{\delta+\epsilon_\beta-\mu_R}{\delta-\epsilon_\beta-\mu_R}\right) + \ln\left(\frac{\delta+\epsilon_\beta-\mu_L}{\delta-\epsilon_\beta-\mu_L}\right) \\
&\quad - \ln\left(\frac{-\delta+\epsilon_\alpha-\mu_L}{-\delta-\epsilon_\alpha-\mu_L}\right) + \ln\left(\frac{-\delta+\epsilon_\alpha-\mu_R}{-\delta-\epsilon_\alpha-\mu_R}\right) \Bigg\} . \qquad \text{(B.18)}
\end{aligned}$$

Appendix C

Rules for the integrals

In order to evaluate the $\Gamma^{(+)}$ rates, we have to consider all integrals of the general form (4.16) that appear in equation (4.6). Each of these integrals has two integration variables and can be determined by the rules that follow below. For the $\Gamma^{(-)}$ rates an analogous consideration has been done. ϵ_1 and ϵ_2 are the generic integration variables. The ωs belong to the equations (4.6) and (4.7); their definition can be found in Chapter 4.

C.1 Rules for $\Gamma^{(+)}$

general case:

$$\Gamma^{(+)} = c\,\frac{-n_1(\mu_2 \mp 2\delta)}{\epsilon_b - \epsilon_a \mp 2\delta}\left[\ln\left(\frac{\epsilon_b - \mu_1 \mp 2\delta}{\epsilon_a - \mu_1}\right) + \ln\left(\frac{\epsilon_a - \mu_2 \pm 2\delta}{\epsilon_b - \mu_2}\right)\right] \tag{C.1}$$

C.1.1 $\omega_{nk} = 0$

i) $\mu_1 = \mu_2$:

$$\Gamma^{(+)} = c\,\frac{1}{\epsilon_b - \epsilon_a}\;k_{\mathrm{B}}T\;\left[\frac{1}{\epsilon_a - \mu_1} - \frac{1}{\epsilon_b - \mu + 1}\right] \tag{C.2}$$

ii) $\epsilon_a = \epsilon_b$:

$$\Gamma^{(+)} = c\,(-n_1(\mu_2))\left[\frac{1}{\epsilon_a - \mu_1} - \frac{1}{\epsilon_a - \mu_2}\right] \tag{C.3}$$

iii) $\mu_1 = \mu_2$ and $\epsilon_a = \epsilon_b$:

$$\Gamma^{(+)} = c\,k_{\mathrm{B}}T\;\frac{1}{(\epsilon_a - \mu_1)^2} \tag{C.4}$$

C.1.2 $\omega_{nk} \neq 0$

i) two integration variables ϵ_1:

$$\Gamma^{(+)} = c\,\frac{-n_1(\mu_2 \mp 2\delta)}{\epsilon_b - \epsilon_a \mp 2\delta}\left[\ln\left(\frac{\epsilon_b - \mu_1}{\epsilon_a - \mu_1}\right) + \ln\left(\frac{\epsilon_a - \mu_2 \pm 2\delta}{\epsilon_b - \mu_2 \pm 2\delta}\right)\right] \tag{C.5}$$

ii) two integration variables ϵ_2:

$$\Gamma^{(+)} = c\,\frac{-n_1(\mu_2 \mp 2\delta)}{\epsilon_b - \epsilon_a \mp 2\delta}\left[\ln\left(\frac{\epsilon_b - \mu_1 \mp 2\delta}{\epsilon_a - \mu_1 \mp 2\delta}\right) + \ln\left(\frac{\epsilon_a - \mu_2}{\epsilon_b - \mu_2}\right)\right] \tag{C.6}$$

iii) $\epsilon_b = \epsilon_a \pm 2\delta$:

$$\Gamma^{(+)} = c\,(-n_1(\mu_2 \mp 2\delta))\left[\frac{1}{\epsilon_a - \mu_1} - \frac{1}{\epsilon_b - \mu_2}\right] \tag{C.7}$$

iv) two integration variables ϵ_1 or ϵ_2 and $\epsilon_a = \epsilon_b$:

$$\Gamma^{(+)} = 0 \tag{C.8}$$

C.2 Rules for $\Gamma^{(-)}$

general case:

$$\Gamma^{(-)} = c\,\frac{-n_2(\mu_1 \pm 2\delta)}{\epsilon_b - \epsilon_a \mp 2\delta}\left[\ln\left(\frac{\epsilon_a - \mu_1}{\epsilon_b - \mu_1 \mp 2\delta}\right) + \ln\left(\frac{\epsilon_b - \mu_2}{\epsilon_a - \mu_2 \pm 2\delta}\right)\right] \tag{C.9}$$

C.2.1 $\omega_{lm} = 0$

i) $\mu_1 = \mu_2$:

$$\Gamma^{(-)} = c\,\frac{1}{\epsilon_b - \epsilon_a}\,k_{\mathrm{B}}T\,\left[\frac{1}{\epsilon_a - \mu_1} - \frac{1}{\epsilon_b - \mu + 1}\right] \tag{C.10}$$

ii) $\epsilon_a = \epsilon_b$:

$$\Gamma^{(-)} = c\,(-n_2(\mu_1))\left[\frac{1}{\epsilon_a - \mu_2} - \frac{1}{\epsilon_a - \mu_1}\right] \tag{C.11}$$

iii) $\mu_1 = \mu_2$ and $\epsilon_a = \epsilon_b$:

$$\Gamma^{(-)} = c\,k_{\mathrm{B}}T\,\frac{1}{(\epsilon_a - \mu_1)^2} \tag{C.12}$$

C.2.2 $\omega_{lm} \neq 0$

i) two integration variables ϵ_1:

$$\Gamma^{(-)} = c\,\frac{-n_2(\mu_1 \pm 2\delta)}{\epsilon_b - \epsilon_a \mp 2\delta}\left[\ln\left(\frac{\epsilon_a - \mu_1}{\epsilon_b - \mu_1}\right) + \ln\left(\frac{\epsilon_b - \mu_2 \pm 2\delta}{\epsilon_a - \mu_2 \pm 2\delta}\right)\right] \tag{C.13}$$

ii) two integration variables ϵ_2:

$$\Gamma^{(-)} = c\,\frac{-n_2(\mu_1 \pm 2\delta)}{\epsilon_b - \epsilon_a \mp 2\delta}\left[\ln\left(\frac{\epsilon_a - \mu_1 \mp 2\delta}{\epsilon_b - \mu_1 \mp 2\delta}\right) + \ln\left(\frac{\epsilon_b - \mu_2}{\epsilon_a - \mu_2}\right)\right] \tag{C.14}$$

iii) $\epsilon_b = \epsilon_a \pm 2\delta$:

$$\Gamma^{(-)} = c\,(-n_2(\mu_1 \pm 2\delta))\left[\frac{1}{\epsilon_b - \mu_2} - \frac{1}{\epsilon_a - \mu_1}\right] \tag{C.15}$$

iv) two integration variables ϵ_1 or ϵ_2 and $\epsilon_a = \epsilon_b$:

$$\Gamma^{(-)} = 0 \tag{C.16}$$

Appendix D

Functions for the atomic limit

One can evaluate the functions Z, Y_1, Y_{-1} and $Y_{1,-1}$ in equations (4.39)-(4.43), if one applies equations (4.22) and (4.23) from the general case or the rules from Appendix C to all summands in the nonvanishing $\Gamma^{(\pm)}$'s in (4.28)-(4.33). This was done by hand.

$$
\begin{aligned}
Z \;=\;& \frac{1}{4\epsilon_{\mathrm{as}}}\left[\ln\left(\frac{3\epsilon_{\mathrm{as}}+\epsilon_\beta-\mu_R}{-\epsilon_{\mathrm{as}}+\epsilon_\beta-\mu_R}\right)+\ln\left(\frac{-3\epsilon_{\mathrm{as}}+\epsilon_\beta-\mu_L}{\epsilon_{\mathrm{as}}+\epsilon_\beta-\mu_L}\right)\right]\\
&-\frac{1}{2(\epsilon_{\mathrm{as}}-\epsilon_\beta)+2\epsilon_{\mathrm{as}}}\left[\ln\left(\frac{\epsilon_{\mathrm{as}}-\epsilon_\beta-\mu_R}{-\epsilon_{\mathrm{as}}+\epsilon_\beta-\mu_R}\right)+\ln\left(\frac{-3\epsilon_{\mathrm{as}}+\epsilon_\beta-\mu_L}{-\epsilon_{\mathrm{as}}-\epsilon_\beta-\mu_L}\right)\right]\\
&-\frac{1}{2(\epsilon_{\mathrm{as}}+\epsilon_\beta)+2\epsilon_{\mathrm{as}}}\left[\ln\left(\frac{3\epsilon_{\mathrm{as}}+\epsilon_\beta-\mu_R}{\epsilon_{\mathrm{as}}-\epsilon_\beta-\mu_R}\right)+\ln\left(\frac{-\epsilon_{\mathrm{as}}-\epsilon_\beta-\mu_L}{\epsilon_{\mathrm{as}}+\epsilon_\beta-\mu_L}\right)\right]\\
&+\left[\frac{1}{\epsilon_{\mathrm{as}}-\epsilon_\beta-\mu_R}-\frac{1}{-\epsilon_{\mathrm{as}}-\epsilon_\beta-\mu_L}\right]\\
&+\frac{1}{2\epsilon_{\mathrm{as}}+\epsilon_\beta-\epsilon_\alpha}\left[\ln\left(\frac{-\epsilon_{\mathrm{as}}+\epsilon_\beta-\mu_R}{-\epsilon_{\mathrm{as}}+\epsilon_\alpha-\mu_R}\right)+\ln\left(\frac{-3\epsilon_{\mathrm{as}}+\epsilon_\alpha-\mu_L}{-3\epsilon_{\mathrm{as}}+\epsilon_\beta-\mu_L}\right)\right]\\
&-\frac{1}{2\epsilon_{\mathrm{as}}-\epsilon_\alpha-\epsilon_\beta}\left[\ln\left(\frac{\epsilon_{\mathrm{as}}-\epsilon_\alpha-\mu_R}{-\epsilon_{\mathrm{as}}+\epsilon_\beta-\mu_R}\right)+\ln\left(\frac{-3\epsilon_{\mathrm{as}}+\epsilon_\beta-\mu_L}{-\epsilon_{\mathrm{as}}-\epsilon_\alpha-\mu_L}\right)\right]\\
&-\frac{1}{2\epsilon_{\mathrm{as}}-\epsilon_\alpha-\epsilon_\beta}\left[\ln\left(\frac{\epsilon_{\mathrm{as}}-\epsilon_\beta-\mu_R}{-\epsilon_{\mathrm{as}}+\epsilon_\alpha-\mu_R}\right)+\ln\left(\frac{-3\epsilon_{\mathrm{as}}+\epsilon_\alpha-\mu_L}{-\epsilon_{\mathrm{as}}-\epsilon_\beta-\mu_L}\right)\right]\\
&+\frac{1}{2\epsilon_{\mathrm{as}}+\epsilon_\beta-\epsilon_\alpha}\left[\ln\left(\frac{\epsilon_{\mathrm{as}}-\epsilon_\alpha-\mu_R}{\epsilon_{\mathrm{as}}-\epsilon_\beta-\mu_R}\right)+\ln\left(\frac{-\epsilon_{\mathrm{as}}-\epsilon_\beta-\mu_L}{-\epsilon_{\mathrm{as}}-\epsilon_\alpha-\mu_L}\right)\right]\\
&+\frac{1}{2\epsilon_{\mathrm{as}}+\epsilon_\beta-\epsilon_\alpha}\left[\ln\left(\frac{3\epsilon_{\mathrm{as}}+\epsilon_\beta-\mu_R}{3\epsilon_{\mathrm{as}}+\epsilon_\alpha-\mu_R}\right)+\ln\left(\frac{\epsilon_{\mathrm{as}}+\epsilon_\alpha-\mu_L}{\epsilon_{\mathrm{as}}+\epsilon_\beta-\mu_L}\right)\right]\\
&-\frac{1}{2\epsilon_{\mathrm{as}}+\epsilon_\alpha+\epsilon_\beta}\left[\ln\left(\frac{3\epsilon_{\mathrm{as}}+\epsilon_\alpha-\mu_R}{\epsilon_{\mathrm{as}}-\epsilon_\beta-\mu_R}\right)+\ln\left(\frac{-\epsilon_{\mathrm{as}}-\epsilon_\beta-\mu_L}{\epsilon_{\mathrm{as}}+\epsilon_\alpha-\mu_L}\right)\right]\\
&-\frac{1}{2\epsilon_{\mathrm{as}}+\epsilon_\alpha+\epsilon_\beta}\left[\ln\left(\frac{3\epsilon_{\mathrm{as}}+\epsilon_\beta-\mu_R}{\epsilon_{\mathrm{as}}-\epsilon_\alpha-\mu_R}\right)+\ln\left(\frac{-\epsilon_{\mathrm{as}}-\epsilon_\alpha-\mu_L}{\epsilon_{\mathrm{as}}+\epsilon_\beta-\mu_L}\right)\right]
\end{aligned}
$$

$$
\begin{aligned}
&+\frac{1}{2\epsilon_{\rm as}+\epsilon_\beta-\epsilon_\alpha}\left[\ln\left(\frac{\epsilon_{\rm as}-\epsilon_\alpha-\mu_R}{\epsilon_{\rm as}-\epsilon_\beta-\mu_R}\right)+\ln\left(\frac{-\epsilon_{\rm as}-\epsilon_\beta-\mu_L}{-\epsilon_{\rm as}-\epsilon_\alpha-\mu_L}\right)\right]\\
&+\frac{1}{4\epsilon_{\rm as}}\left[\ln\left(\frac{3\epsilon_{\rm as}+\epsilon_\alpha-\mu_R}{-\epsilon_{\rm as}+\epsilon_\alpha-\mu_R}\right)+\ln\left(\frac{-3\epsilon_{\rm as}+\epsilon_\alpha-\mu_L}{\epsilon_{\rm as}+\epsilon_\alpha-\mu_L}\right)\right]\\
&-\frac{1}{2(\epsilon_{\rm as}+\epsilon_\alpha)+2\epsilon_{\rm as}}\left[\ln\left(\frac{3\epsilon_{\rm as}+\epsilon_\alpha-\mu_R}{\epsilon_{\rm as}-\epsilon_\alpha-\mu_R}\right)+\ln\left(\frac{-\epsilon_{\rm as}-\epsilon_\alpha-\mu_L}{\epsilon_{\rm as}+\epsilon_\alpha-\mu_L}\right)\right]\\
&-\frac{1}{2(\epsilon_{\rm as}-\epsilon_\alpha)+2\epsilon_{\rm as}}\left[\ln\left(\frac{\epsilon_{\rm as}-\epsilon_\alpha-\mu_R}{-\epsilon_{\rm as}+\epsilon_\alpha-\mu_R}\right)+\ln\left(\frac{-3\epsilon_{\rm as}+\epsilon_\alpha-\mu_L}{-\epsilon_{\rm as}-\epsilon_\alpha-\mu_L}\right)\right]\\
&+\left[\frac{1}{\epsilon_{\rm as}-\epsilon_\alpha-\mu_R}-\frac{1}{-\epsilon_{\rm as}-\epsilon_\alpha-\mu_L}\right]
\end{aligned}
\tag{D.1}
$$

$$
\begin{aligned}
Y_1 \;=\;& \frac{1}{(\epsilon_{\rm as}+\epsilon_\alpha-\mu_L)^2}+\frac{1}{(-\epsilon_{\rm as}-\epsilon_\alpha-\mu_L)^2}-\frac{1}{\epsilon_{\rm as}+\epsilon_\alpha}\left[\frac{1}{-\epsilon_{\rm as}-\epsilon_\alpha-\mu_L}-\frac{1}{\epsilon_{\rm as}+\epsilon_\alpha-\mu_L}\right]\\
&+\frac{1}{(-\epsilon_{\rm as}+\epsilon_\beta-\mu_R)^2}+\frac{1}{(\epsilon_{\rm as}-\epsilon_\beta-\mu_R)^2}-\frac{1}{\epsilon_{\rm as}-\epsilon_\beta}\left[\frac{1}{-\epsilon_{\rm as}+\epsilon_\beta-\mu_R}-\frac{1}{\epsilon_{\rm as}-\epsilon_\beta-\mu_R}\right]
\end{aligned}
\tag{D.2}
$$

$$
\begin{aligned}
Y_{-1} \;=\;& \frac{1}{(\epsilon_{\rm as}+\epsilon_\beta-\mu_L)^2}+\frac{1}{(-\epsilon_{\rm as}-\epsilon_\beta-\mu_L)^2}-\frac{1}{\epsilon_{\rm as}+\epsilon_\beta}\left[\frac{1}{-\epsilon_{\rm as}-\epsilon_\beta-\mu_L}-\frac{1}{\epsilon_{\rm as}+\epsilon_\beta-\mu_L}\right]\\
&+\frac{1}{(-\epsilon_{\rm as}+\epsilon_\alpha-\mu_R)^2}+\frac{1}{(\epsilon_{\rm as}-\epsilon_\alpha-\mu_R)^2}-\frac{1}{\epsilon_{\rm as}-\epsilon_\alpha}\left[\frac{1}{-\epsilon_{\rm as}+\epsilon_\alpha-\mu_R}-\frac{1}{\epsilon_{\rm as}-\epsilon_\alpha-\mu_R}\right]
\end{aligned}
\tag{D.3}
$$

$$
\begin{aligned}
Y_{1,-1} \;=\;& \frac{1}{\epsilon_\beta-\epsilon_\alpha}\left[\frac{1}{\epsilon_{\rm as}+\epsilon_\alpha-\mu_L}-\frac{1}{\epsilon_{\rm as}+\epsilon_\beta-\mu_L}-\frac{1}{-\epsilon_{\rm as}-\epsilon_\alpha-\mu_L}+\frac{1}{-\epsilon_{\rm as}-\epsilon_\beta-\mu_L}\right]\\
&-\frac{1}{2\epsilon_{\rm as}+\epsilon_\alpha+\epsilon_\beta}\left[-\frac{1}{\epsilon_{\rm as}+\epsilon_\alpha-\mu_L}-\frac{1}{\epsilon_{\rm as}+\epsilon_\beta-\mu_L}+\frac{1}{-\epsilon_{\rm as}-\epsilon_\alpha-\mu_L}+\frac{1}{-\epsilon_{\rm as}-\epsilon_\beta-\mu_L}\right]\\
&+\frac{1}{\epsilon_\beta-\epsilon_\alpha}\left[\frac{1}{-\epsilon_{\rm as}+\epsilon_\alpha-\mu_R}-\frac{1}{-\epsilon_{\rm as}+\epsilon_\beta-\mu_R}-\frac{1}{\epsilon_{\rm as}-\epsilon_\alpha-\mu_R}+\frac{1}{\epsilon_{\rm as}-\epsilon_\beta-\mu_R}\right]\\
&-\frac{1}{2\epsilon_{\rm as}-\epsilon_\alpha-\epsilon_\beta}\left[\frac{1}{-\epsilon_{\rm as}+\epsilon_\alpha-\mu_R}+\frac{1}{-\epsilon_{\rm as}+\epsilon_\beta-\mu_R}-\frac{1}{\epsilon_{\rm as}-\epsilon_\alpha-\mu_R}-\frac{1}{\epsilon_{\rm as}-\epsilon_\beta-\mu_R}\right]
\end{aligned}
\tag{D.4}
$$

Appendix E

Some Comments on the Implementation

In order to get expressions for the rates $\Gamma^{(\pm)}_{lmnk}$ in equation (4.5), we implemented the large sums in equations (4.6) and (4.7) in Maple V (Release 7). After this, we have been able to combine these rates to obtain the Redfield tensor elements. The diagonalization of the tensor and the solution of the Redfield equations (4.4) followed then in a straightforward way. The current expression contained terms that were similar to the rates $\Gamma^{(\pm)}_{lmnk}$, consequently the implementation of the rates could partially be used.

The special thing about this implementation is that we used string manipulation to accomplish our calculations. First, the products of the required Schrieffer-Wolff coefficients (see Appendix A) have been evaluated, then these expressions have been parsed for specific parameters to obtain the summands of the final rate via the rules in Appendix C. Finally everything was summed up and one could give values to the parameters to receive some plots or numbers.

One further remark is requested: the actual implementation works only with Maple V (Release 7) or better, because the package "StringTools" did not exist in an earlier version of Maple. On the long term, an implementation in a real programming language like C or C++ is required and planned [e.g. by compiling the Maple code with Matlab or the new Maple V (Release 8)].

Appendix F

Some 3D Pictures

The pictures below [generated with Maple V (Release 7)] have been taken to show the borders of our theory.

F.1 Relaxation time

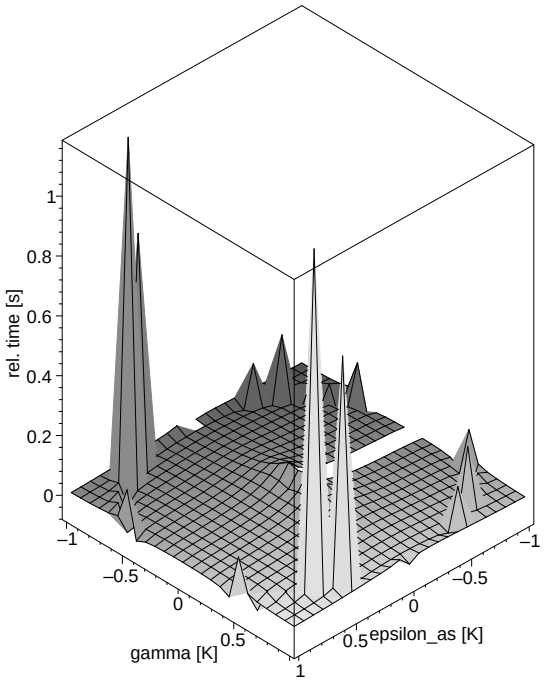

Figure F.1: Relaxation time τ_r when $\epsilon_{\rm as}$ and γ are varied; $V = 0.06$ K, $\mu_{\rm av} = 0.88$ K and $T = 0.14$ K

We found some not forseeable peaks here, therefore we do not trust our theory, if $\epsilon_{\rm as}$ or γ is much larger than 0.5 K.

F.2 Dephasing time

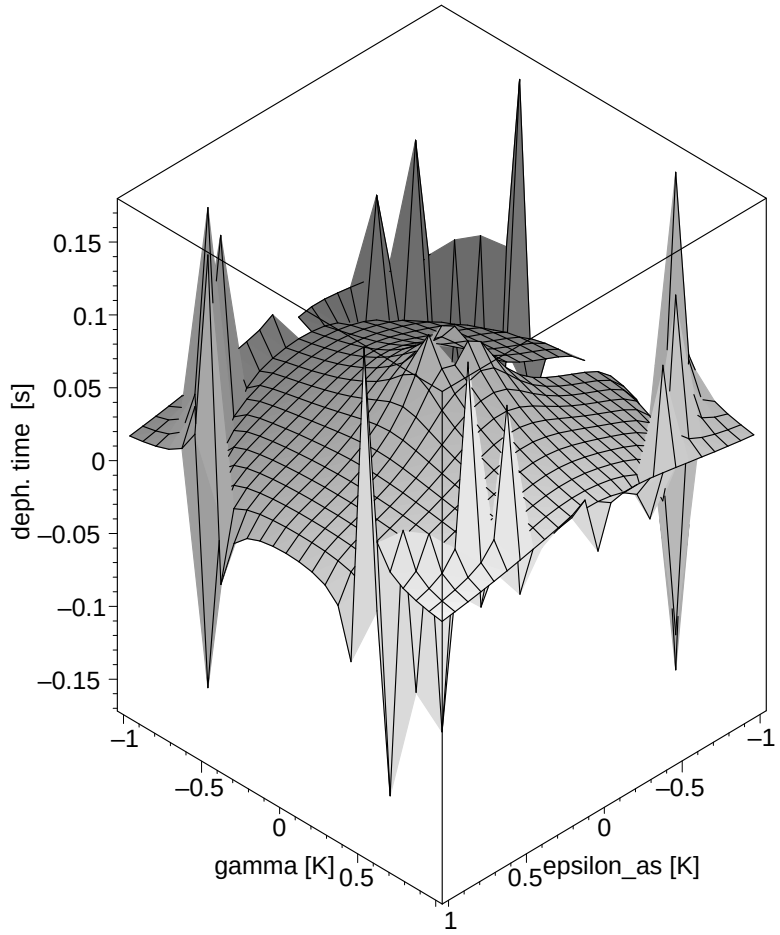

Figure F.2: Dephasing time τ_ϕ when ϵ_{as} and γ are varied; $V = 0.06$ K, $\mu_{\text{av}} = 0.88$ K and $T = 0.14$ K

Even negative dephasing times are possible according to this plot. This is of course not consistent with our understanding of the processes. A quantum state can decay, but not improve its stability.

F.3 Stationary current

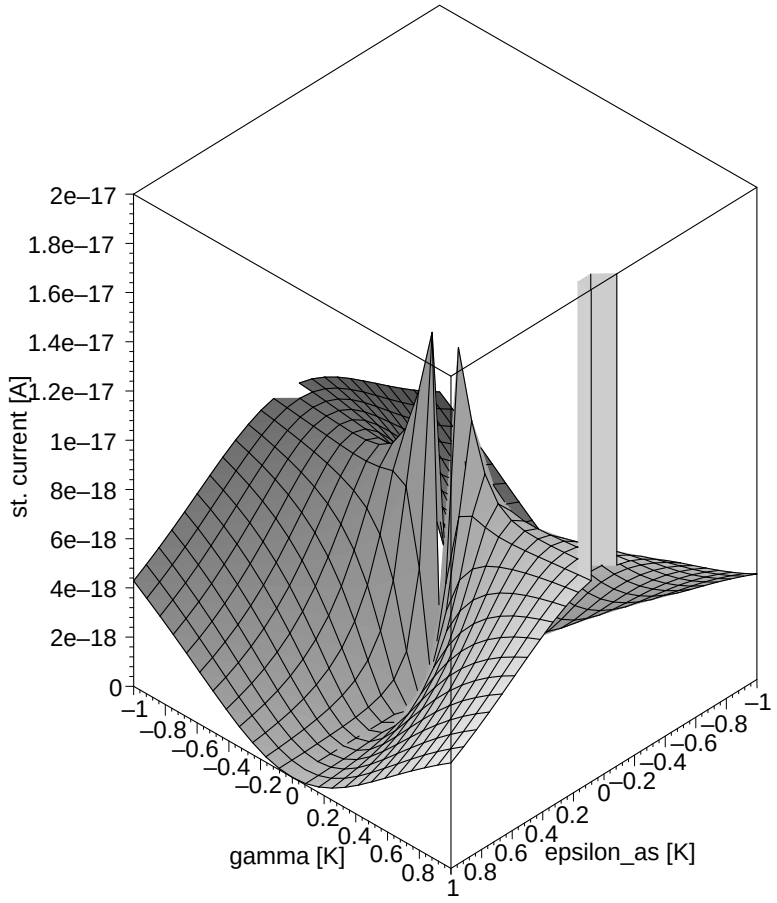

Figure F.3: Stationary current I_{st} when ϵ_{as} and γ are varied; $V = 0.06$ K, $\mu_{\text{av}} = 0.88$ K and $T = 0.14$ K

In this picture, one can see two areas where the values of the stationary current are not defined or in a very huge peak. These areas are another reason to restrict our analysis to small values of ϵ_{as} and γ.

Used symbols

symbol	meaning
H	Hamiltonian
H_0	unperturbed Hamiltonian
H_1	perturbation Hamiltonian
H_{sys}	Hamiltonian of the double-dot system
H_{res}	Hamiltonian of the leads
H_I or $H_{I,\mathrm{eff}}$	effective interaction Hamiltonian for the coupling between dots and leads
$\tilde{H}_I$	effective interaction Hamiltonian in the interaction picture
$A(\cdot)$	Schrieffer-Wolff coefficient (see Appendix A)
$a^{R/L\dagger}_{n/m}$, $a^{R/L}_{n/m}$	creation and annihilation operators acting on the right/left dot
$b^{R/L\dagger}_{m/k}$, $b^{R/L}_{n/l}$	creation and annihilation operators acting on the right/left lead
$\epsilon_{\mathrm{as}} = (\epsilon_l - \epsilon_r)/2$	asymmetry energy between energy levels in the left and the right dot
γ	inter-dot coupling
t_c	strength of the coupling between the dots and the leads
$\delta = \sqrt{\epsilon_{\mathrm{as}}^2 + \gamma^2}$	half level splitting in the molecular basis
R_{nmkl}	Redfield tensor elements
R	Redfield tensor with included ω_{nm}
$\Gamma^{(\pm)}_{lmnk}$	rates that construct the Redfield tensor elements
Γ_r	relaxation rate
$\tau_r = \frac{1}{\Gamma_r}$	relaxation time
Γ_ϕ	dephasing rate
$\tau_\phi = \frac{1}{\Gamma_\phi}$	dephasing time
ρ_{nm}	elements of the reduced density matrix
W	density matrix of the whole system
$\omega_{nm} = (E_n - E_m)/\hbar$	angular frequency of the coherent oscillations
E_n	eigenenergy of state n
t	time
T	temperature
$\epsilon^{L/R}_s$	energies in the left/right lead
$\mu_{L/R}$	electrochemical potential of the left/right lead
$\mu_{\mathrm{av}} = (\mu_R + \mu_L)/2$	average of the electrochemical potentials of both leads
$V = \mu_R - \mu_L$	bias voltage

symbol	meaning
I	current
I_{st}	stationary current
G	conductance
ϵ_β	charging energy to reach the $\|\beta\rangle$ state
ϵ_α	charging energy to reach the $\|\alpha\rangle$ state
$n_{L/R}(\epsilon)$	Bose function for the left/right lead
$f_{L/R}(\epsilon)$	Fermi function for the left/right lead
N_L	particle counting operator on the left dot
C	diagonized R (with ω_{nm} included)
B and B^{-1}	matrices that diagonalize R
ψ	Digamma function
ψ'	Trigamma function
$S = \sqrt{1 + \frac{\gamma^2}{(\delta+\gamma)^2}}$	normalization factor for the molecular states
n	number of electrons in the leads
V_{2DEG}	volume of the leads (two dimensional electron gas)
m_*	reduced mass in the leads
E_F	Fermi energy of the leads
$\beta = \frac{1}{k_{\mathrm{B}}T}$	inverse temperature
$k_{\mathrm{B}} = 1.38 \cdot 10^{-23}$ J/K	Boltzmann constant
$\hbar = 1.05 \cdot 10^{-34}$ Js	Planck constant over 2π
c, c_1, c_2 and c_3	constants stemming from the density of states in the leads
δ_{lm}	Kronecker symbol
$\delta(\epsilon)$	Dirac delta function
$tr(\cdot)$	trace of $\cdot$
B_{P}	strength of the magnetic field, which is needed to polarize the spins of the electrons
$\mu_{\mathrm{B}} = 9.27 \cdot 10^{-24}$ Am^2	Bohr magneton
g_{P}	Landé g factor
T_{K}	Kondo temperature
Z, Y_1, Y_{-1} and $Y_{1,-1}$	specific functions for the atomic limit (see Appendix D)
α	strength of the dissipation in the Spin-Boson model
$J(\epsilon)$	spectral density of a bosonic bath
θ	angle between the z-axis and an effective magnetic field $\vec{B}_{\mathrm{eff}}$ in NMR notation
σ	generalized cross section
κ	generalized spectral density

List of Figures

1.1 (a) Sketch of the double dot system, (b) scanning electron microscope (SEM) picture of a real double dot system 4

2.1 Energy spectrum of the system before and after a diagonalization; δ is defined as $\delta = \sqrt{\epsilon_{\rm as}^2 + \gamma^2}$. 7
2.2 Sketch of the two phases for the Gedanken experiment: (a) superposition, (b) atomic limit 8

3.1 Principle of the generalized Schrieffer-Wolff transformation 10
3.2 Sketch of the virtual processes involved in (a) $H_{I,++}$, (b) $H_{I,--}$, (c) $H_{I,+-}$ and (d) $H_{I,-+}$ 11

6.1 Relaxation times τ_r for different values of $\epsilon_{\rm as}$ when the coupling strength γ is varied (with $T = 0.14$ K, $V = 0.06$ K and $\mu_{\rm av} = 0.88$ K) 26
6.2 Relaxation times τ_r for different values of γ when the asymmetry energy $\epsilon_{\rm as}$ is varied (with $T = 0.14$ K, $V = 0.06$ K and $\mu_{\rm av} = 0.88$ K) 27
6.3 Relaxation times τ_r for different values of $\epsilon_{\rm as}$ and γ when the temperature T is varied (with $V = 0.06$ K and $\mu_{\rm av} = 0.88$ K) 28
6.4 Relaxation times τ_r for different values of $\epsilon_{\rm as}$ and γ when the bias voltage V is varied: (a) at $T = 0.1$ mK, $\mu_{\rm av} = 0.88$ K, (b) at $T = 0.14$ K, $\mu_{\rm av} = 0.88$ K, (c) at $T = 0.1$ mK, $\mu_{\rm av} = 4$ K and (d) at $T = 0.14$ K, $\mu_{\rm av} = 4$ K 29
6.5 Dephasing times τ_ϕ for different values of $\epsilon_{\rm as}$ when the coupling strength γ is varied (with $T = 0.14$ K, $V = 0.06$ K and $\mu_{\rm av} = 0.88$ K) 30
6.6 Dephasing times τ_ϕ for different values of γ when the asymmetry energy $\epsilon_{\rm as}$ is varied (with $T = 0.14$ K, $V = 0.06$ K and $\mu_{\rm av} = 0.88$ K) 31
6.7 Dephasing times τ_ϕ for different values of $\epsilon_{\rm as}$ and γ when the temperature T is varied (with $V = 0.06$ K and $\mu_{\rm av} = 0.88$ K) 32
6.8 Dephasing times τ_ϕ for different values of $\epsilon_{\rm as}$ and γ when the bias voltage V is varied: (a) at $T = 0.1$ mK, $\mu_{\rm av} = 0.88$ K, (b) at $T = 0.14$ K, $\mu_{\rm av} = 0.88$ K, (c) at $T = 0.1$ mK, $\mu_{\rm av} = 4$ K and (d) at $T = 0.14$ K, $\mu_{\rm av} = 4$ K 33
6.9 Stationary current $I_{\rm st}$ for different values of $\epsilon_{\rm as}$ when the coupling strength γ is varied (with $T = 0.14$ K, $V = 0.06$ K and $\mu_{\rm av} = 0.88$ K) 34

6.10 Stationary current $I_{\rm st}$ for different values of γ when the asymmetry energy $\epsilon_{\rm as}$ is varied (with $T = 0.14$ K, $V = 0.06$ K and $\mu_{\rm av} = 0.88$ K) 35
6.11 Limits for the three transport regimes with the parameters $V = 0.06$ K and $t_c = 1.21$ mK 36
6.12 Stationary current $I_{\rm st}$ for different values of $\epsilon_{\rm as}$ and γ when the temperature T is varied (with $V = 0.06$ K and $\mu_{\rm av} = 0.88$ K) 37
6.13 Stationary $I_{\rm st}$-V characteristics for different values of $\epsilon_{\rm as}$ and γ: (a) at $T = 0.1$ mK, $\mu_{\rm av} = 0.88$ K, (b) at $T = 0.14$ K, $\mu_{\rm av} = 0.88$ K, (c) at $T = 0.1$ mK, $\mu_{\rm av} = 4$ K and (d) at $T = 0.14$ K, $\mu_{\rm av} = 4$ K 38
6.14 Conductance G for different values of $\epsilon_{\rm as}$ and γ when the bias voltage V is varied: (a) at $T = 0.1$ mK, $\mu_{\rm av} = 0.88$ K, (b) at $T = 0.14$ K, $\mu_{\rm av} = 0.88$ K, (c) at $T = 0.1$ mK, $\mu_{\rm av} = 4$ K and (d) at $T = 0.14$ K, $\mu_{\rm av} = 4$ K 39
6.15 Differential conductance $dI_{\rm st}/dV$ for different values of $\epsilon_{\rm as}$ and γ when the bias voltage V is varied: (a) at $T = 0.1$ mK, $\mu_{\rm av} = 0.88$ K, (b) at $T = 0.14$ K, $\mu_{\rm av} = 0.88$ K, (c) at $T = 0.1$ mK, $\mu_{\rm av} = 4$ K and (d) at $T = 0.14$ K, $\mu_{\rm av} = 4$ K 40
6.16 Difference of the stationary occupation probabilities $\rho_{++,\rm st} - \rho_{--,\rm st}$ for different values of $\epsilon_{\rm as}$ and γ when the bias voltage V is varied: (a) at $T = 0.1$ mK, $\mu_{\rm av} = 0.88$ K, (b) at $T = 0.14$ K, $\mu_{\rm av} = 0.88$ K, (c) at $T = 0.1$ mK, $\mu_{\rm av} = 4$ K and (d) at $T = 0.14$ K, $\mu_{\rm av} = 4$ K 41
6.17 Time-dependent reduced density matrix elements with the following parameters: $T = 0.14$ K, $\mu_{\rm av} = 0.88$ K and $\epsilon_{\rm as} = 0.1$ K; additionally (a) $V = 0.06$ K, $\gamma = 0.2$ K, (b) $V = 0.06$ K, $\gamma = 0$ K, (c) $V = 0$ K, $\gamma = 0.2$ K and (d) $V = 0$ K, $\gamma = 0$ K 42
6.18 Time-dependent cotunneling current through the double dot system with the parameters: $T = 0.14$ K, $\mu_{\rm av} = 0.88$ K and $\epsilon_{\rm as} = 0.1$ K; additionally (a) $V = 0.06$ K and (b) $V = 0$ K 43
6.19 Sketches for some "stable" [(a) and (b)] and "unstable" [(c) and (d)] configurations in the asymmetry energy $\epsilon_{\rm as}$ and the voltage V 44
6.20 Difference of the stationary occupation probabilities $\rho_{++,\rm st} - \rho_{--,\rm st}$ for varying $\epsilon_{\rm as}$ and V with $\gamma = 0.2$ K, $\epsilon_\beta = 11$ K, $\epsilon_\alpha = 9$ K, $T = 0.14$ K and $\mu_{\rm av} = 0.88$ K 45
6.21 Difference of the stationary occupation probabilities $\rho_{++,\rm st} - \rho_{--,\rm st}$ for varying $\epsilon_{\rm as}$ and V with $\gamma = 0.2$ K, $\epsilon_\beta = 11$ K, $\epsilon_\alpha = 9$ K, $T = 0.1$ mK and $\mu_{\rm av} = 0.88$ K 46

F.1 Relaxation time τ_r when $\epsilon_{\rm as}$ and γ are varied; $V = 0.06$ K, $\mu_{\rm av} = 0.88$ K and $T = 0.14$ K 70
F.2 Dephasing time τ_ϕ when $\epsilon_{\rm as}$ and γ are varied; $V = 0.06$ K, $\mu_{\rm av} = 0.88$ K and $T = 0.14$ K 71
F.3 Stationary current I_{st} when $\epsilon_{\rm as}$ and γ are varied; $V = 0.06$ K, $\mu_{\rm av} = 0.88$ K and $T = 0.14$ K 72

Bibliography

[1] R.P. Feynman, Int. J. Theor. Phys., **V 21**, 467 (1982).

[2] D. Deutsch, Proc. R. Soc. Lond. A **400**, 97 (1985).

[3] P. Shor, in Proc. 35th Ann. Symp. on the Foundations of Computer Science (ed. S. Goldwasser), pp. 124-134 (IEEE Computer Society Press, Los Alamitos, California, 1994).

[4] L.K. Grover, Phys. Rev. Lett. **79**, 325 (1997).

[5] J.I. Cirac and P. Zoller, Phys. Rev. Lett. **74**, 4091 (1995).

[6] J.I. Cirac, T. Pellizzari and P. Zoller, Science **273**, 1207 (1996).

[7] J.F. Poyatos, J.I. Cirac and P. Zoller, Phys. Rev. Lett. **78**, 390 (1997).

[8] N. Gershenfeld and I.L. Chuang, Science **275**, 350 (1997).

[9] A. Barenco et al., Phys. Rev. A **52**, 3457 (1995).

[10] C.H. Bennett, G. Brassard and A.K. Ekert, Sci. Am. **267**, 50 (1992).

[11] A.K. Ekert, Phys. Rev. Lett. **67**, 661 (1991).

[12] L.M.K. Vandersypen et al., Nature **414**, 883 (2001).

[13] M.J. Storcz, master's thesis, University of Bonn (2002).

[14] see e.g. M.A. Nielsen and I.L. Chuang, *Quantum Computation and Quantum Information*, (CUP, Cambridge, 2000).

[15] D. Loss and D. DiVincenzo, Phys. Rev. A **57**, pp. 120-126 (1998).

[16] P. Zanardi and F. Rossi, Phys. Rev. Lett. **81**, 4752 (1998).

[17] R.H. Blick and H. Lorenz, ISCAS 2000 proceedings, pp. II245-II248.

[18] F.R. Waugh et al., Phys. Rev. Lett. **75**, 705 (1995).

[19] T. Dittrich et al., *Quantum Transport and Dissipation*, (Wiley-VCH, Weinheim, 1998).

[20] D.V. Averin and Y.V. Nazarov in *Single Charge Tunneling* (eds H. Grabert and M.H. Devoret), Proc. NATO ASI Ser. B 294, (Plenum, New York, 1991), pp. 217-247.

[21] L.Borda et al., cond-mat/0207001 (2002).

[22] P.N. Agyres and P.L. Kelley, Phys. Rev. **134**, A 98 (1964).

[23] L. Hartmann, I. Goychuk, M. Grifoni and P. Hänggi, Phys. Rev. E **61**, R4687 (2000).

[24] M.C. Goorden, master's thesis, Delft University of Technology (2002).

[25] U. Hartmann and F.K. Wilhelm, phys. stat. sol. (b) **233**, No. 3 (2002).

[26] L.P. Kouwenhoven et al., Proceedings of the NATO Advanced Study Institute on Mesoscopic Electron Transport, edited by L.L. Sohn, L.P. Kouwenhoven, and G. Schön (Kluwer Series E345, 1997) pp. 105-214.

[27] W.G. van der Wiel et al., cond-mat/0205350 (2002).

[28] J.R. Schrieffer and P.A. Wolff, Phys. Rev. **149**, 491 (1966).

[29] C. Cohen-Tannoudji, J. Dupont-Roc and G. Grynberg, *Atom-Photon Interactions: Basic Processes and Applications*, (Wiley, New York, 1992).

[30] I. Shavitt and L.T. Redmon, J. Chem. Phys. **73**, 5711 (1980).

[31] U. Weiss, *Quantum dissipative systems*, 2nd ed., (World Scientific, Singapore, 1999).

[32] S. Nakajima, Prog. Theor. Phys. **20**, 948, (1958).

[33] R. Zwanzig, J. Chem. Phys. **33**, 1338, (1960).

[34] K. Blum, *Density Matrix Theory and Applications*, (Plenum Press, New York, 1981).

[35] R.D. Mattuck, *A Guide to Feynman Diagrams in the Many-Body Problem*, 2nd ed., (Dover Publications, New York, 1992).

[36] G.B. Arfken and H.J. Weber, *Mathematical Methods for Physicists*, (Harcourt AP, San Diego, 2001).

[37] I.S. Gradshteyn and I.M. Ryzhik, *Table of Integrals, Series, and Products*, 6th ed., (Harcourt AP, San Diego, 2000)

[38] J. König, H. Schoeller and G. Schön, Phys. Rev. Lett. **78**, 4482 (1997).

[39] A.J. Leggett et al., Rev. Mod Phys. **59**, 1 (1987).

[40] M. Grifoni, E. Paladino and U. Weiss, Eur. Phys. J. B **10**, 719 (1999).

[41] A. Abragam, *Principles of Nuclear Magnetism*, (Oxford University Press, Oxford, 1961).

[42] G.D. Mahan, *Many-Particle Physics*, 3rd ed., (Kluwer Academic / Plenum Publishers, New York, 2000).

[43] H. Quin, A.W. Holleitner, K. Eberl and R.H. Blick, Phys. Rev. B **64**, R241302 (2001).

[44] A.W. Holleitner et al., Science **297**, 70 (2002).

[45] A.K. Hüttel et al., cond-mat/0109104 (2001).

[46] T. Brandes and B. Kramer, Phys. Rev. Lett. **83**, 3021 (1999).

[47] S. Debald, T. Brandes and B. Kramer, Phys. Rev. B **66**, R041301 (2002).